



AGH

AGH UNIVERSITY OF SCIENCE AND TECHNOLOGY

Faculty of Physics and Applied Computer Science

Doctoral thesis

Tomasz Strączek

**„Structure, magnetic and relaxational
properties of surface modified maghemite
nanoparticles”**

Supervisor: **prof. dr hab. Czesław Kapusta**

Auxiliary supervisor: **dr hab. inż. Damian Rybicki**

Cracow, 2021

Declaration of the author of this dissertation:

Aware of legal responsibility for making untrue statements I hereby declare that I have written this dissertation myself and all the contents of the dissertation have been obtained by legal means.

Declaration of the thesis Supervisor:

This dissertation is ready to be reviewed.

*A heartfelt thanks to Prof. Czesław Kapusta
and dr hab. inż. Damian Rybicki for advisement
and support.*

*Thanks also to all those who contributed to this
work.*

Streszczenie

W rozprawie prezentowane są wyniki badań magnetycznych nanocząstek tlenków żelaza pokrytych różnymi polimerami. Materiały tego typu są obecnie często badane ze względu na ich potencjalne zastosowania, między innymi w medycynie. Superparamagnetyczne nanocząstki tlenków żelaza dzięki swym specyficznym właściwościom znajdują zastosowanie jako środki kontrastujące w obrazowaniu magnetycznym rezonansem jądrowym (ang. MRI) lub w magnetycznej hipertermii. Niezabezpieczone nanocząstki tego typu łatwo ulegają agregacji, stąd konieczność pokrycia ich czynnikiem który pomaga jej przeciwdziałać. Taka osłonka może zmienić ich właściwości chemiczne i fizyczne. Głównym celem tej pracy było zbadanie tego typu nanocząstek pod kątem ich dynamiki oraz wpływu otoczki na ich właściwości. Przedmiotem badań były nanocząstki z trzema różnymi otoczkami chitozanowymi o rdzeniach sporządzonych według tego samego procesu oraz dwie próbki komercyjnie dostępnych nanocząstek pokrytych dekstranem i glikolem polietylenowym.

W badaniach wykorzystanych zostało kilka technik badawczych. Dyfrakcja promieniowania X, mikroskopia elektronowa i dynamiczne rozpraszanie światła zostały użyte do ustalenia struktury krystalicznej, geometrii i rozmiarów badanych nanocząstek. Właściwości magnetyczne zbadano przy pomocy magnetometru wibracyjnego i zmiennoprądowego oraz spektroskopii Mössbauera.

Zaobserwowano duże różnice w superparamagnetycznej temperaturze blokowania oraz dynamice nanocząstek w zależności od ich rozmiaru, rodzaju polimerowych otoczek oraz ich grubości. Pokazana została także zależność zmiennoprądowej podatności magnetycznej wodnych zawiesin nanocząstek od warunków środowiskowych w kontekście relaksacji Browna i Néela. Pomiarы mössbauerowskie wykazały, że rdzenie nanocząstek, to utleniona forma magnetytu – maghemit i pozwoliły określić częstotliwości fluktuacji superparamagnetycznych. Badania przedstawione w rozprawie umożliwiły także ocenę przydatności badanych materiałów dla MRI (jako środki kontrastowe) i do magnetycznej hipertermii.

List of Contents

Abstract	7
List of abbreviations	9
I. Introduction	10
II. Nanoparticle materials and their applications	11
1. Nanoparticles and their types.....	11
2. Core-shell nanoparticles	13
3. Methods of synthesis	15
4. Magnetic nanoparticles.....	17
5. Biomedical applications of magnetic nanoparticles	19
III. Materials studied and characterization methods.....	23
IV. Structure and particle size study.....	27
1. Experimental	33
2. Results and discussion	34
3. Summary of structural and particle size studies	41
V. Study of basic magnetic properties.....	42
1. Experimental	55
2. Results and discussion	56
3. Summary of basic magnetic properties studies.....	62
VI. Magnetic dynamics	64
1. Experimental	66
2. Results and discussion	67
3. Summary for magnetic dynamics study.....	79

VII. Mössbauer spectroscopy studies.....	81
1. Experimental	89
2. Results and discussion	90
3. Summary of Mössbauer study	95
VIII. Conclusions.....	96
IX. References.....	98
List of graphs	133
List of tables.....	136
X. Appendix	106
1. Additional ACMS data	107
2. Raw VSM data	118
3. Fits performed for Mössbauer spectroscopy.....	125

Abstract

The thesis presents results of a study on properties of magnetic iron oxide nanoparticles covered with different type of polymer coatings. These materials have recently attracted a lot of attention of the scientific community due to the vast range of their potential applications. Magnetic properties of superparamagnetic iron oxide nanoparticles make them very useful in medical applications e.g. in magnetic hyperthermia or in MRI as a contrast agent. Pure iron oxide nanoparticles are susceptible to aggregation, therefore, they are usually covered with some type of coating forming shells on them. However, it can influence their chemical and physical properties. The main aim of this thesis is the study of properties of nanoparticles, in particular their dynamics and determination how the shell material changes the behavior of nanoparticles. Three iron oxide samples with different chitosan shells and the same type of the core material and two commercially available iron oxide samples covered with dextran and polyethylene glycol were investigated.

The study was conducted using several experimental methods including: x-ray diffraction, electron microscopy and dynamic light scattering used for determination of crystal structure and size of nanoparticles. The magnetic properties were investigated with vibrating sample magnetometry and alternating current susceptometry techniques. Mössbauer spectroscopy was employed to obtain additional information on the structure and the dynamic magnetic properties of the materials studied.

After the introductory Chapter I, a general information on the nanoparticle materials, their types, methods of their synthesis and more detailed description of magnetic nanoparticles and their biomedical application are contained in Chapter II. Materials studied and characterization methods are described in Chapter III. Subsequent chapters show results of the study of the following: Chapter IV – the structure and particle size, Chapter V – basic magnetic properties, Chapter VI- magnetic dynamics and Chapter VII – Mössbauer spectroscopy. The study revealed

significant differences of the superparamagnetic blocking temperature between the materials studied and the dependence of their dynamics on their size and the thickness of the shell and its composition. The influence of Brown and Néel relaxation processes on the magnetic susceptibility of the suspensions of nanoparticles was elucidated. A large variation of the superparamagnetic fluctuation frequencies between the materials studied was observed in Mössbauer study and the relation to their possible use in MRI and/or alternating magnetic field hyperthermia was discussed.

List of abbreviations

AC	-	alternating current
ACh	-	anionic derivative of chitosan
ACMS	-	alternating current magnetic susceptibility/susceptometry
χ^2	-	Pearson's chi-squared test
CCh	-	cationic derivative of chitosan
DC	-	direct current
DEX	-	dextran
DLS	-	dynamic light scattering
FC	-	field cooled
FWHM	-	full width at half maximum
HFF	-	hyperfine field
IONP	-	iron oxide nanoparticle
IS	-	isomer shift
MRI	-	magnetic resonance imaging
PEG	-	polyethylene glycol
QS	-	quadrupole splitting
SAR	-	specific absorption ratio
SPION	-	superparamagnetic iron oxide nanoparticle
STEM	-	scanning transmission electron microscopy
TEM	-	transmission electron microscopy
VSM	-	vibrating sample magnetometer/magnetometry
XRD	-	x-ray diffraction
ZFC	-	zero field cooled

I. Introduction

Recently, superparamagnetic nanoparticles have become a subject of intensive studies due to their potential applications in industry and biomedicine. Among them are diagnostic methods like MRI (magnetic resonance imaging), where nanoparticles can be used as contrast agents, alternating magnetic field hyperthermia in therapy or targeted drug delivery techniques, where these materials act as drug carriers. For such applications dynamical properties they exhibit in fluid suspensions are of crucial importance.

This work was focused on gaining information about physical properties of iron oxide nanoparticles covered with different shell materials. The biggest part of the thesis is related to characterization of their static and dynamic magnetic properties studied by vibrating sample magnetometry and alternating current magnetic susceptometry. The next important matter was to determine the physical dimensions of both the core and the shell and to obtain deeper insight into the crystal and chemical structure of the core. This was done with scanning transmission electron microscopy (STEM), x-ray diffraction (XRD), dynamic light scattering (DLS) and Mössbauer spectroscopy.

The thesis is divided into ten chapters including this introduction, as the first one. The second chapter “Nanoparticle materials and their applications” is devoted to the description of the current state of the art on the subject of nanoparticle materials, methods of their synthesis and current or potential applications. The third chapter “Materials studied and characterization methods” describes materials studied in this thesis and delineates characterization methods and equipment used. Next four chapters are the core of this thesis and are focused on the results of conducted experiments. Each of these chapters starts with theoretical background that, in author’s opinion, is relevant to the topic, then there are: description of the experimental procedure, results and their discussion and a short summary. These chapters appear in the following order: “Structure and particle size study” – the chapter presenting issues of size, shape, and crystal structure of the materials studied; “Study of basic magnetic

properties” – the chapter referring to the results of the vibrating sample magnetometry and describing the basics of the theory of magnetism; “Magnetic dynamics” – the chapter describing nanoparticle behavior under magnetic fluctuations and presenting the results of alternating current magnetic susceptometry studies; “Mössbauer spectroscopy study” – the chapter providing additional data about the structure of the nanoparticles studied and about their magnetic dynamics. The “Conclusion” section contains a summary of results and outlook on possible applications of the materials. The “Appendix” contains additional materials, such as all the results of ACSM measurements and results of fitting the Mössbauer spectra, which in author’s opinion aren’t that important to be placed in the main body of the thesis, but worth to be included there for the sake of the experiment documenting. The last chapter contains the list of literature used.

II. Nanoparticle materials and their applications

1. Nanoparticles and their types

Ever since R. Feynman first declared the start of an era of nanoscale techniques with his talk in 1959 (Feynman, R., 1960) a whole new discipline of science emerged, i.e. the nanoscience (or nanotechnology). Nanoscience extends over a wide area of scientific disciplines like chemistry, physics, electronics or computation techniques, with variety of nanometer scale structures including nanofibers, (Jiang et al., 2018), quantum dots (Chinnathambi and Shirahata, 2019), nanoscale mechanical devices (Wang et al., 2018) or nanoparticles. As for the definition what can be called a nanoparticle, the International Standard Organization states that it is nano-object with all three external dimensions in the nanoscale, whose the longest and the shortest axes do not differ significantly, with their ratio typically being of at most 3 (ISO, 2015).

The size does matter, especially when it comes to nanoscale, small particles can exhibit properties dramatically different than their bulk counterpart made of the same material. Two main reasons causing nanomaterials to behave differently than bulk materials are surface effects (caused by change in the surface to volume ratio) and

quantum effects (due to breaking of the long range symmetry) (Roduner, 2006). These factors affect the most of properties of materials, e.g. mechanical, optical, electric, magnetic as well as the chemical reactivity. Although the concept of nanoparticles is rather related to modern times, their unique properties have been utilized as early as middle ages in Mesopotamian and later, in European renaissance pottery. The gold-copper nanoparticles have been found to be incorporated into surface of glaze and were responsible for metallic luster (Mirguet et al., 2008; Padovani et al., 2003). Craftsman who originally used such techniques on their products couldn't have known why this works. First scientific attempts of description of the observed change in optical properties of gold, silver, copper and aluminum with decreasing thickness of leaves of these metals was done by Faraday in 1857 (Faraday, 1857). With only optical microscope he couldn't have determined true thickness of his specimen but it was a milestone achievement in the history of science.

Nowadays, there is so vast variety of nanoparticles being fashioned and studied that it is quite difficult task to divide them into distinctive groups. In fact, nanoparticles can be made of every solid chemical element, which is the simplest nanoparticle type. Concerning the motivation, the reason for using e.g. platinum nanoparticles as enhanced catalyst instead of its bulk piece is that for the same volume they can have much bigger active area. A similar may be said about other metallic nanoparticles, regardless of whether they are being used for their catalytic properties or for increased reactivity. Platinum nanoparticles are being commonly used in automotive catalytic converters, in hydrogen production, in carbon monoxide gas sensor, etc.. All those applications utilize catalytic ability of platinum nanoparticles to oxidize CO and NO_x or dehydrogenate hydrocarbons and also to split water. Their ability to inhibit the division of living cells could be used in medicine (Chen and Holt-Hindle, 2010). Nanoparticles of another noble metal, gold, exhibit very attractive electronic, optical, or molecular-recognition properties, and are the subject of intensive research. There are many existing, potential or prospective applications in a range of areas like electronics, materials science and engineering or biomedicine despite the fact that bulk metallic gold is known for its small chemical reactivity (Yang et al., 2015). Also silver may be used as catalytic agent, but most of the research up to now

was focused on its germicidal properties. Its chemical stability and catalytic properties make it advantageous among other metallic nanoparticles for antiviral, antibacterial, anticancer, antifungal and anti-inflammatory applications (Beyene et al., 2017). This is why silver nanoparticles are widely used in agriculture and medicine. Except for noble metals mentioned above, there are also studies on nanoparticles of other metals. For example iron nanoparticles have been tested for usability in soil pollution removal (Zhang, 2003).

From usually reactive and often exhibiting catalytic properties pure metals let us move to metal oxides, which are in general inert and chemically very stable. One of the most often used, also in terms of quantity, are titanium dioxide nanoparticles. Unlike white bulk TiO_2 , its nanoscale thin film form (thinner than 50 nm) is transparent to visible light but it absorbs UV light (Zhao et al., 2007). This property is one of main factors of its commercial use, e.g. in sunscreen filters and other UV protection application, for example to improve UV stability of polymers. Nanoparticles of ZnO exhibit similar optical properties and are also used in those applications. Another property which is often exploited is photocatalytic activity allowing for water purification (Baruah et al., 2016).

Various iron oxide nanoparticles are studied due to their magnetic properties and they are discussed below in more details. Also metal compounds have been studied as nanoparticles. For example FeNi were considered for applications in production of solar cells (Zheng et al., 2014). All previously mentioned nanoparticles are made of inorganic compounds, but there is also possibility of using organic structures. The same general principle is exploited here, i.e. the surface to volume ratio. As it turns out, functional groups of many organic compounds tend to stretch outwards of the particle, thus increasing their reactivity.

2. Core-shell nanoparticles

In the previous paragraph some types of nanoparticles and their applications have been briefly outlined. The problem is, that many of those extraordinary properties which are intended to be exploited, come with a price of other consequences of miniaturization. The most crucial parameter of any nanostructure is the size.

Unfortunately, in any suspension the nanoparticles will tend to reduce their surface energy by combining into groups, i.e. to agglomerate. Agglomeration is a reversible process, (Slomkowski et al., 2011) but if nanoparticles were allowed to stay in this form close together, they would start to aggregate. Aggregation takes place due to presence of forces attracting nanoparticles to each other e.g. as a result of electrostatic or magnetic interactions. When the distance between nanoparticles is small enough a chemical bond can be established. Then the entire cluster will evolve to create a single large particle, and this is irreversible. Note that this feature may be useful when one would like to filter out nanoparticles from the solution. All nanoparticles, which aren't inherently immune to it (Ott and Finke, 2006), will aggregate over time. So if they are intended to be used for long period of time, they have to be properly modified. One of the solutions is covering them with shells, which would reduce their susceptibility to aggregation.

The most important factor in determining physical properties of nanoparticles is their atomic composition. This particularly concerns their surface as the interface with the environment is greatly influenced by the chemical nature of the capping ligands. It dictates how nanoparticles are wetted by other species and where they locate relative to interfaces (Lin et al., 2005). Thus, the coating compound should be chosen accordingly to the potential application. Stability to oxidation can be achieved by covering nanoparticles with a hydrophobic bilayer. If nanoparticles are to be used in acidic environment one can choose basic polymers, such as e.g. hyperbranched polyethyleneimine. For stability in high salt buffers, nanoparticles should be coated with uncharged polymers, such as poly(ethylene glycol) (PEG). There is also a problem of physical accessibility of the core surface in applications based on its catalytic or reactive nature. In this case one should choose light ligands attached to its surface instead of polymers (Grubbs, 2007). Adding a polymer cover to nanoparticles also gives opportunity for custom adjustment of its properties by attaching or modifying other functional groups of polymer. This approach unfolds new perspectives in potential applications, for example by giving them hydrophobic properties (Zhu et al., 2010). Synthetic polymers: polyethylene glycol (PEG) (García-Jimeno and Estelrich, 2013), polyvinylpyrrolidone (PVP) (Huang et al., 2010),

poly(lactic-co-glycolic acid) - PLGA (Schleich et al., 2013) and those of natural origin: dextran (Tassa et al., 2011), starch (Cole et al., 2011), chitosan (Szpak et al., 2013; Unsoy et al., 2012), gelatin (Gaihre et al., 2009), alginate (Ma et al., 2007) have been used in recent years as coatings for superparamagnetic iron oxide nanoparticles (SPIONs). Other examples are fatty acids (oleic acid) (Bloemen et al., 2012), amino acids (arginine) (Ebrahimezhad et al., 2012), oxides (silica) (Alwi et al., 2012; Lewandowska-Łańcucka et al., 2014), or metals (silver) (Mahmoudi and Serpooshan, 2012).

3. Methods of synthesis

It actually isn't so difficult to create nanoparticles. The reason that it took such a long time to study their properties was a lack of means to observe them. In fact air pollution with nanosize particles is attracting ever growing attention. They are often byproduct of technological processes like welding or just side effect of operation, like carbon black production in internal combustion engine (Bystrzejewska-Piotrowska et al., 2009; Kittelson, 1998). Creating nanosized particles isn't a problem, but as their size and phase composition can greatly influence their characteristics it is very important to be able to make them repetitively and with control over mentioned factors.

The methods of synthesis are often divided into top-down and bottom-up methods. The first means obtaining nanoparticles by fragmentation of bulk material, the second - by synthesizing them from different chemicals. Top-down techniques are mostly done by physical means, with *e.g.* high energy milling, laser ablation or vapor deposition. Ball milling would be the most simple solution to create smaller particles from bulk material. Most of the inorganic particles can be created that way, with their characteristics controlled by milling time, rotation speed, ball-to-powder weight ratio as well as temperature and pressure. Milling can be done in vacuum, at ambient or reactive atmosphere or in liquids. Another example of such approach can be method of laser ablation (PLA). Although it has some disadvantages including size distribution, it is quite promising and easily scalable. This method can also provide all kinds of inorganic nanoparticles. Their dimensions can be controlled with laser beam

parameters like wavelength, beam incident angle, energy of single pulse, its time and delay or the atmosphere in which ablation occurs (Caricato et al., 2016). PLA can be included in larger group of techniques called physical vapor deposition (PVD). PVD is a technique based on deposition of vapor of material onto a substrate. Vapor is created by evaporation of material by physical means (laser, electron, ion beam or arc melting). In more traditional manner substrate is made of solid block and, as a result, a thin film is created but, if substrate is replaced by solvent, it is possible to produce nanoparticles. The selection of the solvent is one of decisive factors determining the shape and size of nanoparticles obtained along with pressure and temperature. Nanoparticles of inorganic origin can be prepared using this method, but there are already attempts to make polymer specimens. With the right solvent environment it is also possible to create core-shell nanoparticles with polymer coating. Using multiple targets of vaporization, nanoparticles with more complex structure, for example FeCo or FePt, have been made (Dhand et al., 2015). Those physical means of creating nanoparticles are considered to be environmentally friendly since they produce small amount of waste.

The second approach, bottom-up, involves mostly chemical methods of synthesis. One of the most popular is a sol-gel technique. In this preparation method, two types of components are used. The first one is a sol which is a colloidal suspension of solid particles in a liquid. The second one is a gel, which is a polymer containing liquid. Typical steps of the process are hydrolysis and condensation, in which the former uses water to disintegrate the bonds of the precursor (Karak, 2009). Formation of nanoparticles occurs by condensation, after which excess water is removed. Factors that can affect final attributes of nanoparticles are: precursors, solvent percentage, water percentage, reflux temperature, reflux time, calcination temperature or sol drying method used (Kundu, 2013). Sol-gel is a promising method for the synthesis of variety of nanoparticles such as metal aluminate, magnetic Fe-Co, ZnO, Fe₂O₃, ZrB₂, GdVO₄, Ta₂O₅, TiO₂, SnO₂. To synthesize metal oxide nanoparticles the thermal decomposition technique may also be used. In this method, a salt of transition metal, for example Fe, is stabilized in an organic solvent solution and then mixed with an organic compound to form an organometallic complex. Nanoparticles are created by

the organometallic complex decomposition at high temperatures (Gumieniczek-Chłopek et al., 2020) [EGC Materials 2020]. Stabilized metal salts can be achieved with a wide range of surfactants like oleylamine, pentanedione, oleic acid, or benzylamine (Chaudhuri and Mandal, 2012). Inorganic and hybrid (core-shell) nanoparticles can also be synthesized via coprecipitation method, which is described in the subsequent chapter. In this approach, two or more water soluble salts react in an aqueous solution to form a water insoluble salt that precipitates and forms the nanoparticles.

4. Magnetic nanoparticles

Magnetic properties of bulk materials and nanoparticles will be discussed in more detail in a separate section below and here only the current state of the art and main applications of magnetic nanoparticles are presented. Magnetic nanoparticles have attracted large interest mainly due to their two extraordinary properties. The single domain ferromagnets can achieve much higher coercivity and, therefore, remanent magnetization values compared with the bulk material, which makes them suitable materials for permanent magnets (Tolea et al., 2010). The second property is their superparamagnetic behavior. For small enough nanoparticles their anisotropy energy is comparable with the thermal energy and their magnetic moment will switch randomly between antiparallel states along the easy magnetization axis, resulting in zero net magnetization, similarly to paramagnetic materials. The prefix “super” is added due to the fact that their initial susceptibility is very high (comparable with ferromagnetic materials). Those two properties, in addition to other general properties of nanoparticles, might be useful for variety of applications including vast area of biomedical use. Magnetic nanoparticles are often made of ordinary magnetic materials such as iron oxides, pure metals, alloys (e.g. FeCo) and spinel-type compounds (e.g. CoFe_2O_4 or MnFe_2O_4) and thus may be synthesized with all methods mentioned above. For example, permanent magnets can be made as the so called exchange spring magnet, which consist of interfaced hard and soft magnetic nano-phases coupled by the exchange interactions. These phases can be e.g. $\text{RE}_2\text{Fe}_{14}\text{B} + \text{Fe}$ where RE is a rare earth element Nd or Pr, which can be made by arc melting and, subsequently, HDDR (Hydrogen Decrepitation, Disproportionation, Recombination) processed to obtain

nanopowder (Gutfleisch et al., 1994). With 25% of Fe nanoparticles and optimal annealing conditions the energy product $(B \cdot H)_{max}$ of more than 90 kJ/m³ was achieved (Tolea et al., 2010). Another study shows dependence of the saturation magnetization, M_s and the temperature of superparamagnetic threshold (T_b) on the shape of Fe₃O₄ nanoparticles. It was found that T_b decreased when the morphology of nanoparticles changed from spherical to cubic (Zhen et al., 2011). The M_s increased from 18 emu/g for rods, to 40 emu/g for cubes, and 80 emu/g for spheres, showing strong influence of the shape anisotropy (Yang et al., 2007).

Beside applications related to production of magnetic field there are other useful possibilities. For example there is a study exploiting magnetic nanoparticles for magnetically tunable viscosity and visible light transmission where CoFe₂O₄ ionic ferrofluids prepared by coprecipitation and acid treatment were used (Li et al., 2004). In another study, 10 nm magnetite nanoparticles were used for tunable thermal conductivity and viscosity, with clearly visible effect of magnetic field. With the applied field of 500 Oe a twofold increase of both viscosity and thermal conductivity coefficients was observed (Shima et al., 2009). Electronic and electric devices can also be improved by implementing magnetic nanoparticles into magnetic cores of transformers or coils. For example, an on chip transformer with magnetite nanoparticles ferrofluid was built and studied (Tsai et al., 2010). High voltage transformers for electrical grid could be improved by using mineral oil based magnetite ferrofluids to increase their breakdown voltage parameter (Segal et al., 1998). Up in the space there is recently started experiment involving magnetite nanoparticles based ferrofluid to test its usefulness in inertial satellite positioning (KRAKsat, 2019). Also its use for heat harvesting is studied with purpose of space applications (Chiolerio et al., 2020). It is worth mentioning that they also can be used in environmental protection e.g. for separation of polluting elements from water (Maziarz et al., 2019b, 2019a). The number of applications of magnetic nanoparticles is constantly growing and new possibilities open up all the time, e.g. in nanomedicine, where nanoparticles decorated with antibodies were recently successfully used for capture of circulating cancer cells (Karnas et al., 2021).

5. Biomedical applications of magnetic nanoparticles

There are several fields in which nanoparticles can be implemented in biomedicine. Some applications are at the testing stage, but others are already approved for therapy or diagnostics e.g. for magnetic resonance imaging (MRI) contrasts. MRI is one of the modern, noninvasive imaging techniques used for medical diagnostics. Its main advantage is that it uses nonionizing electromagnetic radiation. Medical MRI is usually based on proton (hydrogen) magnetic resonance, so the signal is proportional to water content in a tissue. Also, relaxation time of protons spins instead of e.g. absorption of X-Rays (tissue density measure) like in computer tomography, allows for imaging differences also in a soft tissue. Although MRI is being developed since 1971, it still faces some difficulties, for instance the presence of various artifacts like air bubbles or calcification should be accounted for and sensitivity of the technique could be improved (Yoo et al., 2011). The problem is that in normal conditions spin-lattice nuclear magnetic relaxation time of hydrogen atoms is usually too long to perform high refresh rate imaging needed for example to diagnose heart diseases. This can be overcome with administration of MRI contrast agents to the patient. Recently, gadolinium complexes, which have been used as MRI contrast, are being replaced by superparamagnetic nanoparticles e.g. of iron oxides (Szpak et al., 2014; Weissleder et al., 1990; Widder et al., 1987).

Another application which has been developed is targeted drug delivery. The idea originated from the Nobel prize winner Paul Ehrlich. As in many cases side effects of using a drug are as dangerous or unpleasant as diseases they were intended to cure, Ehrlich suggested to concentrate drug in selected region of the body to limit its harmful effects. Since then, many scientists proposed strategies to deliver a drug to the vicinity of a disease infected region. Among others, the use of vectors (i.e. carriers) sensitive to physical factors or having tumor-recognizing parts were incorporated into a drug. Since then, this technique has been developed by many researchers and they have created delivery strategies with magnetic carriers starting from micro scale, down to nanoparticles. Carriers containing magnetic nanoparticles can e.g. be trapped and then hold in place by external magnetic field or permanent magnet implanted into the region of interest. Diverse therapies including chemotherapy, antiangiogenic or

radiation therapy have been developed and some of them were in clinical trials (Arruebo et al., 2007). However, there are some challenges that must be faced when it comes to using magnetic nanoparticles in such a manner. The most important one is optimization of their size. Overall magnetic moment decreases with nanoparticle radius, so stronger magnetic field and/or its gradient is required to hold them in place. On the other hand large nanoparticles are more likely to be caught and fagocited by the immune system. This contradiction could be resolved by finding materials with higher M_s or by modifying nanoparticle shell with polymers, which are invisible to the immune system. However, then the shell can influence the magnetic properties of the nanoparticle itself (Gaur et al., 2000). Numerous nanoparticle types were used or are being tested for targeted drug delivery, for example: iron oxides, Au or Si coated Fe, Co, Ni or of alloys, like FePt (Sun et al., 2008; Veiseh et al., 2010).

The last potential application of magnetic nanoparticles that is discussed in this thesis is magnetic hyperthermia. In medicine, hyperthermia is a condition where the body temperature of an individual is elevated beyond normal due to failed thermoregulation. Such a condition can cause irreversible damage to the organism and may be exploited as therapy if it could be caused locally. Such an approach can be observed in nature. When a hornet attacks a honeybee nest, the bees will gather around the hornet and by rapid wing movement heat him up above his temperature limit (Ono et al., 1995). Analogous action could be taken to destroy a tumor in human body if only there was a way to selectively and, the best – remotely, heat it up. Here we can employ magnetism. Ferromagnetic materials absorb energy when put into alternating magnetic field of appropriate strength. The effect occurs due to magnetic domain wall movement for minimizing the internal energy (this topic is discussed in more details in the part of the thesis discussing magnetic properties). Nanoparticles which exhibit superparamagnetic behavior also absorb energy below their superparamagnetic threshold temperature, but the field strength required for this is usually much smaller compared to the ferromagnetic material. To quantitatively describe the heating effect of the external energy delivered to the body, the value of the specific absorption rate (SAR) was defined as the power absorbed per mass of the tissue (W/kg). SAR is usually measured for assessment of the negative influence of technology e.g. wireless

electronics operating at radio/microwave frequency, like mobile phones or Wi-Fi. In magnetic hyperthermia applications it is often called the specific power absorption (SPA) and is defined in relation to the mass of absorbing media. For chemically synthesized maghemite nanoparticles the highest SAR value achieved was 600 W/g (Hergt et al., 2004) and 720 W/g was reported for Co nanoparticles (Müller et al., 2005).

Materials for magnetic hyperthermia made of ferro/ferrimagnetic nanoparticles can simply be characterized by static magnetic measurements, as the total power outcome depends on values like saturation magnetization and coercive field. In the case of metal alloys, or other conductive material, part of the absorbed energy is due to eddy currents induced by alternating magnetic field. On the other hand, in the superparamagnetic materials the relation of energy absorption to static magnetic properties isn't simple (Lacroix et al., 2009), but depends strongly on temperature and frequency of the applied magnetic field. Therefore, measurements in dynamic magnetic field are most suited for their characterization.

The most obvious approach to enhance heating effect of magnetic hyperthermia would be to increase the concentration of the absorbing media or the power of the magnetic field, but there are limitations of physical and biological nature. The problem with concentration is that in colloids with high concentration of nanoparticles agglomeration is inevitable, no matter how well they are protected against it with their shells. Moreover, increasing concentration even of biocompatible material like $\gamma\text{-Fe}_2\text{O}_3$ can become harmful to the organism. This issue is still being researched towards formulation of guidelines on the critical concentration (Buzea et al., 2007). There exist, however, many publications pointing at toxicity of magnetite nanoparticles via producing reactive oxygen species or even directly damaging the DNA in concentration as low as 50 $\mu\text{g/ml}$ (Ansari et al., 2019; Gaharwar et al., 2017). The next limitation is the electromagnetic field power. There is no definite answer to how strong this field can be allowed but available literature gives quite wide estimates ranging from 400 kHz Oe (Hergt et al., 2004) up to 6 MHz Oe (Baker et al., 2006). Such a broad spread results from many additional factors that might cause harmful

effects, e.g. time of exposure. There is another limitation to the electromagnetic field, the maximum frequency cannot exceed approx. 1 GHz since it would cause excitation of water molecules and thermal damage to the skin. The next potential obstacles are the Curie temperature of ferromagnetic nanoparticles or the blocking temperature of superparamagnetic nanoparticles. Once they are exceeded, the heating power decreases rapidly. This, however, can be turned into an advantage if those transition temperatures could match the maximum allowable temperature of heating. This would help in preventing the overheating of the surrounding tissues by creating a negative feedback loop (Pollert et al., 2007). Shell thermal conductivity has to be considered too and it also sets constraints to the shell thickness (Gonzalez-Fernandez et al., 2009).

III. Materials studied and characterization methods

The hybrid core-shell nanoparticles studied in this thesis were obtained via coprecipitation method. In this approach, two or more water soluble salts react in an aqueous solution to form a water insoluble salt that precipitates and forms nanoparticles. Hydrated ferrous chloride ($\text{FeCl}_2 \cdot 4\text{H}_2\text{O}$) and ferric chloride ($\text{FeCl}_3 \cdot 6\text{H}_2\text{O}$) undergo oxidative reaction following deprotonation in aqueous solution in the presence of $\text{NH}_3 \cdot \text{H}_2\text{O}$ as the precipitating agent. The overall reaction can be written as:



The product precipitates by nucleation in the liquid phase when the concentration of product in the solution increases above the solubility limit. The growth of Fe_3O_4 crystals continues with precipitation reaction on the nucleating surfaces. Iron oxide nanoparticles are formed after small particles undergo agglomeration via Ostwald ripening (Chaudhuri and Mandal, 2012). Cationic (CCh) and anionic (ACh) derivatives of low molecular weight chitosan were obtained according to the procedures described by Bulwan (Bulwan et al., 2009).

SPION-CCh

SPIONs coated with cationic derivative of chitosan (SPION-CCh) were obtained using the procedure developed by Szpak (Szpak et al., 2013). Briefly, iron salts in molar ratio Fe(III):Fe(II) = 2:1, were dissolved in 50 ml of aqueous solution of CCh (1g/l). The solution was deoxygenated by purging with argon and sonicated for 10 min in a thermostated bath (20°C). Next, 5 ml of 5MNH₃(aq) was added drop-wise, and the solution was further sonicated for 30 minutes. Finally, the precipitated nanoparticles, SPION-CCh, were purified by magnetic filtration.

SPION-CChB

Additionally SPION-CCh-B were prepared using the analogous procedure as in the case of SPION-CCh but sonication in thermostatic bath and argon bubbling were not applied. Briefly, iron salts in molar ratio Fe(III):Fe(II) = 2:1, were dissolved in 50 ml of aqueous solution of CCh (1g/l). Next, 5 ml of 5MNH₃(aq) was added drop-wise. The final product was extracted by magnetic separation.

SPION Gd

SPIONs with surface attached gadolinium complex SPION Gd (ACh-Gd DTPA) were obtained using the procedure developed by (Szpak et al. 2014). Briefly, in the first step ACh polymer was modified with gadolinium complex using NHS, EDC (carbodiimide chemistry) and Gd DTPA aqueous solution. The mixture was stirred for 24h at room temperature, dialyzed against distilled water for 7 days and the modified polymer (ACh-Gd DTPA) was lyophilized. In the next step SPIONs coated with ACh-Gd DTPA were prepared: ACh-Gd DTPA solution was mixed with purified SPION-CCh suspension and sonicated for 10 minutes. The product was purified by magnetic filtration.

PEG-IONP

Iron Oxide Nanoparticles with surface coating with amphiphilic polymer and PEG (polyethylene glycol) of a commercial origin were used. According to data provided by manufacturer their average size is 30 nm with less than 10% distribution and chemical formula corresponds to magnetite, Fe₃O₄. They are delivered as a 5 mg/ml water solution.

DEX-IONP

Iron Oxide Nanoparticles with surface coating with amphiphilic polymer and dextran, a polysaccharide made of many glucose molecules, were of a commercial origin. According to data provided by manufacturer their average size is 10 nm with less than 10% distribution and chemical formula of maghemite, $\gamma\text{-Fe}_2\text{O}_3$. They are distributed as a 5mg/ml water solution.

Characterization methods

Dynamic light scattering (DLS)

Hydrodynamic sizes and zeta potentials of the nanoparticles obtained were measured by dynamic light scattering (DLS) using ZetaSizerNano ZS (Malvern Instruments Ltd.), equipped with He-Ne laser operating at 633 nm. The measurements were performed at 25°C, three times for each sample. The mean weighted size according to distribution by number, as well as, zeta potential were determined.

Scanning transmission electron microscopy (STEM)

The size and shape of nanoparticles studied was characterized by STEM (FEI Nova NanoSEM 450). Nanoparticles were deposited on carbon coated copper mesh grid and air-dried at room temperature. The bright field high resolution electron microscopy images were obtained.

Vibrating sample magnetometry (VSM)

Basic magnetic properties were studied with vibrating sample magnetometer which is a part of Quantum Design Physical Property Measurement system (QD PPMS). System is equipped with 90 kOe (9 T) superconducting magnet and is capable of reaching temperatures from 2 K up to 350 K.

Alternating current magnetic susceptibility (ACMS)

To obtain more detailed information on dynamic magnetic properties an Alternating Current Magnetic Susceptometer (ACMS) was employed. ACMS is also an add-on to PPMS set-up and it has the same magnetic field and temperatures capabilities. The AC field can vary from 1 Hz to 10 kHz and its strength can be controlled between 0 and 10 Oe.

Mössbauer Spectroscopy

⁵⁷Fe Mössbauer measurements have been carried out in the transmission mode at a constant velocity spectrometer (MOSIEK 3E, Elektronika Jądrowa). A 50 mCi ⁵⁷Co/Rh source has been used. For measurements at low temperatures the bath cryostat with cold finger was used. Measurements in the magnetic field were conducted using set of permanent magnets and the magnetic field strength was measured with Hall effect probe. Additional high magnetic field measurements were conducted at Jagiellonian University, Faculty of Physics, Astronomy and Applied Computer Science.

X-ray diffraction (XRD)

X-ray diffraction experiments have been performed with a Siemens D5000 diffractometer at room temperature. The Cu K_α source and a rear graphite monochromator were used. The samples were placed at a glass substrate and fixed at the table of the goniometer. The diffraction patterns obtained were analysed with the X'Pert Highscore Plus software in order to identify the crystallographic phases present in the materials studied, by comparison with database references.

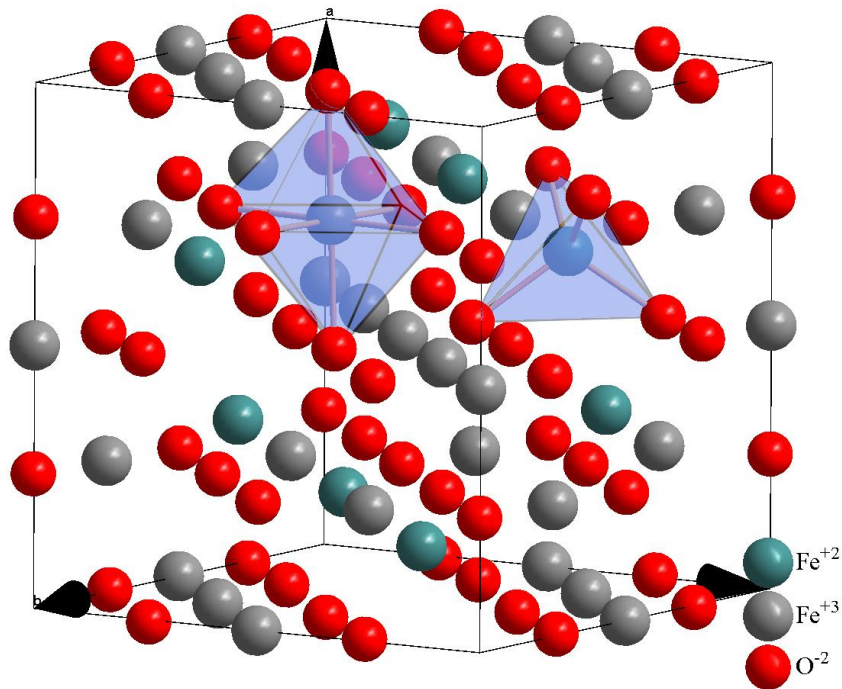
IV. Structure and particle size study

1. *Basic physical properties of magnetite*

Magnetite (Fe_3O_4) is a mineral that crystallizes in an inverse spinel structure, which is regular structure described by H-M symbol: $Fd\bar{3}m$ with lattice constant $a=8.397 \text{ \AA}$ (Anthony et al., 1990). The oxygen ions are forming a face-centered cubic crystal system and Fe ions occupy octahedral and tetrahedral sites at equal proportion in ideal stoichiometry (Fig. IV-I). Its chemical formula is $\text{Fe}^{2+}\text{Fe}_2^{3+}\text{O}_4^{2-}$ where Fe^{2+} and Fe^{3+} are placed on the octahedral sites, and the tetrahedral lattice is occupied only by Fe^{3+} . Magnetite is a ferrimagnetic material with moments of iron ions on octahedral and tetrahedral sites set antiparallel to each other. Curie temperature of magnetite is 856 K. Around 130 K magnetite undergoes the Verwey transition changing its structure to monoclinic (Verwey and Haayman, 1941). This change influences magnetic, electrical and thermal properties. Verwey transition temperature, and even its occurrence, is strongly related to stoichiometry (Aragón et al., 1985).

2. *Basic physical properties of maghemite*

Maghemite ($\gamma\text{-Fe}_2\text{O}_3$) is fully oxidized form of magnetite and it has the same structure. In oxidation process two thirds of the Fe^{2+} ions oxidizes to Fe^{3+} . Remaining Fe^{2+} ions at the octahedral sites are being moved by diffusion and replaced with vacancies. The diffusing Fe^{2+} ions get oxidized to Fe^{3+} and built into new maghemite cells of inverse spinel structure. Maghemite is metastable at high temperature and has strong tendency to transform to hematite at $\sim 700 \text{ K}$ (Banin et al., 1993). The Curie temperature of stoichiometric maghemite was estimated to be 853 K but it is difficult to prevent hematite transformation at this temperature. The main difference between maghemite and magnetite is in local neighborhood, which is hardly visible in the x-ray diffraction.



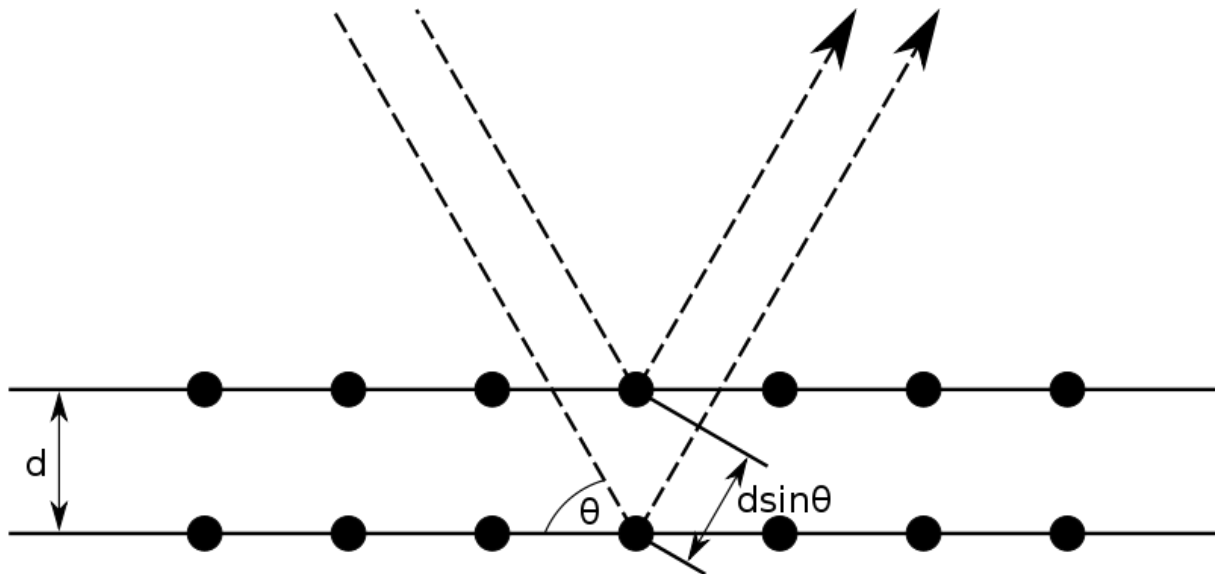
Graph IV-I Crystal structure of magnetite with marked tetrahedral and octahedral positions.

3. X-Ray diffraction

Most of solid matter is made of grains which may be considered as ideal crystals with the exception that they are of finite size. Ideal crystals are made of periodic blocks of particles. This smallest possible set of particles creating crystal is called an unit cell. With the help of crystallography it is possible to describe such a structure with a space group symbol or Hermann–Mauguin symbol and list of atoms position within unit cell, called Wyckoff positions. Every atom can scatter electromagnetic radiation, when atoms are organized in periodic manner, reflection created on every atom can interfere with reflections on other atoms. By using x-ray light source with wave length comparable with interatomic distances it is possible to observe diffraction pattern unique for a given structure. The condition to observe maximum intensity of reflected beam is given by the Wolf-Bragg diffraction law:

$$2d\sin(\theta) = n\lambda \quad \text{Eq. IV-I}$$

where d is the distance between planes, θ is the angle between plane and incident beam, λ is the wave length. It is schematically shown in Graph IV-II.



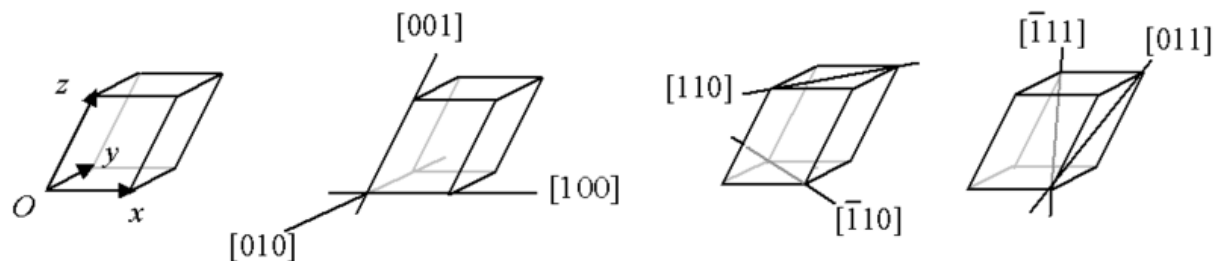
Graph IV-II Schematic representation of Bragg law.

(SOURCE: [HTTP://EN.WIKIPEDIA.ORG/WIKI/FILE:DIFFRACTIONPLANES.PNG](http://en.wikipedia.org/wiki/File:Diffractionplanes.png))

Using Miller notation which describes crystallographic planes in relation to unit cell borders, like it is shown in Graph IV-III, it is possible to calculate theoretical diffraction pattern of a known structure. In cubic structures Miller indices are spread upon orthonormal base vectors and by this, the distance between planes is given by:

$$d = \frac{a}{\sqrt{h^2 + k^2 + l^2}} \quad \text{Eq. IV-II}$$

where a is the lattice constant and h , k , and l are the Miller indices of the Bragg plane.



Graph IV-III Crystallographic directions representation (SOURCE: [HTTPS://COMMONS.WIKIMEDIA.ORG/W/INDEX.PHP?CURID=457850](https://commons.wikimedia.org/w/index.php?curid=457850))

If one has an ideal crystal it is simple, however, as was mentioned earlier, the real matter is composed of grains. Existence of those adds disorder to the structure and this may also change the distance between planes. There are more factors that can influence the diffraction pattern, like stress and strain present in real material. Changes of peak width and positions of peaks can be used to determine those internal forces through Williamson-Hall analysis (Williamson and Hall, 1953). It is also possible to use Scherrer equation, which relates the size of sub-micrometer grains of particles in a solid matter to the broadening of peaks in a diffraction pattern (Patterson, 1939; Scherrer, 1912). It can be used to determine the size of particles of crystals in the form of powder. The Scherrer equation can be written as:

$$\tau = \frac{K \lambda}{\beta \cos(\theta)} \quad \text{Eq. IV-III}$$

where: τ is the mean size of the grains; K is a dimensionless shape factor. The shape factor has a typical value of close to 0.9, but may vary with the actual shape of crystallites; β is the line width at the half of the maximum intensity (FWHM) after subtracting the instrumental line broadening, in radians. Scherrer equation was used in this work to estimate the size of magnetic core of the nanoparticles studied.

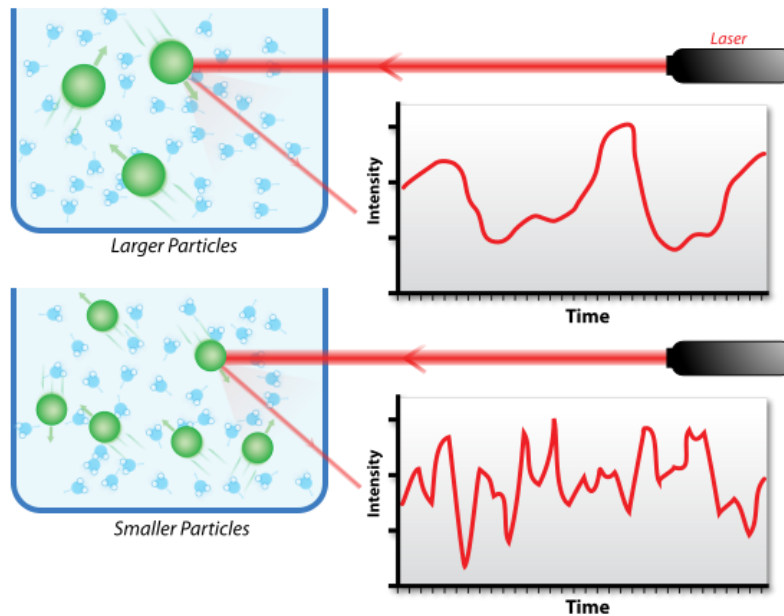
4. Scanning transmission electron microscopy (STEM)

Old good optical microscopy, discovered and used by Assyrians ages before Christ, then developed by European scientists in XVII century, contributed remarkably to advancements in general science. Unfortunately due to its nature optical microscope has limitation of magnification because of resolving power of visible light which has limited wave length. Maximal resolving power of optical microscope is about 10 μm (Rose, 1994). In XX century this limitation has been overcome by invention of transmission electron microscope (TEM). With development of electronics and physics it became possible to use imaging media other than light, i.e. electrons. With their little mass and easy acceleration in the electric field they can have adjustable de Broglie wavelength. Instead of using polished glass lenses TEM is equipped with magnetic and electrostatic beam forming lenses. The main difference is that in TEM

the image is created from electrons transmitted through specimen, unlike in optical microscope, where it is created from reflected light. This limits TEM usage only to thin samples (~100 nm). Another difference is that the image has to be projected on the screen, as electrons are invisible to the naked eye. TEM resolving power is of 1 nm. Scanning transmission electron microscope is a modification, where beam is focused in one point and then swept through the area of the sample. From images taken with STEM one can measure particle size, their shape and even composition, as the shell may absorb electrons less than the core. Estimation of agglomeration and size distribution of particle size in the sample is also possible and, with usage of software, it is pretty straightforward.

5. *Dynamic Light Scattering (DLS)*

The dynamic light scattering is a technique widely used for determination of the size and its distribution for nanoparticles in colloids. This is an indirect measurement involving observation of light scattering in a suspension. The light source used is mainly laser based because of its high coherence. By directing the laser beam at the suspension of fine particles and registering the time dependence of the light backscattered from these particles an oscillating pattern emerges (Graph IV-IV). Using the autocorrelation function it is possible to assess the particles diffusion coefficient from the rate of decay of the correlation of this pattern in time. Assuming a spherical shape of particles it is possible to use Einstein-Stokes equation to calculate the hydrodynamic radius of scattering particles. This approach would, however, work only for monodisperse suspension. In order to obtain information of the size distribution in a polydisperse suspension the second-order autocorrelation function has to be used.



Graph IV-IV Schematic representation of the principle of operation of dynamic light scattering, which is recorded as a function of time. Depending on the particle size different pattern is obtained (source: https://en.wikipedia.org/wiki/Dynamic_light_scattering#/media/File:DLS.svg)

The hydrodynamic radius is the radius of the theoretical sphere that would behave in a viscous environment in a similar way as the object under study does. Therefore, it isn't the real particle dimension, but rather a mathematical equivalent of it, which can be used for calculations. The hydrodynamic radius is also discussed later in the thesis in the chapter VI related to Brown relaxation. The difference compared to e.g. TEM is that this method is sensitive also to the polymer shell and the particle behavior in a real suspension, e.g. the solvent molecules attaching to the particle. In fact, this is not a drawback but rather an additional information compared e.g. to TEM or STEM images. There are other limitations of this technique, like concentration limit, as at high concentrations multiple scattering events will disturb the measurement. Negative influence of the high concentration can be limited with increasing the observation angle. Another limitation is that DLS method is more sensitive to bigger particles, therefore the size distribution shouldn't be too broad and the particle size shouldn't be bigger than 10 μm

DLS enables also another type of measurement. With voltage applied to plates on opposite sides of the suspension container it is possible to measure the potential of the shell. This is called electrophoresis light scattering and is based on the same

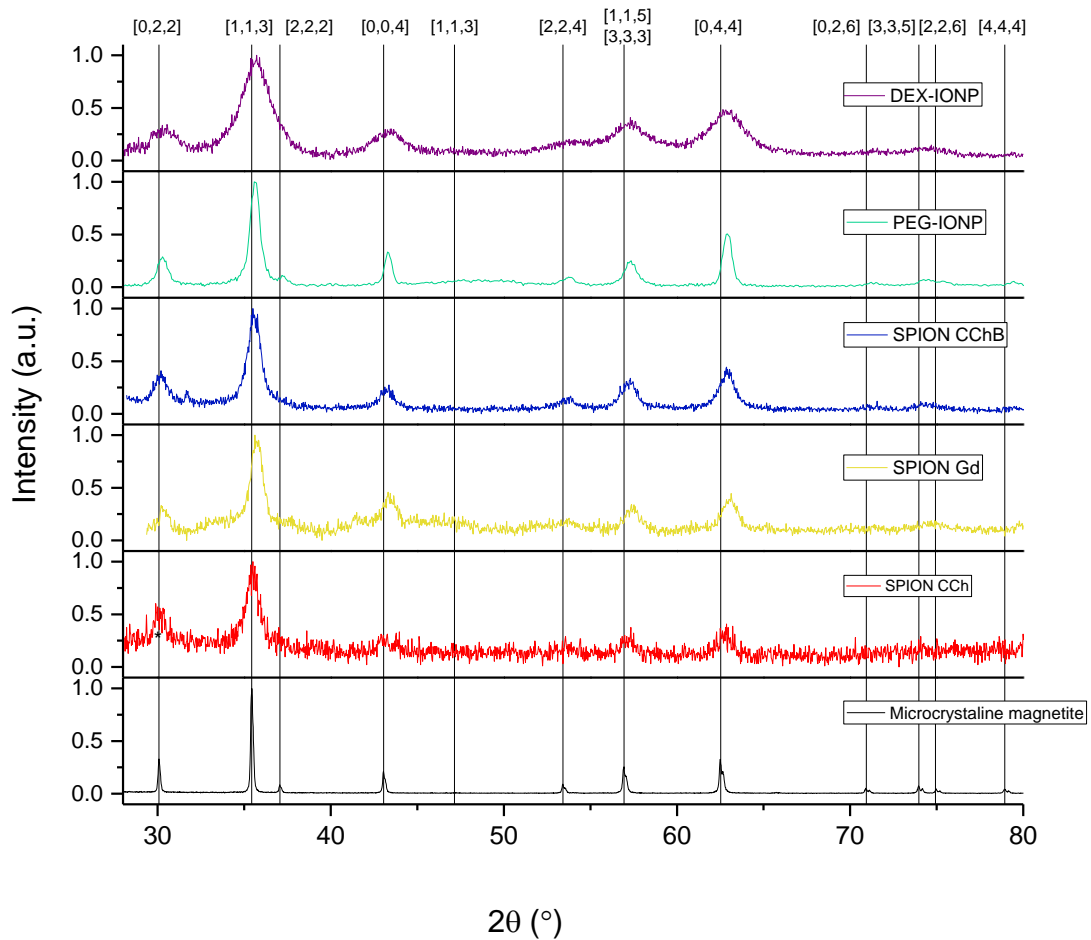
principle, but with movement of particles caused by alternating electric field and measuring the Doppler effect. Results of this measurement are often recalculated to the zeta potential, which is the surface potential of particles in suspension. The zeta potential is an important property, which allows us to assess suspension stability, as particles with high surface potential repel each other and do not agglomerate easily.

1. Experimental

At the beginning of the research it was important to determine the exact crystalline structure of investigated materials. One of the most common techniques to do this is X-Ray Diffraction (XRD), described briefly above. In order to perform XRD it was necessary to dry out the specimen as it is much easier to perform it in a solid state. Drying was carried out by dripping water solution of nanoparticles on a heated substrate made of either an amorphous silicon or polypropylene tape. XRD was carried out in theta - 2 theta mode in the range from 10 to 80 angular degrees at room temperature with Cu water cooled X-Ray tube of the Siemens D-5000 diffractometer.

DLS equipment is designed to use with liquid materials therefore, samples did not require any special treatment.

2. Results and discussion



Graph IV-V XRD results for studied SPION and IONP samples with microcrystalline magnetite diffraction pattern for comparison.

The collected data, with subtracted background and normalized for all studied samples and a reference sample (microcrystalline magnetite) are shown in Graph IV-V. Diffraction peaks for all of the nanoparticle materials are in a good match with the reference, thus it can be concluded that their crystalline structure is the same as that of the magnetite. Significant broadening of diffraction peaks can be observed in nanoparticle samples compared to the reference sample, which is a consequence of the size effect and can be used to determine the mean size of crystallites in nanoparticles via the Scherer's formula. This would correspond to the particle size if we have single crystallite particles and this can be verified by a comparison with the STEM results.

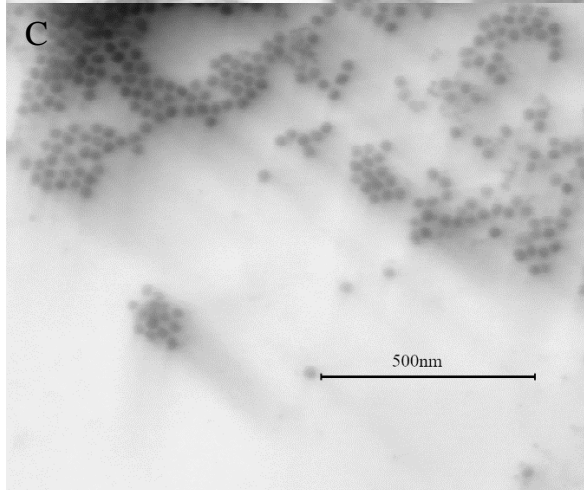
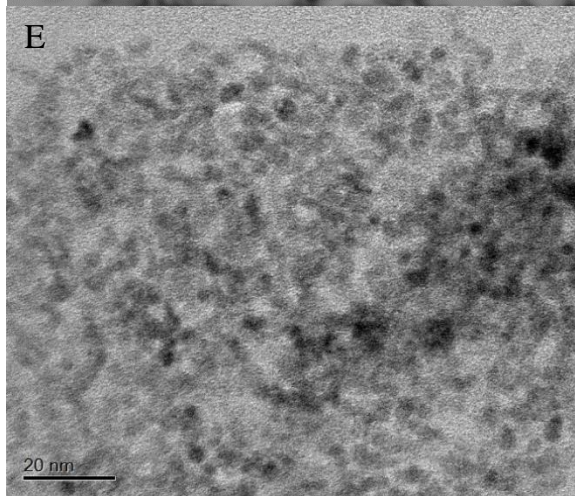
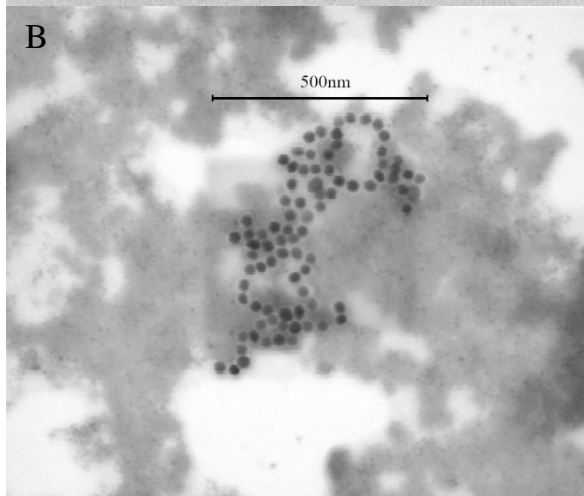
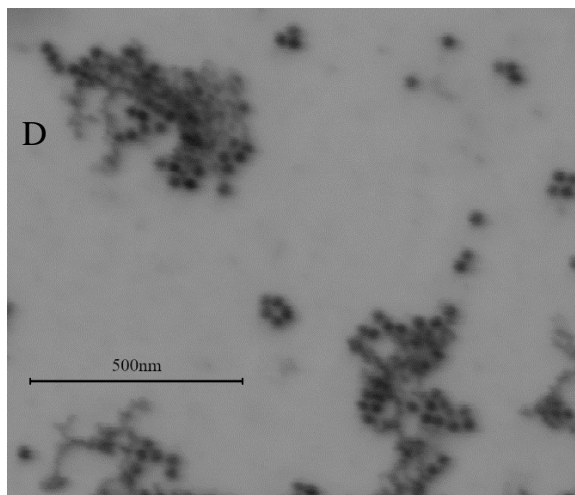
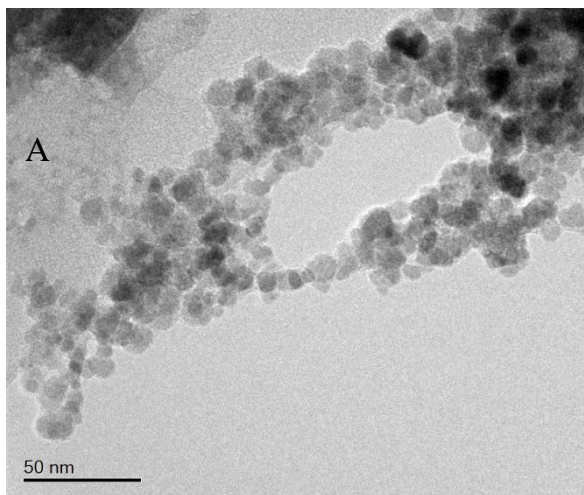
From Graph IV-V it is easy to notice that, except for the DEX sample, the peak broadening of nanoparticle samples is quite similar. Therefore, assuming the same particle shape in these samples, it is safe to conclude that they have similar radii. For DEX IONP the peak is much broader, which indicates smaller particles. The positions of the peaks do not shift with increasing Bragg angle, compared to the reference magnetite sample, indicating that there is no internal stress, which would cause deformation of the crystal lattice. The results of calculations of the particle radius are collected in table IV-1 and we observe that for most of the measured nanoparticle samples particles are of 10 nm in radius except for the DEX IONP for which particles are of about half that size.

Table IV-1 The particle size for investigated samples, derived from the XRD using the Scherer's equation and from the scanning transmission electron microscopy (for SPION Gd and DEX IONP it corresponds to the maximum counts, while for other samples it is the mean value of the fitted distribution function).

	Grain size determined from XRD [nm]	Radius (max count) from STEM/TEM [nm]
SPION CCh	9	13
SPION Gd	11	14
SPION CChB	10	7
PEG IONP	12	13
DEX IONP	4	6

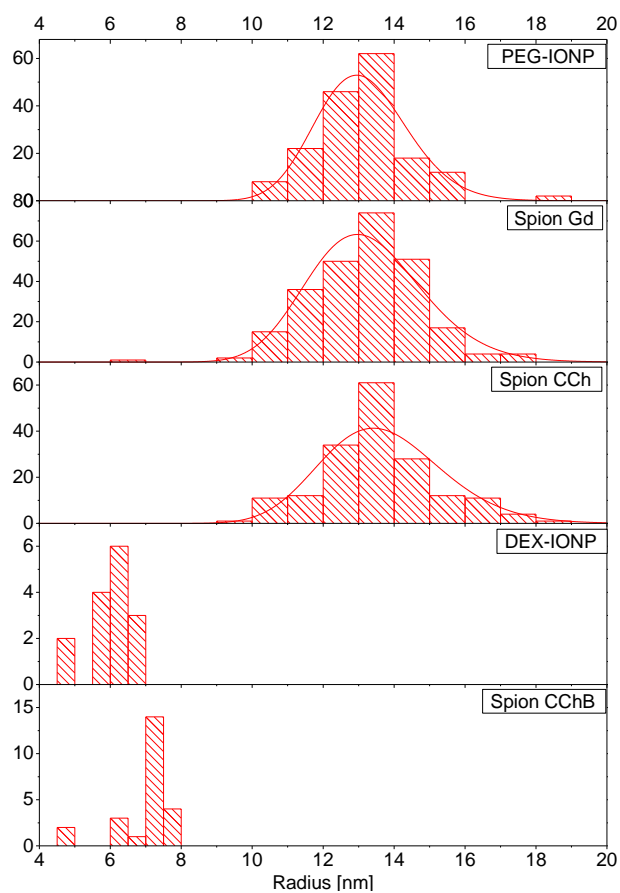
In order to verify the above XRD results, the STEM/TEM images for the samples studied were taken and the outcomes are presented in Graph IV-VI. The images of SPION-GD, SPION-CCh and PEG-IONP are of good quality, therefore, it was possible to perform computer aided analysis of particle sizes with satisfying quantity of particles of more than 200 on each image. Unfortunately, neither STEM nor TEM technique delivered clear image of the two remaining samples (DEX-IONP

and SPION-CChB). Analysis of images of those two samples was carried out by hand on small number of particles, with images sharp enough to be included in the count. Automated analysis was carried out using ImageJ software. From the qualitative description side, in the first mentioned group of three samples there are no signs of agglomeration visible since all of the particle cores appear as separate circles. Thus, one can also conclude that the shape of the particles is mostly spherical. As for the other two samples it is hard to draw any conclusions as the images are clearly overlapping with multiple layers of particles and overall blurry. It's also worth noting that TEM images were made after considerable time passed from their synthesis/production therefore the results might be affected by long term stability issues (Tadros, 2013).



Graph IV-VI STEM/TEM image of A) SPION CChB, B) PEG-IONP, C) SPION Gd, D) SPION CCh, E) DEX-IONP.

The results of analysis of images are presented in Graph IV-VII.



Graph IV-VII Particle radii distribution with fitted normal distribution function.

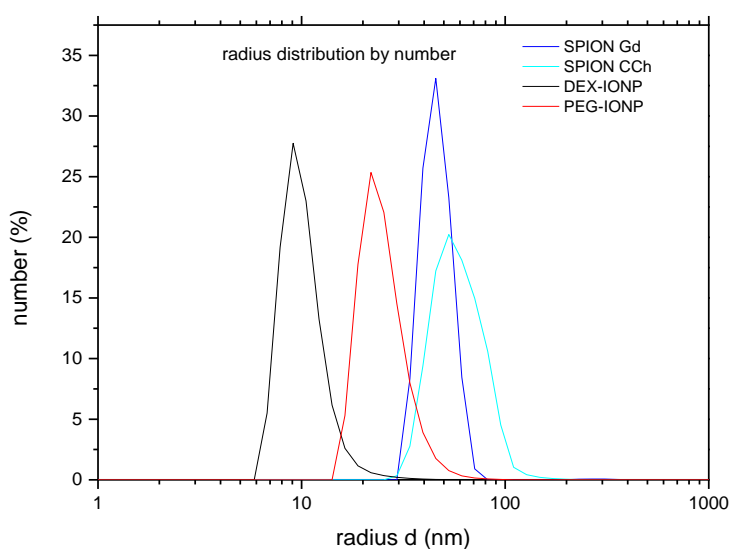
The distribution histograms were fitted with normal distribution curves and results are presented in Table IV-II.

Table IV-II Mean radii of three nanoparticle samples as obtained from the fit to the experimental data (see Graph IV-VII).

Sample	Mean radius [nm]	Standard deviation [nm]
PEG-IONP	13,1	1,3
SPION Gd	13,3	1,6
SPION CCh	13,7	1,7

It is apparent that the mean core radius is very similar in those samples, which allows for further comparison between them. The width of the distribution for those three samples is not as similar as their radii. For the IOPN-PEG it is the narrowest and SPIONS have about the same distribution width. These results are quite close to those obtained from XRD data described above and the difference can be attributed to distorted area of the surface of the nanoparticles. It also shows that the nanoparticles studied consist of single crystallites.

The data obtained from DLS are presented in Graph IV-VIII. The hydrodynamic radius distribution is similar for most of investigated samples except for the SPION-CCh, for which the distribution is much broader.



Graph IV-VIII Hydrodynamic radius distribution for investigated samples as measured with DLS.

Table IV-III Results of Dynamic Light Scattering measurements.

Sample name	Mean hydrodynamic radius (by number) d [nm]	Zeta potential ξ [mV]
SPION CCh	60,5	+32 ± 6
SPION CChB	97,5	
SPION Gd	46,5	-34 ± 7
PEG IONP	24,5	-9±4
DEX IONP	10	-21±4

The data collected from DLS are automatically analyzed by equipment software and the results are presented in Table IV-III. The mean hydrodynamic radius of SPIONs is bigger than core radius determined from XRD and microscopy confirming deposition of the shell material on them. Using the core radius obtained from XRD and TEM/STEM one can estimate the shell thickness of nanoparticles studied. There occurs a significant difference of shell thickness between SPIONs with SPION Gd having the thinnest shell of about 33 nm, the SPION CCh of about 47 nm and the thickest SPION CChB shell of about 80 nm. The two commercial samples have quite thin shell of about 11 nm and 3 nm for PEG-IONP and DEX-IONP, respectively. -

DLS measurements with applied voltage provided information on nanoparticles surface electrostatic potential, ξ . The higher this potential is, the better for stability of nanoparticles suspension, as particles stronger repel each other and therefore, do not agglomerate easily. We note that the ξ potential of SPION CChB sample was not possible to determine. The surface potential of SPION CCh was determined to be 32 mV and -34 mV for SPION Gd. The commercial samples possess a negative surface potential of -9 mV and -21 mV for PEG-IONP and DEX-IONP, respectively. This kind of surface potential can prevent agglomeration of nanoparticles (Tadros, 2013).

3. Summary of structural and particle size studies

In conclusion of this chapter the most important findings of the structural study are presented. From the XRD study it was possible to determine that the crystal structure of samples studied is of the inverse spinel type. This indicates that the synthesized and the commercial materials can be either magnetite or maghemite.

The transmission electron microscopy provided information about the particle shape and actual size of the investigated nanoparticle samples. For the three of them, SPION Gd, SPION CCh and PEG-IONP the results are quite similar, with the size of the core of about 13 nm in radius and with mostly spherical shape. There was no agglomeration effect visible for those samples as well. The results of the analysis of the other two samples was not conclusive but it can be safely stated that their core radius is less than 10 nm and there were some signs of possible degradation of the samples.

The hydrodynamic size, shell thickness and zeta potential were elucidated from the dynamic light scattering. The SPION CChB was determined to have the thickest shell and the next in descending order of shell thickness were: SPION CCh, SPION Gd, PEG-IONP and DEX-IONP. All the zeta potentials measured are in the range corresponding to a stable state of the suspensions of the respective nanoparticle materials.

These data are the basic characterization of any nanoparticles and are essential for further analysis presented in subsequent chapters of the thesis.

V. Study of basic magnetic properties

1. Magnetism in the solid state

Every atom in the universe and, thus, the matter consisting of them exhibits magnetic properties. To describe it we define magnetization M as a value of magnetic moment per unit of volume of a substance in a static state or

$$M = -\frac{N}{V} \frac{dF}{dH} \quad \text{Eq. V-I}$$

where F is the free energy, N is the number of magnetic dipoles in a given volume V and H is the magnetic field strength. To describe how magnetic field interacts with it, we define magnetic susceptibility χ as the ratio:

$$\chi = \frac{M}{H} \quad \text{Eq. V-II}$$

From the practical point of view we can define χ with respect to quantity other than volume, then the resulting χ would be described as mass or molar magnetic susceptibility. Units of these physical values in the SI system are [A/m] for M and volume χ is dimensionless. However, because of historical reasons magnetic physical values are often given in emu-CGS system as is in this part of the thesis. For the reader's convenience table V-I contains CGS to SI conversion table.

Table V-1 Conversion table of CGS and EMU units to the SI system.

Quantity	Symbo l	Unit in CGS	Conversion factor	Unit in SI
Magnetic induction	B	gauss (G)	10^{-4}	tesla (T)
Magnetic field strength	H	oersted (Oe)	$10^3/4\pi$	A/m
Magnetic moment	m	Emu	10^{-3}	$\text{A}\times\text{m}^2$
Magnetic susceptibility per unit of mass	χ_ρ	$\text{cm}^3/\text{g}; \text{emu}/\text{g}$	$4\pi\times 10^{-3}$	m^3/kg

It is the easiest to start describing magnetic systems with diamagnetism. Let's imagine a single atom with electrons circling around the core. If we look at this atom from a perspective of the Bohr model, movement of an electron produces electric current density on its orbit and by that creates a magnetic dipole with magnetic moment μ_B which value can be calculated as:

$$\mu_B = \frac{eh}{4\pi m_e} \quad \text{Eq. V-III}$$

where e is the electron charge; h is the Planck's constant and m_e is the electron mass. This quantity is called Bohr magneton and is used as a unit of magnetic moment in atomic physics. When we apply external magnetic field, electrons will respond to it according to the Lenz's law and produce electric current and thus magnetic field, with opposite direction to the applied one. In this approach, every single atom with fully occupied shell ($J=0$) would be an ideal diamagnet. In reality it isn't true and it is necessary to take into account quantum effects of magnetic field interacting with electron orbital magnetic moment. This was described by van Vleck and is called van Vleck paramagnetism. Overall the magnetic susceptibility can be written as:

$$\chi = -\frac{\mu_0 e^2 Z N}{6m_e} \sum \langle r^2 \rangle + 2N \sum_s \frac{|\langle s | \mu_B | 0 \rangle|^2}{E_s - E_0} \quad \text{Eq. V-IV}$$

where Z is the number of electrons, N is the number of atoms, $\langle r^2 \rangle$ is the mean square distance of an electron from the nucleus, $\langle s | \mu_B | 0 \rangle$ is the matrix element of orbital magnetic moment binding ground state 0 with excited state s and $E_s - E_0$ is the energy difference between those two states.

The first component in this equation is called Langevin (also called Larmor) term and the second one is van Vleck term. When a substance is diamagnetic the first factor is to be greater than the latter, so in general a substance with negative magnetic susceptibility is diamagnetic. On the other hand, if the second factor is dominant, susceptibility would be positive and such a behavior is called paramagnetism.

So far only materials with total angular momentum $J = 0$ were described. If $J \neq 0$ and, assuming that only one shell isn't fully occupied, it means that there is at least one

unpaired magnetic moment left, so the atom might be paramagnetic. The relation between the total angular momentum and macroscopic magnetic moment of an ion, μ is given by;

$$\mu = -g(LSJ)\mu_B J \quad \text{Eq. V-V}$$

where $g(LSJ)$ is the atomic Landé factor, which can be calculated for particular electronic configuration.

There are several ways to obtain equation for paramagnetic magnetization. Following Ashcroft's statistical physics approach we define free energy as $-\mu H$ and then sum for all available $2J+1$ states and we will get:

$$M = -\frac{N}{V} \mu B_J \left(\frac{\mu H}{k_B T} \right) \quad \text{Eq. V-VI}$$

where $B_J(x)$, with $x = \frac{\mu H}{k_B T}$, is the Brillouin function:

$$B_J(x) = \left(1 + \frac{1}{2J} \right) \text{ctgh} \left(1 + \frac{1}{2J} x \right) - \frac{1}{2J} \text{ctgh} \left(\frac{1}{2J} x \right) \quad \text{Eq. V-VII}$$

for $x \gg 1$ this function will reach its upper limit, so if $\mu H \gg k_B T$ the overall magnetization would be $M = -\frac{N}{V} \mu$. Such a case represents the situation with all magnetic moments aligning with the magnetic field and such a state is called saturation. In practice it is difficult to achieve, because in paramagnetic materials μ is rather small so we would need very high magnetic field and low temperature. More common situation will be when $\mu H \ll k_B T$, then it is possible to use approximation of ctgh function and reduce Brillouin function to $B_J(x) = \frac{J+1}{3J} x + O(x^3)$. If we insert it to Eq. V-VI and divide by magnetic field strength we obtain:

$$\chi = \frac{N}{V} \frac{(g \mu_B)^2 J(J+1)}{3 k_B T} = \frac{C}{T} \quad \text{Eq. V-VIII}$$

This equation is called the Curie law and describes how magnetic susceptibility depends on temperature. This simple hyperbolic relation describes paramagnetic system quite accurately if we keep in mind assumptions that it is composed of non-interacting particles and magnetic energy μH is much lower than thermal one $k_B T$.

This description of magnetic behavior is limited only to dielectric materials. In the case of metals where there are electrons in the conduction band, they will contribute to the total magnetization. Theory of magnetization of delocalized electrons was introduced by Pauli and so the property stemming from it is called Pauli paramagnetism. Another complication that one would encounter in real systems is the crystal structure of matter and its impact on magnetic moments. One of its consequences is quenching of orbital momentum. Existence of periodic electric field and exchange interaction can and often lead to creating a state in which at the minimum of energy the substance has a spontaneous magnetic moment. This group of materials is called ferromagnetics.

There are many types of magnetic ordering. Ferromagnetic (e.g. α -iron) and antiferromagnetic (e.g. hematite) are the most simple ones with neighboring magnetic moments parallel and antiparallel, respectively. Ferrimagnetics (e.g. magnetite and maghemite) are slightly more complicated structures and are similar to antiferromagnets but with two sublattices of different magnetic moments. There are also more complex magnetic structures like helical with a spiral or helical pattern of magnetic moments. So far there exists no theory adequately describing all aspects of magnetism. However, there are models providing good results within their assumptions, like the Heisenberg model that introduced a concept of exchange integral, which describes the energy of interaction of spins in a set of atoms. Another approach, which is rather simple, but still often used is the mean field approximation, which leads to the Curie-Weiss law:

$$\chi = \frac{C}{T-T_c}, T_c = \lambda C \quad \text{Eq. V-IX}$$

where: C is the Curie constant (Eq. V-VIII), T_c is the Curie temperature or Néel temperature in the case of antiferromagnetic ordering and denoted as T_N , and λ is the Weiss molecular field constant. The Curie-Weiss law is often used for determination of the magnetic ordering in the sample, as λ is proportional to the exchange field and thus it is positive in the case of ferro- or ferrimagnetic materials and negative for antiferromagnetic ones.

In any ferromagnetic material, even for a single crystal sample, the total magnetic moment measured experimentally will be smaller than the expected value or even absent if there is no magnetic field applied. This observation was explained by Weiss in 1910 by introducing the concept of magnetic domains inside of the material. Magnetic domains are areas of material with magnetic moments aligned in the same direction and they are separated by domain walls in which moments are more or less smoothly converted from one domain orientation into another. The reason that domains are created is high magnetostatic energy of uniformly aligned magnetic moments in the entire sample volume. From this perspective the minimum of energy would be achieved if moment of every atom has a random orientation. Such a state is prevented by the exchange interaction, which will stop growth of domain walls area. Ultimately, the domain structure of ferromagnetic material is dictated by a balance between the magnetic energy of the whole crystal and the energy of interaction of neighboring domains.

When external magnetic field of sufficient strength is applied to a ferromagnetic material with zero net magnetic moment it changes the balance condition by introducing an additional energy to domains that are not oriented along the applied field direction. To restore the balance and minimize the overall energy, domains oriented along the applied field direction will grow and, eventually, merge, using external magnetic field energy for this reorientation of magnetic moments. When external magnetic field is then removed, there may be no energy available for domain structure to return to its initial form, which may result in remnant non zero net magnetic moment and the corresponding remanent magnetization M_r . If the same process was to be repeated with magnetic field directed opposite, it will result in net magnetic moment with opposite direction. This process is termed magnetic hysteresis. The magnetic field strength required to set the net magnetic field back to zero is called the coercive field H_c .

An isolated atom does not exhibit any preference of magnetic moment orientation in space. However, in a solid, interactions between atoms in crystal lattice, represented by the exchange integral, can create preferential directions in which it is

easier to magnetize a ferromagnetic material. The feature resulting from that is called the magnetic anisotropy and it can have its origin either in the type of the crystal structure of the material or in the shape of an object. In the former case it is called magnetocrystalline anisotropy, and in the latter one it is called the shape anisotropy. For example, a bar shaped object would be easy to magnetize along its longest axis because of long distance dipole interactions, but for a spherical shape the presence of a preferred direction of magnetization would depend only on its crystal structure. When the magnetic moment is being forced out of the easy axis the system gains energy. This energy is called the anisotropy energy and for a uniaxial system it can be expressed with the following equation:

$$E_S = V K \sin^2(\theta) \quad \text{Eq. V-X}$$

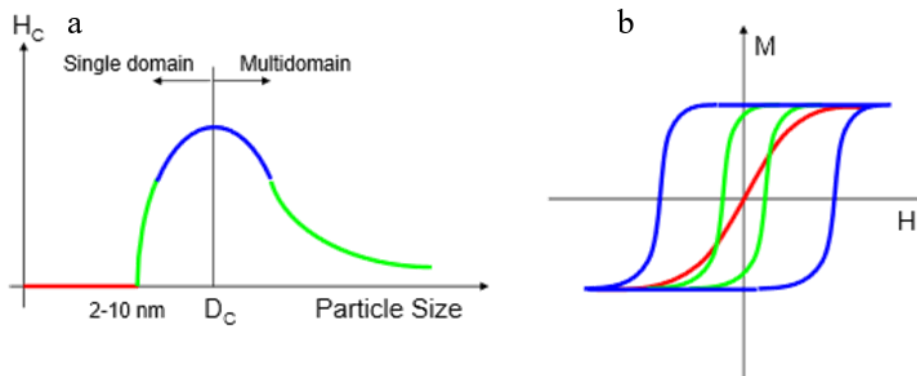
where K is the magnetocrystalline anisotropy coefficient, V is the volume and θ is the angle between the magnetic moment and the easy magnetization axis.

Magnetic properties of solids are quite complex problem, which is not fully solved analytically until now. As this thesis is not focused on the origin of the magnetic properties in any particular material, the most important part of information in this section are energy considerations. Ultimately, the difference between magnetic properties of the bulk material and these of a collection of small particles will be determined by the balance of their total anisotropy energy elements i.e. related to shape, composition, volume or domain wall forming energy.

2. Superparamagnetism

Superparamagnetism is a state of ferromagnetic and ferrimagnetic material where magnetocrystalline energy is close to or smaller than the thermal energy (Néel, 1949). This is possible to occur when particles are small enough to be a single domain i.e. there isn't enough energy in the system to create a domain wall or it is beneficial from the perspective of minimizing the overall energy. This typically happens when the diameter of particles is in a range of 3 nm – 50 nm (Cullity and Graham, 2011;

Kronmüller and Fähnle, 2003). Graph V-I-a presents an example of such dependence. The magnetocrystalline energy depends on the type of the material and its crystal structure. In the superparamagnetic state at the applied field, it is considered that the magnetization of nanoparticles is a single giant magnetic moment, a sum of all individual magnetic moments carried by the individual particles. This assumption is due to fact that in the superparamagnetic state there is no force preventing magnetic moment to align with magnetic field so there is no coercive field. Graph V-I-b presents an example of magnetic hysteresis loops for materials with different particle size. This ideal situation is described by Stoner-Wohlfarth model (Stoner and Wohlfarth, 1948) of anisotropy with non-interacting single domain particles with ellipsoidal shape and easy magnetization directed along the major axis of the ellipsoid. Energy in this model is determined only by angles between the magnetic moment, magnetic field and easy axis.



Graph V-I a) A schematic dependence of the coercive field H_c on the particle size, with D_c being critical diameter, b) dependence of the magnetization M on the external magnetic field for nanoparticles of different size, blue and green show a behavior typical for ferromagnets while red corresponds to a superparamagnet.

Unfortunately, this model does not take into account the temperature dependence of the superparamagnetic behavior or time dependent effects.

3. Néel Relaxation

Néel relaxation model is a theory developed by Louis Néel in 1949 (Néel, 1949) to explain time-dependent magnetic phenomenon known as magnetic viscosity. It is also called Néel-Arrhenius theory, after the Arrhenius equation, or Néel-Brown theory after a more rigorous derivation done by William Fuller Brown, Jr. (Brown, 1963).

Néel used his theory to develop a model of the remanent magnetization in single-domain ferromagnetic minerals which explained how these minerals could reliably record the geomagnetic field. He also modeled frequency-dependent susceptibility and alternating field demagnetization. At the end of this theoretical introduction another important model of relaxation is described, i.e. the Brownian relaxation. In order to avoid confusion, in this work the sole magnetic moment relaxation is called Néel relaxation and that related to movement of entire particles is called Brownian relaxation.

4. Mean transition time

As a result of the magnetic anisotropy of the nanoparticle, its magnetic moment has usually only two stable orientations antiparallel to each other and separated by an energy barrier. The stable orientations define the magnetic easy axis of the nanoparticle. At a finite temperature, there is a finite probability for the magnetization to flip and reverse its direction. The mean time between two flips is called the Néel relaxation time τ_N and is given by the Néel-Arrhenius equation:

$$\tau_N = \tau_0 \exp\left(\frac{KV}{k_B T}\right) \quad \text{Eq. V-XI}$$

where KV is the height of the energy barrier, a product of the magnetic anisotropy energy coefficient K and the volume V ; k_B is the Boltzmann constant, T is the temperature and their product is the thermal energy; τ_0 is the attempt time or attempt period, characteristic of the material, (its reciprocal is called the attempt frequency). Typical values of τ_0 are between 10^{-9} and 10^{-12} seconds.

The Néel relaxation time can range from a few nanoseconds to years or much longer. In particular, it is an exponential function of the particle volume, which explains why the flipping probability becomes negligible for bulk materials or large nanoparticles.

5. *Blocking temperature*

Let's assume that the magnetization of a single superparamagnetic nanoparticle is measured over a time τ_m . If this time, called usually the characteristic time of the method, is much greater than the relaxation time τ_N , the nanoparticle magnetization will flip several times during the measurement. At zero magnetic field, the measured magnetization will then average out to zero. If $\tau_m \ll \tau_N$, the magnetization will not flip during the measurement, so the measured magnetization will be equal to the initial magnetization. In the former case, the nanoparticle will be seen as fluctuating, whereas in the latter case it will be seen as apparently blocked in its initial state. The state observed of the nanoparticle (fluctuating or blocked) depends on the characteristic measurement time. A transition between fluctuating and the blocked state occurs when $\tau_m = \tau_N$. In some experimental techniques of the characteristic time τ_m of order of seconds or longer, the transition between superparamagnetism and the static state can be observed with decreasing temperature. The temperature at which $\tau_m = \tau_N$ is called the blocking temperature T_B and is given by the formula:

$$T_B = \frac{KV}{k_B \ln\left(\frac{\tau_m}{\tau_0}\right)} \quad \text{Eq. V-XII}$$

Néel's theory introduces the thermal dependence in a form of Boltzmann energy distribution and states that magnetic moment will remain still if the thermal energy is much lower than the anisotropy energy making it an energy barrier. However, Néel's theory describes only the case in which particles cannot rotate or otherwise move in their environment. Another approach, which was first discussed by Peter Debye, involves Brownian rotational motion.

6. *Brownian relaxation*

Brown relaxation theory describes movement of particles in a suspension. It was first described by Robert Brown in 1828 (Brown, 1828) and in the following years the theory has evolved as a result of contributions of several famous scientists like Albert Einstein, Jean Perrin or Marian Smoluchowski. In this work the Einstein's model will be used. In particular, its final equation describing the relation between the rotational

relaxation time τ_B , temperature T , dynamic viscosity η of a solvent and hydrodynamic radius of dispersed particles d :

$$\frac{1}{\tau_B} = D_r = \frac{k_B T}{4\pi\eta d^3} \quad \text{Eq. V-XIII}$$

where D_r is the rotational diffusion coefficient.

When conducting a measurement of water suspension where both the Néel and the Brown relaxations are possible, one should keep in mind that it would display a relaxation time referred to as effective relaxation time τ_e (Fannin and Charles, 1989; Shliomis and Raikher, 1980; Singh et al., 2009) which is described by the equation:

$$\tau_e = \frac{\tau_N + \tau_B}{\tau_N \tau_B} \quad \text{Eq. V-XIV}$$

This equation is often employed in calculations of relaxation time but in this thesis there is only PEG IONP sample that could be analyzed in this manner. Other investigated water suspension samples are already frozen when the transition to the superparamagnetic state occurs.

The Brownian rotation is not the only factor determining the particle rotation. There are also: mechanical angular momentum (I) and hydrodynamic drag (γ) that come into play when a particle is subjected to external force. In this study the force acting on the magnetic dipole moment was caused by static or alternating magnetic field. The angular momentum is usually neglected as even for micrometer sized particles it is very small (Helgesen et al., 1990; Romodina et al., 2016). The overall equation for particle rotation in an external magnetic field is then:

$$I\ddot{\varphi} = -\gamma\dot{\varphi} + m\mu_0 H \sin(2\pi f_H t - \varphi) + F(t) \quad \text{Eq. V-XV}$$

$$\gamma = \frac{k_B T}{2D_r}$$

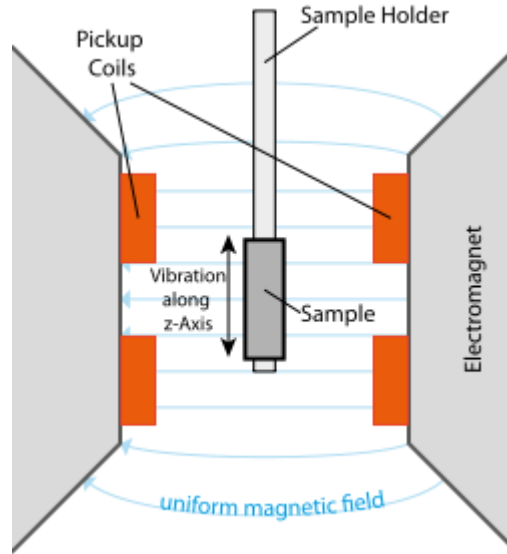
where φ is the relative angle of rotation of the particle, m is the magnetic moment of the particle, f_H is the external magnetic field frequency and $F(t)$ is the Brownian torque. This equation has no analytical solution but numerical study shows two distinct modes of the particle motion. At first, in the lower frequency range, the magnetic moment of the particle follows the magnetic field with some increasing phase difference up to $\pi/2$. Then, at frequencies higher than the critical frequency (f_{crit}) the magnetic moment of the particle precesses around the direction of the external magnetic field with a phase equal to $\pi/2$. The critical frequency can be expressed as:

$$f_{crit} = m\mu_0 H / 2\pi\gamma \quad \text{Eq. V-XVI}$$

Therefore, when a particle is free to rotate and the external field frequency exceeds the critical frequency the observed magnetic moment of the particle will be smaller than the real one. Especially in the case of Vibrating Sample Magnetometry ((VSM) or Alternating Current Magnetic Susceptibility (ACMS) methods where the measurement outcome is only the parallel projection of the magnetic moment. Additionally, in ACMS measurements, as it is phase sensitive, the “in phase” signal should diminish on approaching the critical frequency.

7. *Vibrating sample magnetometry (VSM)*

Vibrating sample magnetometry is a straightforward technique, which allows to measure the magnetic moment of a material studied. Its operation principles are quite simple and easy to understand. In the case of VSM the main physical base is the Faraday’s law of induction which was formulated already in 1831. It states that spatial or time varying magnetic field produces an electromotive force. Despite the long known principle, the first VSM device was constructed only in 1955 in MIT [Foner,1959].



Graph V-II A schematic of the vibrating sample magnetometer. (source: https://en.wikipedia.org/wiki/File:VSM_en.)

Foner’s magnetometer used a single pickup coil for the sample and a second one with known magnetic material as a reference. In the case of VSM measurement using a Physical Property Measurement System (PPMS) device there are two pickup coils wound in opposite directions so that any external change of magnetic field would cancel out, which eliminates the need of constant reference measurement.

For a sinusoidally oscillating sample, the resulting voltage is given by the following equation:

$$V_{coil} = 2\pi f C M A \sin(2\pi f t) \quad \text{Eq. V-XVII}$$

where C is a coupling constant, M is the DC magnetic moment of the sample i.e. the magnetic moment in a static magnetic field, A is the amplitude of oscillations, and f is the frequency of oscillations.

Such a vibrating sample magnetometer, in combination with a superconducting magnet and a cryostat is a part of PPMS device. This setup allows us to measure magnetic moment of a sample in wide range of temperatures and magnetic fields.

The VSM implements rather long measurement time. In a standard operation the sample oscillates with a frequency of 55 Hz, so the minimal single measurement time

τ_m is 0.018 s. With one second (or more) averaging time the results obtained correspond rather to a static state. Typical measurements made with VSM are FC-ZFC magnetization and hysteresis loop measurements, where FC-ZFC stands for the field cooled - zero field cooled. The FC-ZFC magnetization measurements were originally invented for characterization of spin glasses but they are useful for nanoparticle research as well. The idea of this type of measurements is that in the first stage, which can be viewed as a preparation stage, the sample is cooled to a desired low temperature with no external magnetic field. This allows magnetic moments in the sample to be oriented randomly. During the second stage the actual measurement is carried out with the sample heated up at small magnetic field, in the case of nanoparticles it is usually 100 Oe. As the sample gets warmer, the increase of the thermal fluctuation energy and decrease of the magnetic anisotropy allows individual particles to align with the field, so the increase of the overall magnetic moment is observed. At the point where most of particles are aligned with the field, the ZFC curve reaches its maximum and the temperature at which it happens is denoted as T_{max} . From this point the magnetic moment will decrease as smaller particles reach the energy higher than the energy barrier imposed by the external field and may flip. The last stage is to cool the sample down at the same magnetic field and measure the FC magnetization curve, which serves as a base line with all particles aligned. The FC-ZFC measurement is typically used for estimation of the blocking temperature (Hansen and Mørup, 1999). The temperature at which FC and ZFC curves merge is denoted as T_{eqq} .

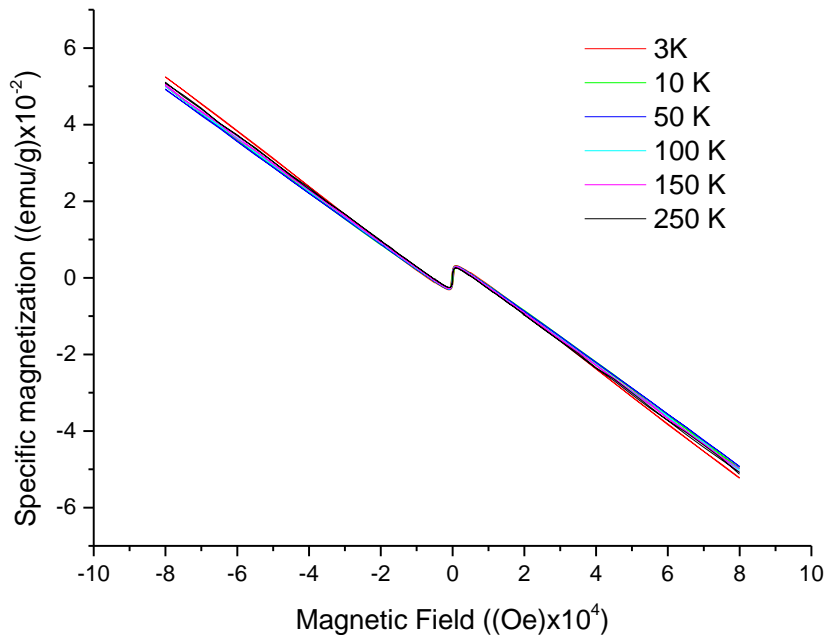
The second measurement type carried out with VSM is a measurement of magnetic hysteresis loops. This is rather straightforward measurement of magnetic moment carried out in function of the external magnetic field, at a given temperature. The magnetic field is set to change from zero to maximum (virgin magnetization curve), then in a loop from its positive to negative extremum and back. This type of measurement allows to obtain material quantities like the saturation magnetization, remanent magnetization, coercive field or saturation field.

1. Experimental

Measurements have been carried out using Quantum Design Physical Properties Measurement System (PPMS) with vibrating sample magnetometer option. Two types of measurements were conducted: low field magnetization curves and magnetic hysteresis loops. Low field magnetization measurements were made in the Field Cooled (FC) and Zero Field Cooled (ZFC) mode with field of $H=100$ Oe and in the temperature range from 323 K to 4 K. For samples measured in a liquid suspension the temperature range was from 3 K to 250 K and 250 K to 323 K and they are presented in separate graphs. Magnetic hysteresis loops were made starting from $H= 80$ kOe at 3 K or 4 K, 10 K, 50 K, 100 K, 150 K, 250 K, 300 K and 350 K although some of them were of unsatisfying quality and are not included in here. As the equipment requires vacuum in the sample chamber to work properly it was necessary to seal the sample container using its thermoplastic properties. It was found that measurements in the liquid phase are a contamination threat to the equipment. Therefore, a part of results presented was obtained for a dried form and such cases are indicated in the sample name. Additionally, the FC curve was measured as the sample was cooled down, instead of first cooling it down and then measuring during heating it up, since both measured curves showed no difference for exemplary samples and it allowed us to save one day of the measurement time per sample. For all the temperature dependent measurements the temperature was stabilized at each measurement point prior to the measurement.

2. Results and discussion

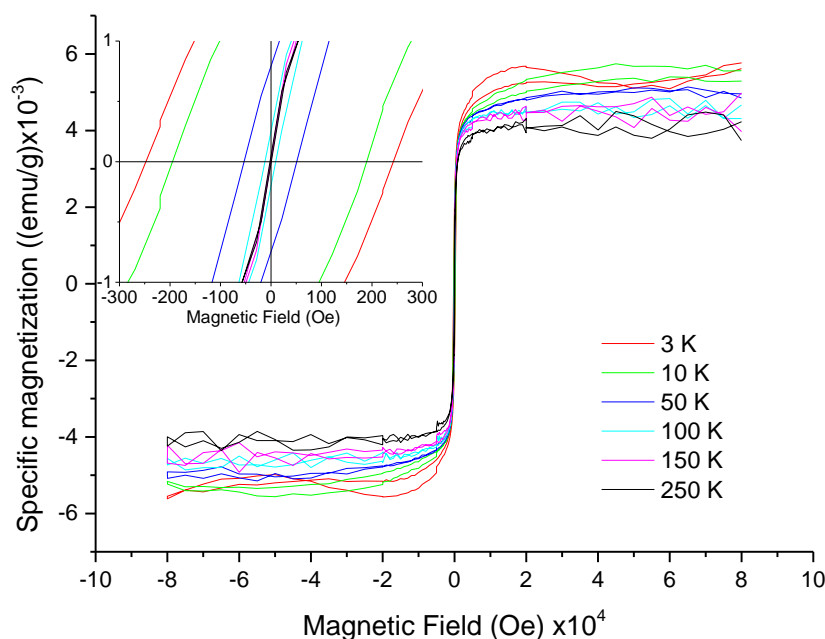
Graph V-III presents typical measurements of the magnetic hysteresis loop obtained on a sample prepared as nanoparticles in water suspension, these particular results are for the SPION Gd sample.



Graph V-III Magnetic hysteresis loops of the SPION-Gd water suspension sample carried out at different temperatures.

Hysteresis loops are dominated by the diamagnetic contributions from water and the sample container. In order to enable the analysis of the data the diamagnetic part was subtracted from the raw data. In the subtraction process straight lines were fitted to linear parts of the plot i.e. typically from 50 kOe to 80 kOe, then the obtained four values of slopes were averaged and a straight line with the resulting slope was subtracted from the data. Resulting hysteresis loops are presented in Graph V-IV. The hysteresis loops obtained resemble the Brillouin function although their shape is dictated by the particle size distribution rather than interactions of magnetic dipoles. One can notice that the saturation magnetization is inversely proportional to temperature, which is expected for a paramagnetic material according to the Curie-Weiss law. An inset in Graph V-IV presents enlarged area around the zero external

magnetic field. The coercive field at 250 K is close to zero and it strongly increases with decreasing temperature. This indicates that the blocking temperature for this sample is between 250 K and 150 K in a measurement with 55 Hz frequency.

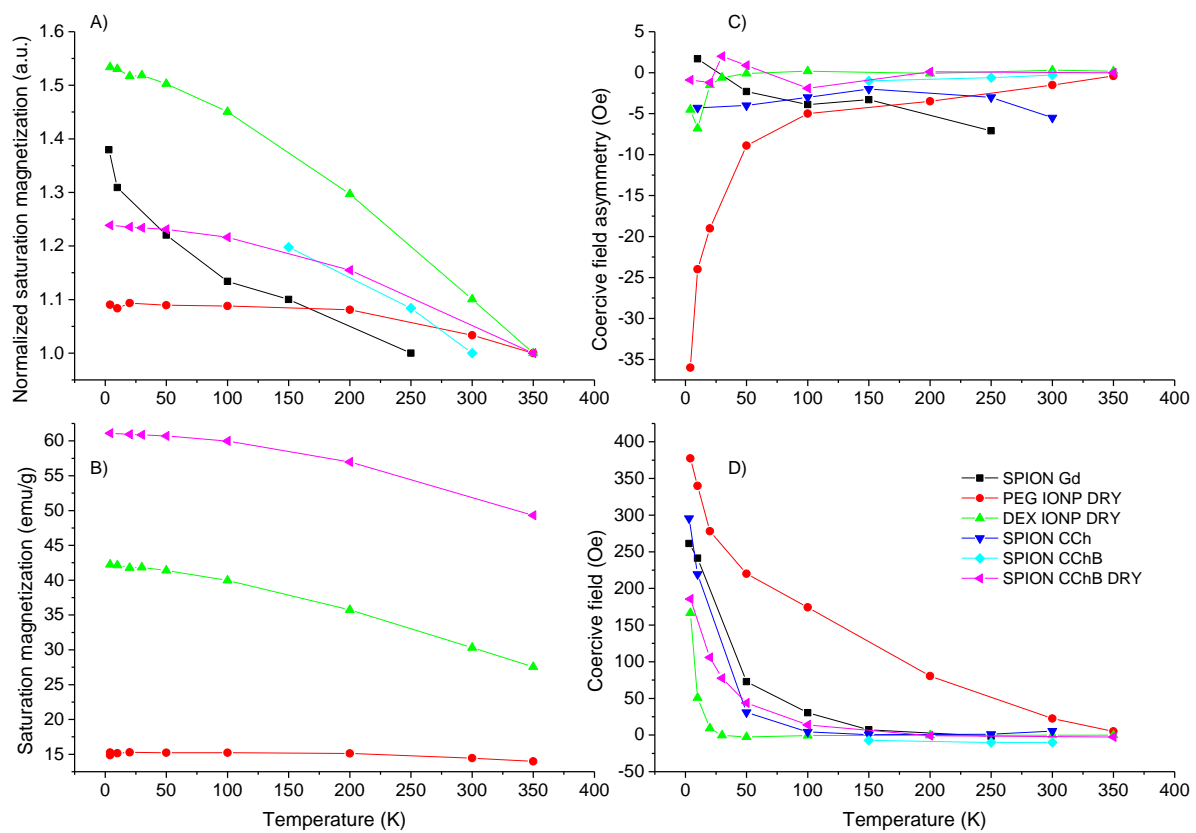


Graph V-IV Magnetic hysteresis loops of the SPION-Gd sample after subtraction of the diamagnetic contribution from loops presented in Graph V-III. Inset shows enlarged area around the zero external magnetic field.

The coercive field is symmetrical, within the uncertainty margin, at all the temperatures, indicating that a two state model (i.e. Néel) is valid for this sample as an intermediate state would bias the coercive field towards one direction. Unfortunately, the value of the saturation magnetization in the samples in water suspension does not carry any useful information as the concentration of the specimens haven't been determined prior to the measurement.

Raw measurements of the hysteresis loops of the remaining specimens are similar and are not presented here (the remaining hysteresis loops are presented in the appendix). Their analysis was conducted in the same way as described above and the parameters obtained are discussed below. Values of the coercive field were adjusted to account for the residual field of the superconducting magnet. This field was

determined by measuring the hysteresis loop of the reference palladium sample in the same magnetic field range. As palladium is paramagnetic, if any coercivity would occur, it is due to the magnet residual field. The coercive field asymmetry has been calculated by a linear interpolation of the data points adjacent to zero magnetic moment line for both falling and rising slopes. This interpolation and estimation of the residual field of the magnet contributes both to the uncertainty margin of the derived value of the coercive field and its asymmetry, which is estimated to be of 5 Oe.



Graph V-V Cumulative graph of temperature dependences of: a) Saturation magnetization normalized to its value at the highest measurement temperature; b) Saturation magnetization for dried samples; c) Coercive field asymmetry d) Coercive field. Solid lines are only a guide to eyes.

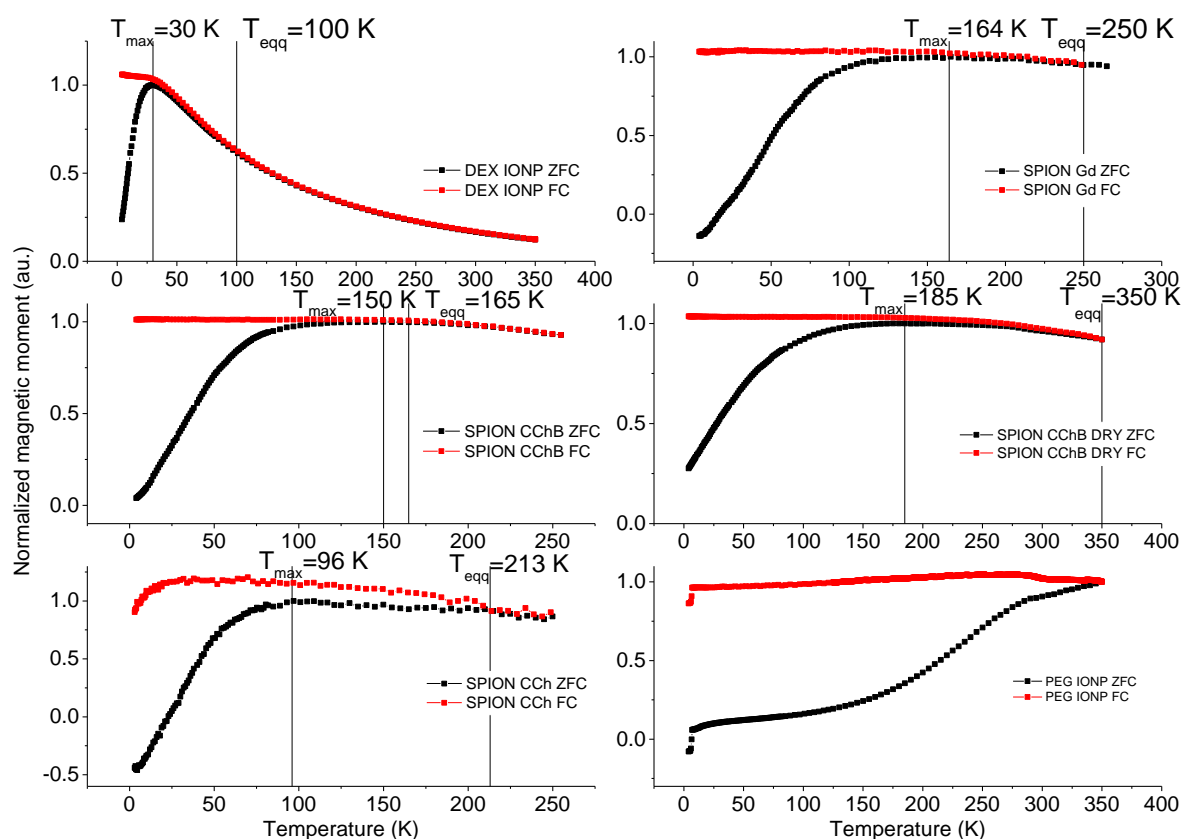
All the samples measured exhibit increase of the saturation magnetization with decreasing temperature. Only in the case of the SPION Gd sample it shows a hyperbolic-like dependence which is due the addition of paramagnetic gadolinium ions to its shell. For the remaining samples the normalized saturation magnetization

increases asymptotically to the maximal value as expected for a ferromagnetic single domain material. The rate of this increase reflects the distribution of the anisotropy energy in the sample nanoparticles. In the case of the SPION CCh, due to low concentration of nanoparticles in the suspension, the hysteresis loop measurements were too noisy to reliably estimate values of the saturation magnetization. For the dried SPION CChB DRY sample all the quantities obtained follow different trend compared to the one dispersed in water. This is quite important as it indicates that magnetic properties of these materials can differ in different environments. This can be in particular due to larger distances of nanoparticles dispersed in suspension

Lack of the coercive field indicates the superparamagnetic state of the material. As can be seen the PEG IONP sample shows the coercive field different from zero in the entire temperature range studied, which indicates that its nanoparticles are not superparamagnetic. In principle, this could be explained by different size of its core, however, it does not differ much compared to other SPION samples as concluded from XRD and STEM. Therefore, the effect observed must be the result of a higher magnetocrystalline anisotropy of the core material in this sample. This seems to be possible as the PEG IONP sample exhibits strong asymmetry of the coercive field, which is biased towards one direction of the field. This is likely to originate from crystal defects causing presence of antiferromagnetic regions and interaction between ferro- and antiferromagnetic phases (Gumieniczek-Chłopek et al., 2020; Wu et al., 2018). For the SPION samples the coercive field decreases to zero between 200 K and 250 K and for the DEX IONP around 50 K. Low blocking temperature of the DEX IONP sample can be easily explained by its small core size. At this point it is hard to draw any conclusions about the influence of modifications of SPION samples on their blocking temperature because of insufficient data point coverage.

The saturation magnetization of dried samples is in agreement with values reported by other researchers for magnetite particles of similar size [Sim,2020] with exception of the PEG IONP which exhibits surprisingly low saturation magnetization value. This, however is consistent with possible presence of antiferromagnetic regions of largely compensated Fe moments as deduced from asymmetry of the hysteresis

loops. Although the technique for extracting the ferromagnetic signal from the experimental data assumes that the particles studied reach saturation magnetization between 70 kOe and 90 kOe, which is not always the case, especially for blocked particles at low temperatures, the error due this assumption is not high and, more importantly, very similar for all samples. Therefore, the values obtained can be quite reliably compared.



Graph V-VI FC-ZFC magnetization curves of the samples studied normalized to the maximum of the ZFC curve. Vertical lines mark the temperatures of the maximum moment and the divergence of the FC and ZFC curves.

The FC-ZFC measurements are primarily carried out in order to obtain the blocking temperature and, possibly, its distribution. Results of measurements are presented in Graph V-VI for all the samples studied. It is important to note that the blocking temperature describes well only a single particle. In the case of an ensemble of particles with distribution of size and shape the interpretation is more difficult. To address this issue the blocking temperature values must be provided together with the information regarding the statistical distribution function. In this thesis the analysis of

the FC-ZFC curves is done using two approaches. The first one is the simplest possible, as just the T_{max} temperature is taken as an indication of the blocking temperature, since it represents a temperature at which most of the particles are already in the superparamagnetic state. This value is fairly sensitive to the applied magnetic field, but using the same measurement procedure allows for a qualitative and quantitative comparison between the samples. In the second approach a technique of estimating a median blocking temperature, T_{Bm} introduced by Hansen and Morup (Hansen and Mørup, 1999) will be employed. The results of both analyses are presented in Table V-II.

Table V-2 Results of analyses of FC-ZFC curves.

SAMPLE	T_{max} [K]	T_{eqq} [K]	T_{Bm} [K]	σ_{Tbm} [K]
DEX IONP	30	100	16	1,01
SPION CCh	96	213	53	0,80
SPION Gd	164	250	98	0,56
SPION CChB	150	165	102	0,29
SPION CChB DRY	185	350	105	0,71

The results are partly in agreement with findings of XRD studies. DEX IONP sample, which has the smallest nanoparticles shows the lowest blocking temperature. For the SPION Gd and CChB samples the blocking temperature is similar and T_{max} is in the range 160 K to 180 K and values of T_{Bm} are of about 100 K. However, the SPION CCh sample has significantly lower characteristic temperatures with $T_{max} = 96$ K and $T_{Bm} = 53$ K. The results obtained bear rather high uncertainty, as for all SPION samples measured dependences are flat (see Graph V-VII). This flattening is most likely caused by a distribution of particle sizes. We can only compare σ_{Tbm} with the standard deviation of the particle size obtained from XRD (Table IV-II) for SPION Gd and SPION CCh samples, where σ_{Tbm} is significantly larger for the SPION CCh sample, while the size distribution is similar. In all of the samples studied the temperature of maximum of magnetic moment seems to be a good approximation of

blocking temperature as the temperature at which the coercive field vanishes are similar.

In principle, there are other, more advanced ways to analyze FC-ZFC curves. However, since results of ACMS and Mössbauer spectroscopy measurements enable a more precise estimation of the blocking temperature, further analysis of magnetization curves would be redundant and results obtained from simple approaches are sufficient to serve as a first estimation.

As mentioned above, the PEG IONP sample does not enter the superparamagnetic state at measured temperature range but its behavior is similar to that of other samples, indicating that it might become superparamagnetic at higher temperatures. This difference was unexpected as its core size determined from XRD measurements is similar to those of SPION samples, but it has a larger magnetic anisotropy.

3. Summary of basic magnetic properties studies

Measurements of basic magnetic properties confirm the superparamagnetic nature of the materials studied, as the coercive field vanishes at around 200 K for SPION samples and 30 K for the DEX IONP sample. The PEG IONP sample does not enter the superparamagnetic state at measured temperature range but it might become superparamagnetic at higher temperatures.

Hysteresis loop measurements provided information about the saturation magnetization. For the dried sample of SPION Gd it amounts to 64 emu/g and 54 emu/g at 4 K and 300 K, respectively, which is within the expected range for this type of materials (Coduri et al., 2020). The IONP samples show lower values of M_s and a pronounced exchange-bias-like effect which indicate a presence of antiferromagnetic regions in it. This is consistent with its much higher blocking temperature, which could be attributed to a much higher magnetic anisotropy, despite particle size being similar to that of other samples. The SPION Gd sample at low temperatures exhibits a hyperbolic temperature dependence of the saturation magnetization, which could be due to presence of gadolinium in the shell of its nanoparticles.

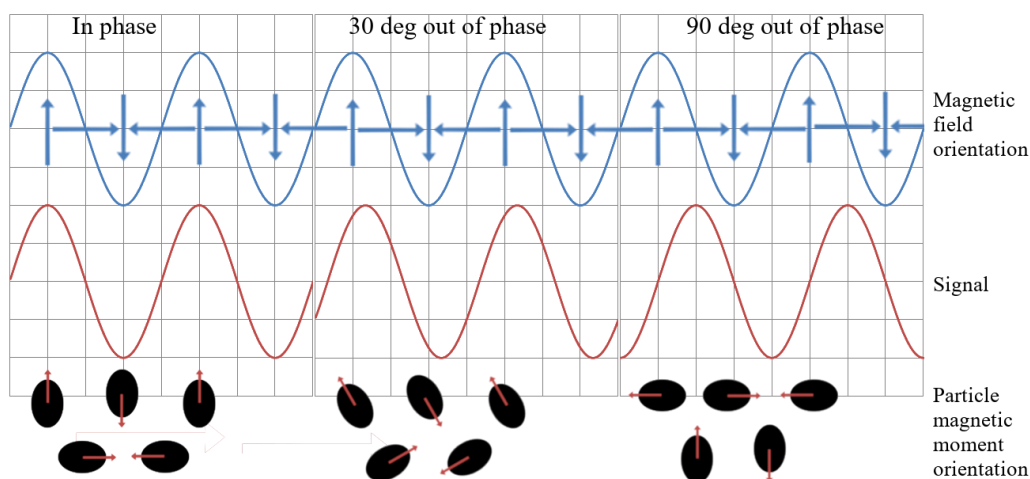
The median blocking temperature determined from the FC-ZFC curves amounts to 16 K, 53 K, 98 K, 102 K, 105 K, for the DEX IONP, SPION CCh, SPION Gd, SPION CChB and dried SPION CChB samples, respectively. Values of T_{Bm} are consistent for the SPION samples, except for the SPION CCh, which shows significantly lower value. This might be due to the influence of the modification, but might also be also be caused by poorer data quality for that sample.

Measurements carried out on dried and dispersed in water SPION Gd sample show noticeable differences indicating that the environment is an important factor, which should be taken into consideration during interpretation of results obtained and in planning possible applications of superparamagnetic nanoparticles.

VI. Magnetic dynamics

1. Alternating current magnetic susceptometry (ACMS)

ACMS is a method of measuring magnetic moment of a sample via measurement of the voltage induced in the reception coil by variable magnetic flux passing through the sample and coil. This allows for measuring not only the in phase magnetic moment, but also the out of phase part that corresponds to the absorption by the sample. ACMS is particularly sensitive to the magnetic phase transitions, therefore, it is often utilized in studies on superparamagnetism, superconductivity and other phenomena involving change of the type of magnetic order or the type of its magnetism.



Graph VI-I Principle of the phase sensitive ACMS measurement. The top part shows time dependence of the external driving AC field (blue) and the signal from magnetic nanoparticles (red), which can be phase shifted depending on the relative orientation of magnetic moments of nanoparticles.

During AC magnetic measurements a small AC driving magnetic field applied to the excitation coil is superimposed on the constant magnetic field causes a time-dependent moment changes in the sample. The time evolution of the moment induces an electric voltage in the pickup coils, allowing for a measurement without sample motion. The detection circuitry is configured to detect only in a narrow frequency range, normally at the fundamental frequency (that of the AC drive field) with lock-in amplifier. In order to understand what is measured in AC magnetometry, let us first consider very low frequencies, where the measurement is the most similar to the DC

magnetometry (Graph VI-I, in phase). In this case, the magnetic moment of the sample follows the $M(H)$ curve that would be measured in a DC experiment. As long as the AC field is small enough, the induced voltage is proportional to the moment and the frequency, analogously to the relation in Eq. VI-I. The susceptibility is given by the formula:

$$\chi_{AC} = \left(\frac{dM}{dH} \right) \quad \text{Eq. VI-II}$$

$$H(t) = H_{AC} \sin(2\pi ft) \quad \text{Eq. VI-III}$$

where H_{AC} is the amplitude of the driving field $H(t)$, f is the driving field frequency, and χ is the magnetic susceptibility, which is the quantity of interest in the AC magnetometry. As the constant applied magnetic field is changed, different parts of the $M(H)$ curve are accessed, giving the respective differential susceptibility. One advantage of the AC measurement is already evident: the measurement is very sensitive to small changes in $M(H)$. Since the AC measurement is sensitive to the slope of $M(H)$ and not to the absolute value, a small magnetic moment change can be detected even when the absolute moment is large.

At frequencies higher than those considered above, the AC moment of the sample does not follow the DC magnetization curve due to dynamic effects in the sample like kinetic drag in a viscous fluid or an interatomic interactions in a solid (Graph VI-I out of phase). For this reason, the AC susceptibility is often termed as the dynamic susceptibility. In this higher frequency case, the magnetization of the sample may lag behind the drive field, an effect that is detected by the magnetometer lock-in circuitry. Thus, the AC measurement yields two quantities: the magnitude of the susceptibility, χ , and the phase shift, φ (relative to the driving signal). Alternatively, one can think of the susceptibility as having an in-phase, or real, component χ' and an out-of-phase, or imaginary, component χ'' . The two representations are given by the expression:

$$\begin{aligned} \chi' &= \chi \cos \varphi \\ \chi'' &= \chi \sin \varphi \end{aligned} \Leftrightarrow \begin{aligned} \chi &= \sqrt{\chi'^2 + \chi''^2} \\ \varphi &= \arctan\left(\frac{\chi''}{\chi'}\right) \end{aligned}$$

Eq. VI-IV

The real component is also called the dispersion part. In the limit of low frequency of the driving field, where AC measurement is the most similar to a DC measurement, the real component χ' is just the slope of the $M(H)$ curve discussed above.

The imaginary component, χ'' , termed also the absorption part, indicates a dissipative processes in the sample as the lag is caused by a force opposing the magnetic moment change. In electrically conductive samples, the dissipation is also due to eddy currents. Relaxation and irreversibility of magnetic moment in spin-glasses give rise to a nonzero χ'' . In the ferromagnetic materials, a nonzero imaginary susceptibility can indicate an irreversible domain wall movement causing magnetic hysteresis. Also, both χ' and χ'' are very sensitive to thermodynamic phase transitions, and are often used to measure transition temperatures. AC magnetometry allows one to probe all of these interesting and important phenomena and properties.

In this work several types of measurements are presented, like χ vs. temperature, χ vs. driving field frequency, χ vs. AC field amplitude or χ vs. constant field bias. The expected outcome of the measurement of superparamagnetic material is a narrow spike in the absorption component of the susceptibility at the blocking temperature for the given frequency, if the sample was completely uniform. However, in real samples, the nanoparticle size and shape distribution result in a broadening of that spike. Increasing the AC field amplitude should also broaden the absorption spike but in measurements presented in this thesis this effect was masked by the broadening due to the size distribution.

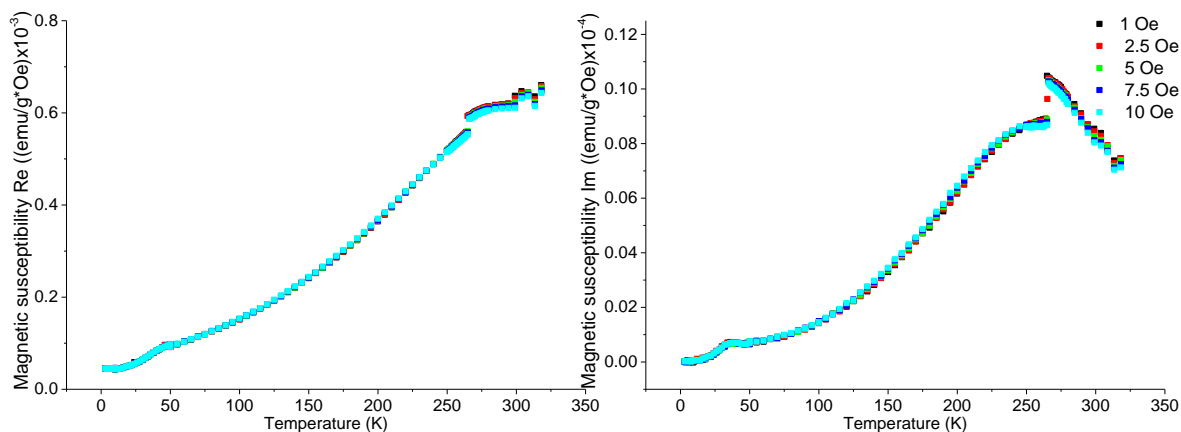
1. Experimental

All the measurements have been carried out at the Quantum Design Physical Properties Measurements System (PPMS) with ACMS option, which allows the user to carry out measurements in the temperature range from 2 K up to 350 K. The low

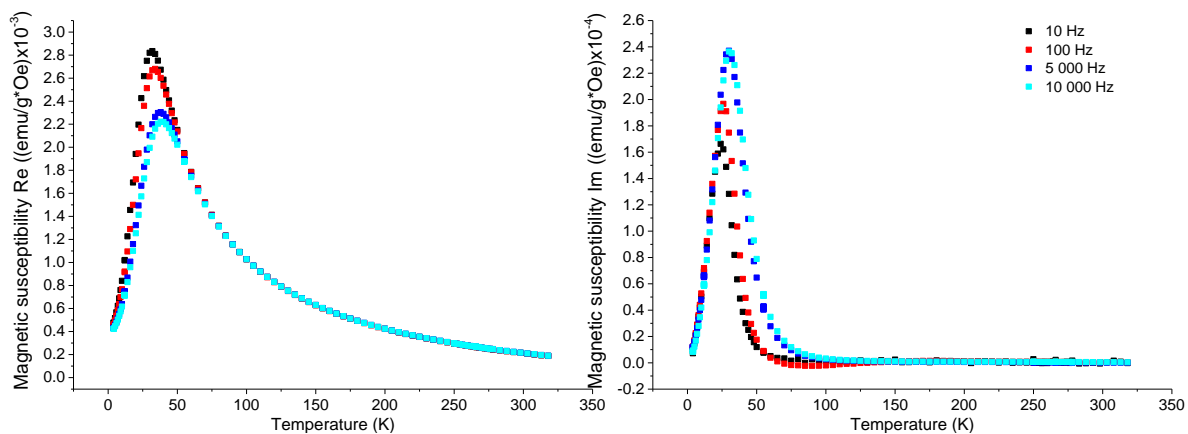
temperature region is of interest because it allows for probing magnetic moment in the blocked state. On the other hand, investigated materials are to be potentially used for biomedical applications and, therefore, it is important to know their properties in a region around the human body temperature. Most measurements were conducted with five distinct amplitudes and frequencies of the AC field, namely 2.5 Oe, 5 Oe, 7.5 Oe, 10 Oe and 10 Hz, 100 Hz, 1000 Hz, 5000 Hz, 10000 Hz. All the samples were measured in their liquid suspension. The PPMS system was not inherently designed to operate with liquid samples as it requires vacuum to reach low temperatures (and eliminate influence of liquid oxygen on the outcomes). In order to avoid these problems samples were injected into polypropylene capsules and then sealed with the use of its thermoplastic properties to ensure that water doesn't leave the capsule during the measurement. Below, results of measurements of the AC magnetic susceptibility as a function of temperature are shown. For every sample they are separated into two, the absorption and the dispersion parts.

2. Results and discussion

Measurements taken at a given temperature with various amplitudes of the AC magnetic field reveal that resultant magnetic moment and its real and imaginary components change linearly with magnetic field amplitude, i.e. the magnetic susceptibility at a given temperature does not depend on the AC field amplitude. This feature is observed in all the samples, therefore, as an example of this behavior measurement results only for the SPION Gd sample are shown in Graph VI-II.



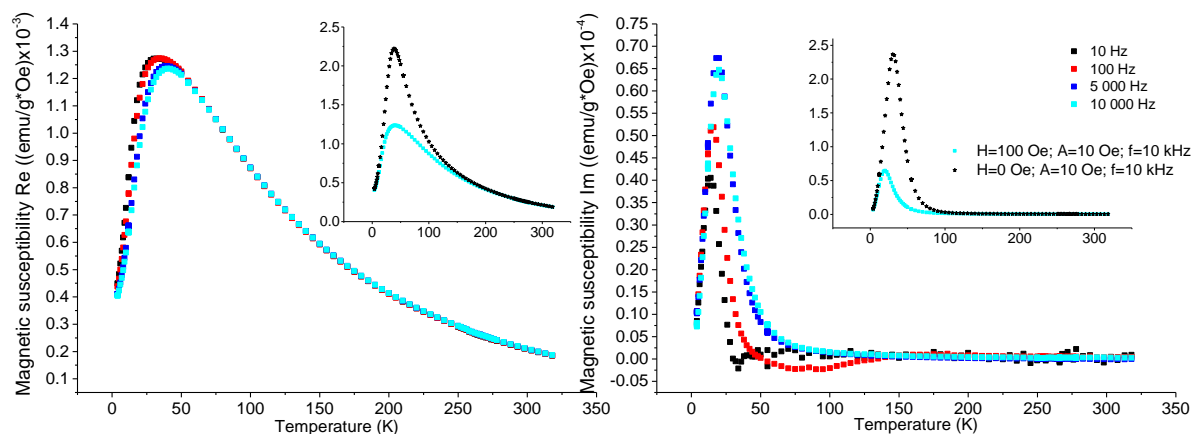
Graph VI-II Temperature dependence of the magnetic susceptibility of the SPION Gd sample without constant external field at the AC field frequency of 10 kHz and various amplitude. The dispersion part is shown in the left panel and the absorption part is presented in the right panel.



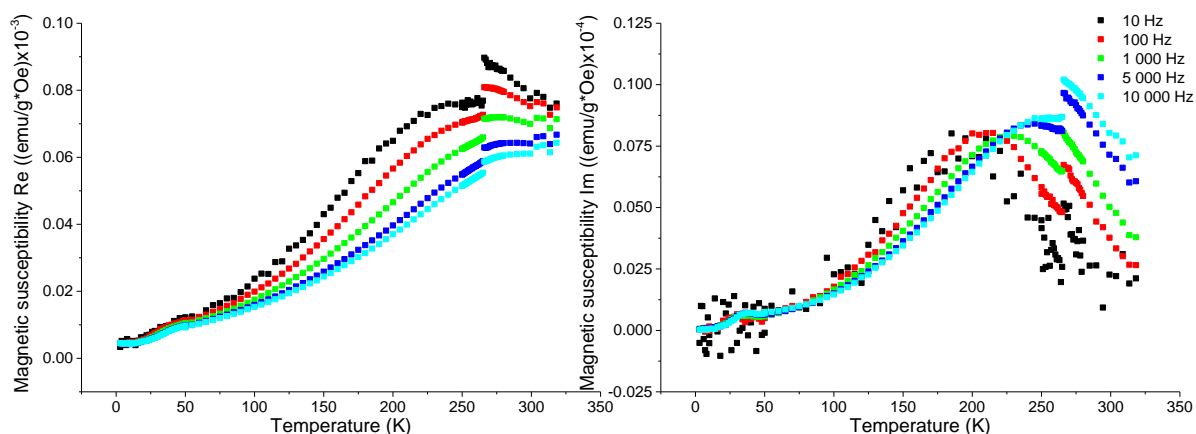
Graph VI-III Temperature dependence of magnetic susceptibility of the DEX-IONP sample without constant external field and with AC field amplitude of 10 Oe and various frequency. The dispersion part is presented in the left panel and the absorption part is shown in the right panel.

In Graph VI-III the results of temperature dependent measurements of both parts of magnetic susceptibility without external field for the DEX IONP sample are presented. As was mentioned above, a spike appears in the absorption part of the susceptibility at all frequencies. In the dispersion part it is much broader. The maximum of magnetic susceptibility appears at around 32 K and 30 K in absorption and dispersion part, respectively. Above the temperature of this maximum the susceptibility decreases hyperbolically. The real (dispersion) part is roughly one order of magnitude bigger than the imaginary (absorption) part. The value of the dispersion part of magnetic susceptibility is higher for lower frequencies, while for the absorption part the behavior is opposite. For both parts the maximum shifts towards higher

temperatures with increasing frequency as expected from the Néel-Arrhenius formula. In Graph VI-IV similar measurements are presented, but at constant magnetic field of 100 Oe. The most noticeable difference is that the susceptibility maximum is decreased and shifted towards lower temperatures particularly in the absorption part, where the peak gets narrower.

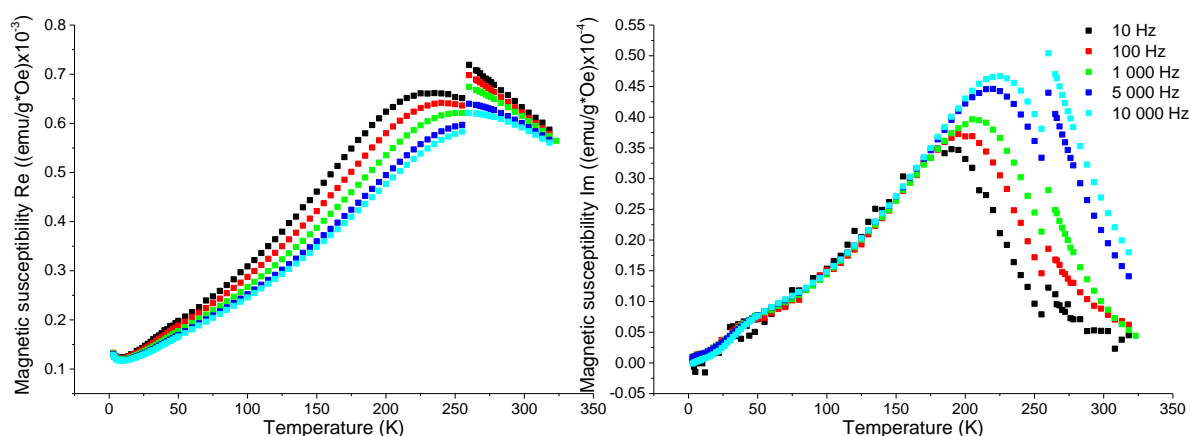


Graph VI-IV Temperature dependence of magnetic susceptibility of the DEX-IONP sample at constant external field $H=100 \text{ Oe}$ and with AC field amplitude A of 10 Oe for various frequencies. The dispersion part is shown in the left panel and the absorption part is presented in the right panel. (Insets show comparison with measurements without constant external field at the ac field amplitude $A=10 \text{ Oe}$ and frequency of 10 kHz .)



Graph VI-V Temperature dependence of magnetic susceptibility of the SPION Gd sample without constant external field and with AC field amplitude of 10 Oe at various frequencies. The dispersion part is shown in the left panel and the absorption part is presented in the right panel.

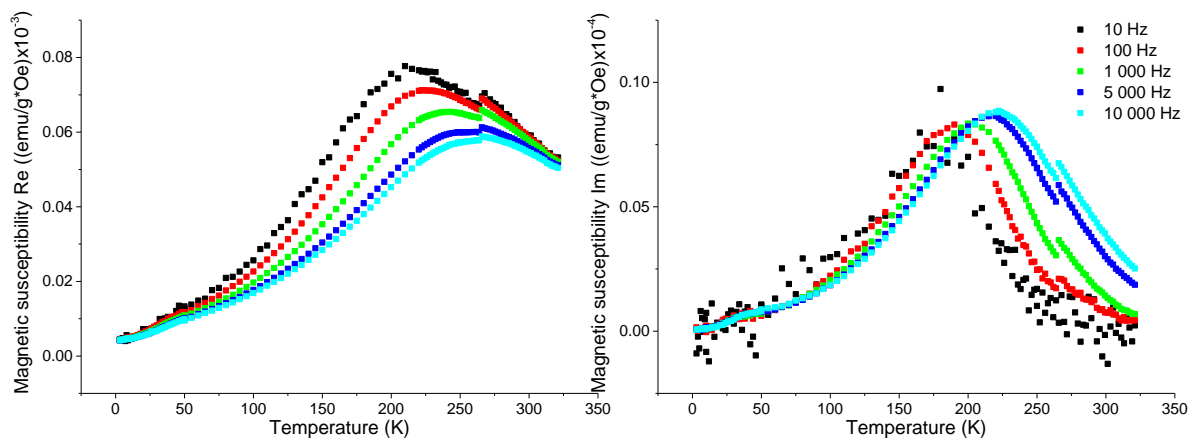
Graph VI-V shows results obtained for the SPION Gd sample. Compared to results of the DEX IONP one immediately notices that the dependences are different, e.g. there is no sharp spike in the absorption part. Additionally, in both parts of the magnetic susceptibility there appears a step at 270 K, which is due to freezing of the suspension. Similarly to the DEX IONP sample the maximum shows a strong frequency dependence and shifts from 180 K to 250 K with increasing frequency. The maximum value of the magnetic susceptibility is higher for lower frequencies in the dispersion part, but in the absorption part the opposite tendency is visible. There also appears a shoulder visible at low temperatures (around 50 K). As such a feature is observed for the most of the samples at a similar temperature of 50 K, this could be attributed to magnetic ordering of oxygen dispersed in the water or absorbed in a Teflon tape which was taped around the sample container for possible leak containment. Such a feature was also recently observed in metal oxide systems (Okunev et al., 2016), although this interpretation may sound controversial.



Graph VI-VI Temperature dependence of magnetic susceptibility of the SPION CChB sample without constant external field and with AC field amplitude of 10 Oe at various frequencies. The dispersion part is presented in the left panel and the absorption part is shown in the right panel.

Graph VI-VI presents data obtained for the SPION-CChB sample. In this case the magnetization curves are broader and the temperature of susceptibility maximum is located at slightly different temperature range, i.e. from 220 K to 260 K in the dispersion part and 200 K up to 240 K in the absorption part. The frequency dependence of the susceptibility maximum is similar as in other samples. Like for the SPION Gd sample, there is a sharp step at 260 K and a shoulder at low temperatures

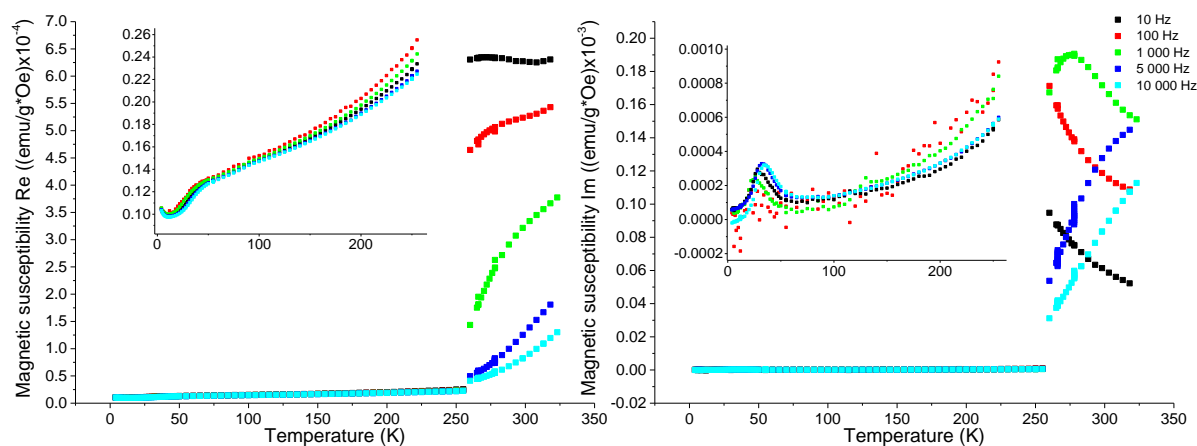
(around 50 K). In the dispersion part at very low temperatures a small upturn appears with decreasing temperature, reminiscent of the paramagnetic behavior, unlike in other SPION samples.



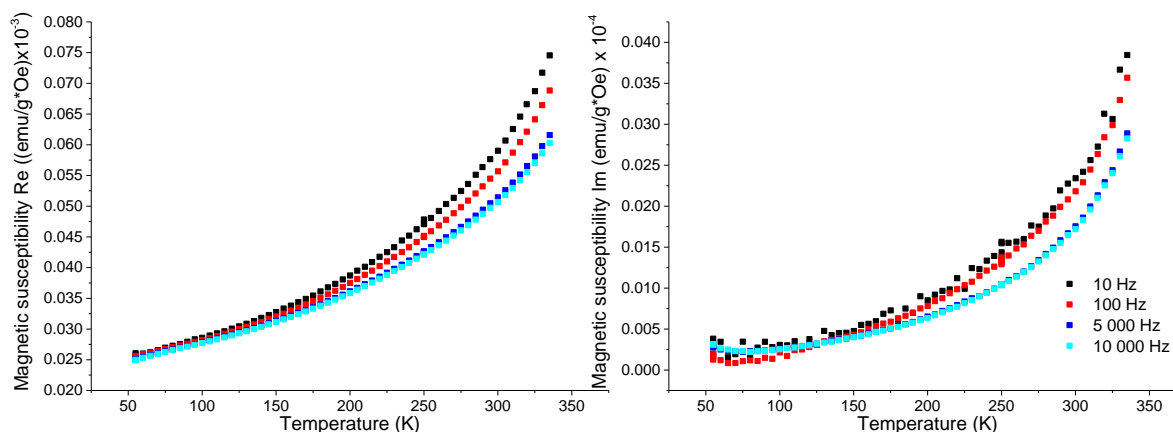
Graph VI-VII Temperature dependence of magnetic susceptibility of the SPION CCh sample without constant external field and with AC field amplitude of 10 Oe at various frequencies. The dispersion part is presented in the left panel and the absorption part is shown in the right panel.

The results for pristine, unmodified in any way SPION CCh are shown in graph VI-VII and one can notice that the temperature and frequency dependence of the magnetic susceptibility is similar to that of the SPION CChB sample. Again, peaks are rather broad, the temperature of maximum susceptibility is in a range from 200 K to 250 K for the dispersion part and from 190 K up to 230 K for the absorption part. There is also a sharp step at 260 K and a shoulder at low temperatures (around 50 K).

In Graph VI-VIII results for the PEG-IONP sample are presented. Magnetic susceptibility maximum is clearly visible only for one AC field frequency (1 kHz), only in the absorption part and occurs at 276 K. In other measurements it is probably located beyond the measurement range. In all the results there is a huge step between 255 K and 260 K visible, which corresponds to the freezing point, and another maximum occurring at 32 K. Value of magnetic susceptibility is higher for lower frequencies in the whole temperature range in the dispersion part. Ratio between absorption and dispersion part is around one order of magnitude. At very low temperatures one can again notice paramagnetic-like dependence in the dispersion part.

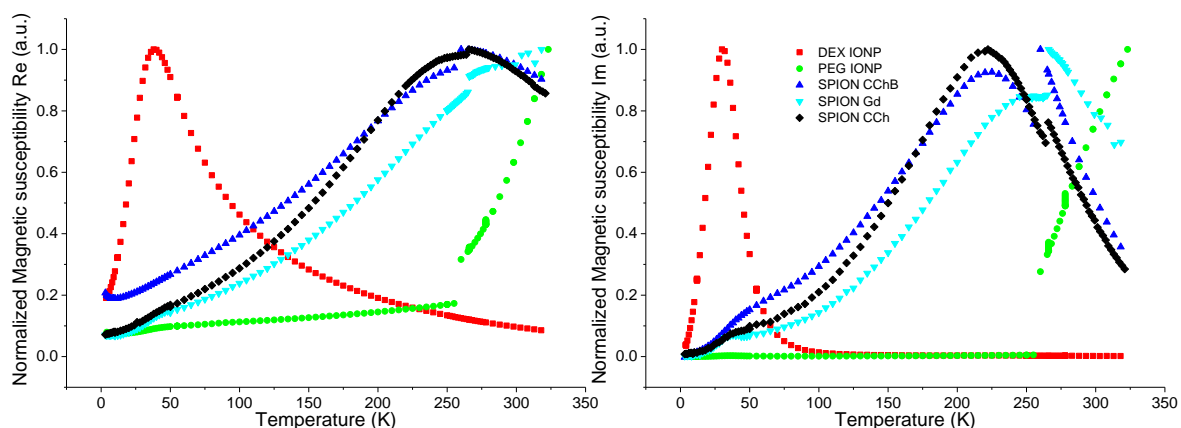


Graph VI-VIII Temperature dependence of magnetic susceptibility of the PEG IONP sample without constant external field and with AC field amplitude of 10 Oe at various frequencies. The dispersion part is presented in the left panel and the absorption part is shown in the right panel. Insets show enlarged view in the temperature range below freezing temperature.



Graph VI-IX Temperature dependence of magnetic susceptibility of the DRY PEG IONP sample without constant external field and with AC field amplitude of 10 Oe at various frequencies. The dispersion part is shown in the left panel and the absorption part is presented in the right panel.

Graph VI-IX presents results of ACMS measurements of the dried out PEG-IONP sample. One immediately notices that they are different than those presented above for other samples. There is no step at about 260 K, which confirms that in previously discussed samples it was due to freezing. The susceptibility maximum is most likely above 320 K.



Graph VI-X Temperature dependence of magnetic susceptibility normalized to its maximum of all of the samples studied without constant external field, with AC field amplitude of 10 Oe and a frequency of 10 kHz. The dispersion part is presented in the left panel and the absorption part is shown in the right panel.

In Graph VI-X the normalized magnetic susceptibility data are presented for all the samples at one selected AC field amplitude and frequency. The dependencies for SPION CChB and CCh are quite similar, but SPION CChB exhibits a larger decrease of magnetic susceptibility at the freezing temperature. The SPION Gd sample shows the highest temperature of the susceptibility maximum of the all SPION samples. The IONP DEX sample has the lowest temperature of the susceptibility maximum of all the materials studied, while for the IONP PEG sample magnetic susceptibility in the measured temperature range does not reach its maximum, which is probably located above 320 K.

Based on the Néel - Arrhenius formula (Eq. V-XI) it is possible to calculate some of the most important parameters used for characterization of superparamagnetic materials. This can be done by transforming the equation Eq. V-XI to frequency domain (Bałanda, 2013). The blocking temperature T_B and τ_N can be calculated from χ vs temperature measured at different frequencies and using equation (Eq. V-XII). It is assumed that T_B is a temperature, at which magnetic susceptibility reaches its maximum. The anisotropy constant K can be then estimated using approximation of nanoparticles size obtained from XRD and STEM measurements. With these parameters it is possible to calculate other parameters, like the fluctuations frequency of nanoparticles at 300 K or the energy barrier $\Delta E = KV$. The blocking

temperature in DC measurements, $T_{B,DC}$ is the temperature, at which the relaxation time of a given collection of nanoparticles equals 100 s, so $T_{B,DC} = KV/25k_B$ (Bałanda, 2013).

Table VI-1 Results of calculations based on the Néel-Arrhenius formula with uncertainties (u()), the anisotropy constant K is calculated for particle diameter obtained from XRD and STEM.

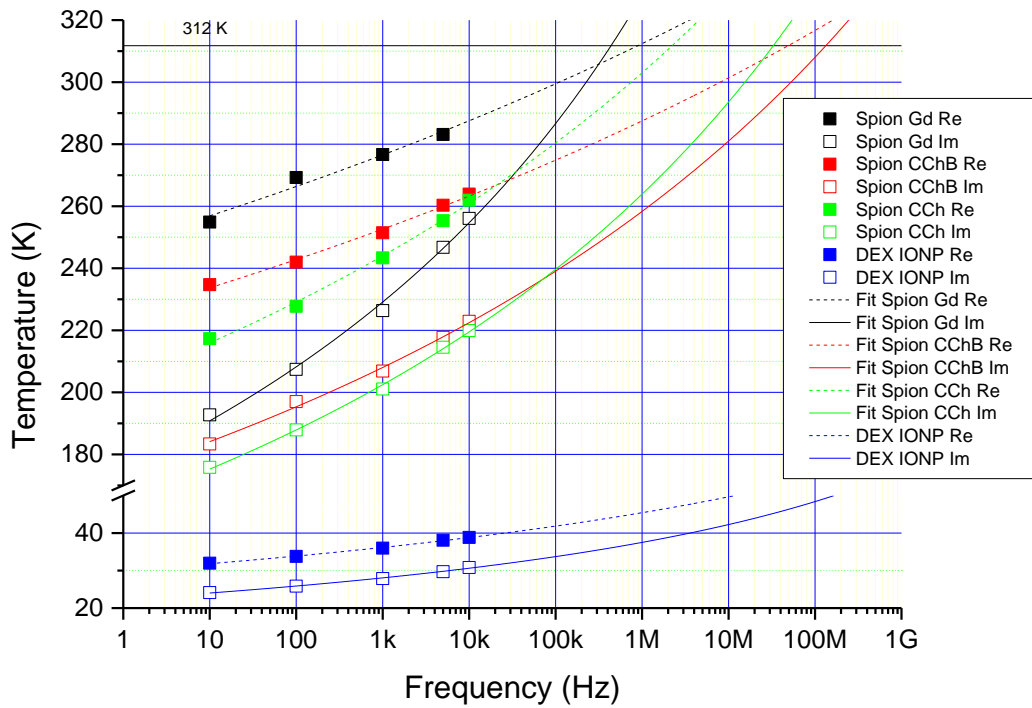
	SPION CCh	u()	SPION CChB	u()	DEX IONP	u()	SPION Gd	u()
$T_{B,DC}$ [K]	240	± 10	295	± 21	31	± 3	210	± 16
KV/k_B [K] x10	600	± 28	738	± 10	77	± 4	526	± 39
τ_0 [s]	$1,2 \times 10^{-16}$		$3,9 \times 10^{-19}$		$1,2 \times 10^{-15}$		$2,2 \times 10^{-13}$	
f_{RT} [MHz]	15	± 34	52	± 60	61×10^6		0.22	± 0.7
D_{xrd} [nm]	9		10		4		11	
K [kJ/m ³], [erg/cm ³] x10 ⁴	37	± 1	43	± 8	60	± 3	39	± 9
D_{stem} [nm]	13		7		8		14	
K [kJ/m ³], [erg/cm ³] x10 ⁴	12.2	± 0.2	127	± 8	18	± 1	19	± 4

Such values of the blocking temperature recalculated to correspond to a static case are in agreement with those obtained in VSM only for the DEX IONP sample, while for other samples they are roughly two times higher. The values of the energy barrier derived are in the range expected for nanoparticles of similar size (Haracz et al., 2015) and are similar for SPIONs, with SPION Gd showing the lowest one and SPION CChB the highest one. The values of the attempt time τ_0 are very short in

comparison with values obtained by other researchers (Bałanda, 2013). The values obtained are about three orders of magnitude longer than or those considered to be valid for ferro or antiferromagnetic material (Kim et al., 2001). The determined values of the fluctuation frequency at room temperature are in MHz range, therefore, spectra obtained from Mössbauer spectroscopy are likely to show a relaxational character (see below). The typical values of the magnetic anisotropy coefficient K for magnetite/maghemite nanoparticles of similar sizes are in the range of several to several hundreds of kJ/m^3 (Coduri et al., 2020; Figueroa et al., 2015; Jonsson et al., 1997), and the values obtained here for SPION and DEX IONP nanoparticles are in this range. All of the above are higher or close to those of bulk Fe_3O_4 (about 11 kJ/m^3) or $\gamma\text{-Fe}_2\text{O}_3$ (13 kJ/m^3) (Martinez-Boubeta et al., 2013). However, depending which method of particle volume assessment is employed, the results can differ significantly.

With the obtained information about temperatures at which maximum of absorption occurs and using Eq. V-XII it is possible to extrapolate the maximum of absorption to higher frequencies than those that could be used in ACMS.

This is especially useful for estimating the potential applicability of nanoparticles for magnetic hyperthermia as the best results in this application would be achieved when the maximum of the absorbance occurs at the human body temperature, to exploit their self-regulating potential. Table VI.II presents the results of extrapolations of fitted lines to the human body temperature (shown in Graph VI-XI).



Graph VI-XI Blocking temperature (maximum of the absorption part of the magnetic susceptibility) of investigated samples as a function of the AC field frequency together with fits to the experimental data.

The DEX IONP sample shows unreasonably high frequency required to achieve a maximum at human body temperature (312 K) which is not surprising as it has very low blocking temperatures. A huge difference between SPION samples is, on the other hand, quite unexpected. Since the required frequency for SPION CCh and CChB is in MHz range, their potential for magnetic hyperthermia would be limited, as the electromagnetic field of sufficient strength might be harmful to living organism. The SPION Gd sample is the most suitable for hyperthermia application of the studied samples.

Table VI-II Estimated frequency at which T_B would be equal to a human body temperature.

	SPION Gd	DEX-ION	SPION CChB	SPION CCh
F_{MAX312} [MHz]	0.4	67×10^6	135	33

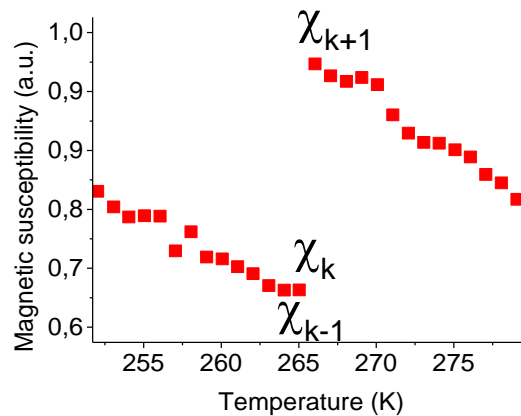
This measurement technique presents also a unique opportunity to study the behavior of nanoparticles in water solution at freezing temperature and through that to separate the influence of the Néel and Brown relaxation process. The Graph VI-XIII presents the partial contributions of these two processes to χ . The relative Brownian contribution was calculated from the following formula:

$$\chi_B = \frac{\chi_{k+1} - \chi_k + \Delta\chi}{\chi_{k+1}} * 100 \quad \text{Eq. VI-V}$$

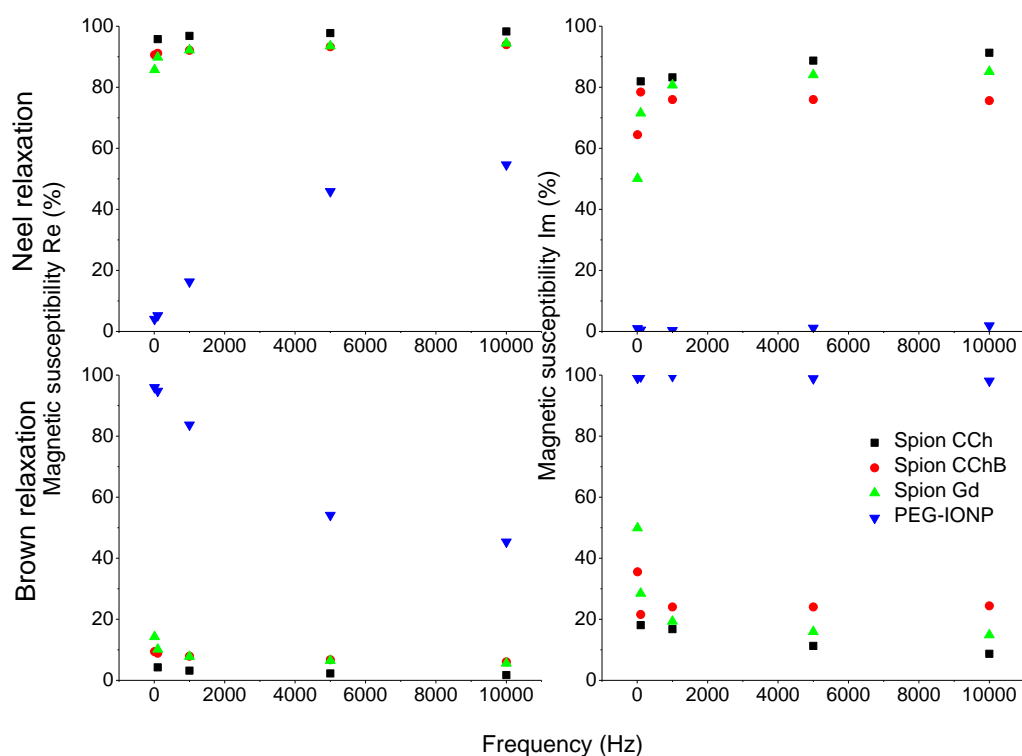
$$\chi_N = 100 - \chi_B \quad \text{Eq. VI-VI}$$

$$\Delta\chi = \chi_k - \chi_{k-1} \quad \text{Eq. VI-VII}$$

where χ_{k+1} is a value of magnetic susceptibility just above the step at freezing temperature and χ_k - just below, as indicated in graph VI-XII.



Graph VI-XII Graphical explanation of the procedure of determination of the Brownian contribution at the freezing temperature (see also Eq. VI-V to Eq. VI-VII).



Graph VI-XIII The partial Néel (top) and Brown (bottom) relaxation contributions to the magnetic susceptibility at the freezing temperature in the dispersion part (left panels) and in the absorption part (right panels).

The SPION samples absorb most of the energy in Néel process with only SPION Gd reaching 50% at low frequencies. Concerning the SPION samples, the hydrodynamic radius does not seem to affect this behavior too much, with the only difference that SPION CChB with the largest radius is not affected by frequency change as strong as the other samples are. The biggest contribution of Brownian relaxation is observed for the PEG IONP sample with almost 100 percent share. This is certainly caused by its high blocking temperature, so that at the freezing temperature there is not much absorption in Néel's mechanism as the particles are in the blocked state. The decrease of the Brownian contribution with increasing frequency might be explained by the viscous torque acting on the particles shells. At frequencies higher than that of their natural diffusion rotation they cannot keep up with the changes of the magnetic field.

3. Summary for magnetic dynamics study

All the samples show similar temperature dependence of magnetic susceptibility. Going from low temperatures it increases, then approaches a maximum for four of the samples studied, and then it starts decreasing. For all the samples studied the ratio between χ' and χ'' is of the order of 10. The temperature of the maximum in the absorption part varies between samples in a wide range of temperatures (from ~30 K to ~260 K and possibly higher for the PEG IONP sample). A step in the temperature dependence of both components of the magnetic susceptibility is observed for all suspension samples, except for the DEX IONP, at temperature close to 260 K, which is attributed to freezing of the suspension and stopping of the Brownian relaxation. A second, weak maximum appears at low temperature (~50 K) for all the samples except the DEX IONP one. The derived values of $T_{B,DC}$ are consistent with temperatures of vanishing of the coercive field obtained from VSM measurements. Therefore, it can be concluded that values of ΔE estimated from ACMS data are reliable.

The values obtained for magnetic anisotropy coefficient K are strongly influenced by the estimation of the particle diameter and, thus, bear a large error margin. Nevertheless, they are within expected range for maghemite nanoparticles of that size. Out of SPION samples, the SPION CChB exhibits the highest energy barrier and the SPION Gd the lowest one. The calculated magnetic fluctuation frequency at room temperature is in a range of megahertz for SPION samples but it bears rather high uncertainty.

From the susceptibility step at the freezing temperature the Brownian contribution is estimated and it is found that it is prevailing for the PEG IONP since it is in a blocked state at this temperature. The SPION samples show much smaller contribution of the Brownian relaxation, which is responsible for about 20% of energy absorption in these samples. The Brownian contribution in SPION CChB is less dependent on the AC field frequency compared with other SPION samples. The extrapolation of the temperature at which magnetic susceptibility (absorption part) attains a maximum, to a

human body temperature indicates that at least SPION Gd could be a prospective material for magnetic hyperthermia, as the frequency required for its optimal heating stays much below the microwave range. Its comparable Neel and Brown parts show that it could be effective when the nanoparticles are suspended in fluid and also when they are immobilized.

VII. Mössbauer spectroscopy studies

Many contemporary research techniques are based on probing nuclei of atoms in the investigated substance and one of them is the Mössbauer spectroscopy. After more than a half the century from its discovery it proved to be very useful tool for research in many fields of science, such as physics, chemistry, geology, metallurgy, biology or even archeology (Cousins and Dharmawardena, 1969; Lempart et al., 2020). As nuclei are influenced by their surroundings, the chemical, structural and magnetic properties (both static and time dependent) of a material can be studied. The method is named after Rudolph Mössbauer who discovered it (Mössbauer, 1958).

1. The principles of Mössbauer spectroscopy

Energy levels of nuclei are influenced by their surrounding environment, both by electric and magnetic field, which can shift or split these levels. Therefore, by observing these shifts the information about electronic or structural properties of the material studied can be obtained. These changes can provide information about the local environment of the parent atoms within a sample and should be possible to observe using resonance-fluorescence. There are, however, two major obstacles in obtaining such an information. First, the “hyperfine” interactions between the nucleus and its electronic environment are extremely small, so that the energy shifts are of the order of 10^{-7} eV. The second, the recoil of the nucleus, as the gamma-ray is emitted or absorbed, prevents matching to the resonance. In order to obtain the resonance, the absorbed photon must have the energy profile overlapping with the energy profile of an emitted photon. According to the energy conservation principle both the absorber and the source nuclei experience a recoil, so the actual energy of emitted/absorbed photon is shifted by the Doppler effect. In the case of ^{57}Fe nuclei the energy of the emitted photon is 14.4 keV and with a mass of ~ 57 Da the recoil energy would be 0.0004 eV. This is much larger than the natural line width of $4,7 \times 10^{-9}$ eV, which comes from the Heisenberg uncertainty principle and the lifetime of an excited state

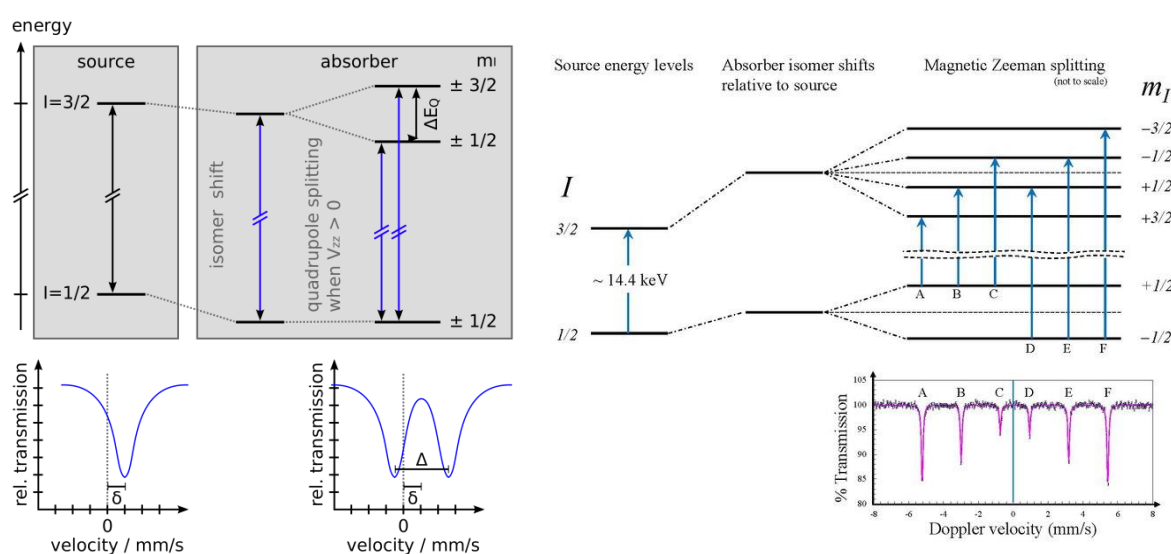
(140 ns for ^{57}Fe 3/2- \rightarrow 1/2 transition). As it comes out, the recoil for an atom embedded in a crystal lattice is far smaller than it is expected for an isolated atom as the momentum is absorbed by the whole crystal so the mass of an absorber is effectively many orders of magnitude larger. This phenomenon is called the Mössbauer effect.

The need for a resonant fluorescence limits the amount of isotopes that could be used with this technique to those that have transitions with excited state lifetime in the range of 10^{-6} s to 10^{-11} s and transition energy in the range of 5 keV to 180 keV. A shorter or longer lifetime would result in too narrow energy profiles for the resonance to occur or too broad for the observation of changes in the spectra obtained. There are more than 40 isotopes that fulfill such conditions, e.g. ^{57}Fe , ^{61}Ni , ^{119}Sn or ^{197}Au and among them ^{57}Fe is the most popular in Mössbauer spectroscopy.

In a free nucleus the ground state is degenerated and there is only one absorption line present in the spectrum. The energy levels can be split or changed when nuclei are subjected to electric or magnetic field, as mentioned. The interactions between nucleus and its surrounding are termed hyperfine interactions. Electrons of *s* orbitals have a nonzero probability of charge density in the volume of a nucleus. If the electric field within the nucleus is homogenous, all energy levels would be shifted by the same energy and the effect is called the isomer shift and is denoted as δ or *IS*. The isomer shift can give information about the atom's oxidation state or the type of bond and, in this way, it is similar to the chemical shift known from other types of spectroscopic techniques.

When the electric field at the nuclei is not homogenous, the nuclear quadrupole moment interacts with the electric field gradient (EFG) and the energy levels are split. They are schematically represented on Graph VII-I. In this situation there are two possible transitions with energy difference of ΔE_Q . This type of interaction is called the electric quadrupole interaction and allows to determine the quadrupole splitting denoted as Δ or *QS*. The quadrupole splitting carries the information about the oxidation state and the symmetry of atomic surrounding.

The last type of the hyperfine interactions is the magnetic dipolar interaction. This takes place when there is a magnetic field present in the volume of nucleus and the nucleus has its own magnetic moment which occurs for $I \geq 1/2$ and it also splits the energy levels, in this case to $2I+1$ levels. For ^{57}Fe there are six possible transitions fulfilling the dipolar selection rules i.e. $\Delta I = \pm 1$ and $\Delta m_I = 0, \pm 1$. The effective magnetic field induction at the nucleus, B_{eff} often called the hyperfine field HFF is a sum of the Fermi contact field, orbital dipolar contribution, spin dipolar contribution and the applied external magnetic field.



Graph VII-I Schematic representations of: isomer shift, δ and quadrupole splitting, Δ in the left panel and the magnetic Zeeman splitting in the right panel for the ^{57}Fe Mössbauer source: https://upload.wikimedia.org/wikipedia/commons/thumb/6/66/Mössbauer_Isomer_Shift_and_Quadrupole_Splitting_for_57Fe.svg/2000px-Mössbauer_Isomer_Shift_and_Quadrupole_Splitting_for_57Fe.svg.png

In the case of a thin absorber when only natural line width contributes to the spectral lines shape, it was proven that the lines have the shape of a Lorentzian function. Solution of Hamiltonian for a system with $I=3/2$ to $I=1/2$ transition, with electric field gradient and magnetic interaction yields six absorption energies as described by the following expressions:

$$\begin{aligned}
\Delta E_1 &= \left(\frac{3}{2} g_L - \frac{1}{2} g'_L \right) \mu_N B + \delta - \Delta \\
\Delta E_2 &= \left(\frac{1}{2} g_L - \frac{1}{2} g'_L \right) \mu_N B + \delta + \Delta \\
\Delta E_3 &= \left(-\frac{1}{2} g_L - \frac{1}{2} g'_L \right) \mu_N B + \delta + \Delta \\
\Delta E_4 &= \left(+\frac{1}{2} g_L + \frac{1}{2} g'_L \right) \mu_N B + \delta + \Delta \\
\Delta E_5 &= \left(-\frac{1}{2} g_L + \frac{1}{2} g'_L \right) \mu_N B + \delta + \Delta \\
\Delta E_6 &= \left(-\frac{3}{2} g_L + \frac{1}{2} g'_L \right) \mu_N B + \delta - \Delta
\end{aligned}$$

Eq. VII-I

where g_L and g'_L are Lande atomic factors of the ground and excited state, μ_N is the nuclear magneton.

The line positions are related to the differences of the respective energy levels of the split states, but the line intensities are related to the angle between the Mössbauer gamma-ray and the direction of the magnetic field at nucleus, which is usually parallel or antiparallel to the magnetic moment of the atom. The outer, middle and inner line intensities are related by:

$$3 : \frac{4 \sin 2\theta}{1 + \cos 2\theta} : 1$$

Eq. VII-II

where θ is the angle between incident gamma ray and the magnetic moment.

The outer and inner lines are always in the same proportion, but the middle lines can vary in relative intensity between 0 and 4 depending on the angle between the nuclear spin moments and the gamma-rays. In polycrystalline samples with no applied field this value averages to 2 (as in Graph VII-I lower right panel), but in single crystals or under applied fields the relative line intensities can provide information about moment orientation and magnetic ordering.

The Lorentzian shape of a line occurs only in an ideal situation where the absorber is thin enough that there is no self-absorption and other factors like Debye–

Waller factor (thermal oscillations of atoms in a crystal) are negligible. In such a situation every component of a spectrum can be treated individually and the outcome is algebraic sum of the components. Rancourt et al. presented a formula for calculating an ideal absorber thickness $t_{g,ideal}$, i.e. the thickness of the absorber yielding maximal signal to noise ratio, and a technique for assessing influence of thickness on the relative spectral lines area (Rancourt et al., 1993). The formula states that:

$$t_{g,ideal} = \frac{1}{\mu_e}$$

$$\mu_e = \sum_i \beta_i \mu_{e,i}$$

Eq. VII-III

$$n_{a,thin} = \frac{t_a f_a \sigma_0}{\alpha}$$

where μ_e - electronic mass absorption coefficient of the absorber material for the Mössbauer γ -ray, β_i is the mass fractions of the element i , t_a is dimensionless absorber thickness, f_a is a recoilless fraction for absorbing nucleus, σ_0 is the Mössbauer cross section at resonance; α is a fraction of the spectrum area of the strongest component and n_a is the absorber thickness expressed as the number of Mössbauer nuclei.

Calculations for magnetite reveal that ideal thickness of the absorber should be of order of 23 mg/cm² but processing of this data would require usage of transmission integral for reliable outcome. For area distortion less than 5% (the thin absorber approximation) the thickness should be less than 2 mg/cm².

The energy differences between nuclear energy levels are extremely small (in order of 10⁻⁸ eV). To obtain energy resolution in this range the Doppler effect is employed. The typical Mössbauer spectrometer is composed of a suitable gamma radiation source (for ⁵⁷Fe it is ⁵⁷Co) mounted at an oscillating drive. Changes in source velocity v with respect to the absorber influence the source γ -ray energy E_0 according to Doppler formula:

$$E' = E_0 \left(1 + \frac{v}{c}\right)$$

$$\Delta E = \frac{E_0 v}{c}$$

Eq. VII-IV

Where c is the speed of light in vacuum and E' is the Doppler shifted energy. The energy absorption levels in Mössbauer spectroscopy are usually expressed in velocity units for convenience.

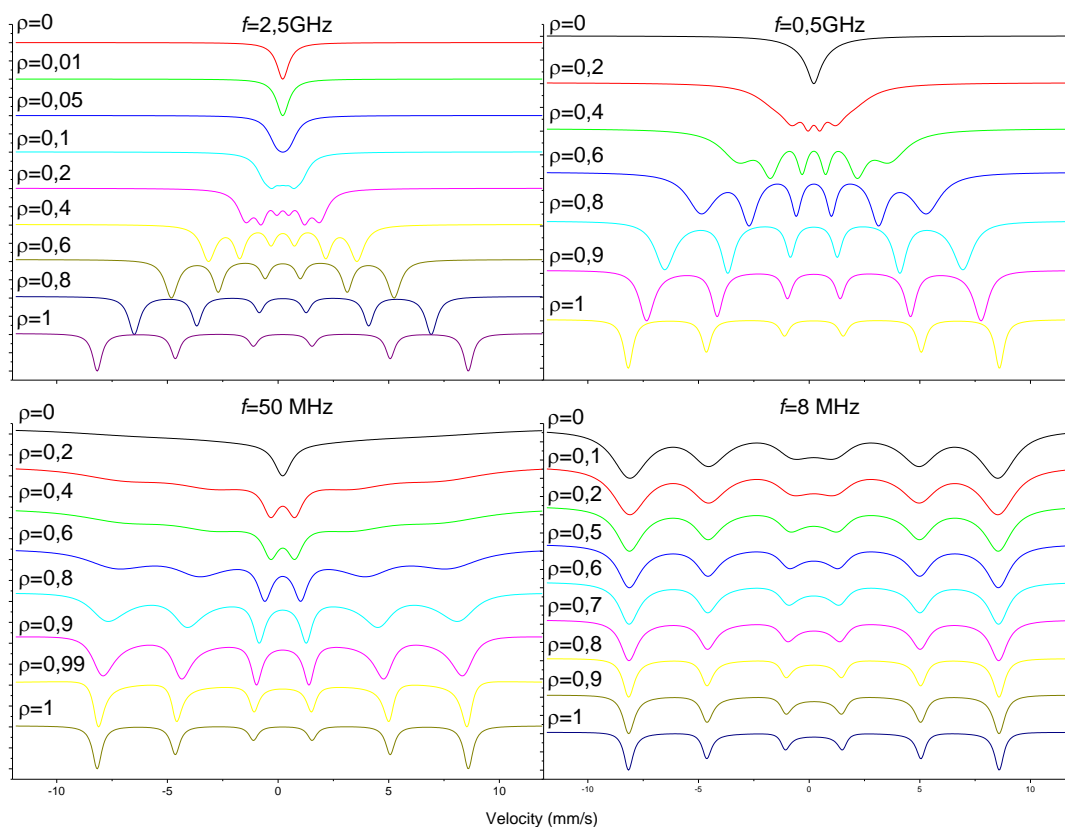
A situation in which there is only one component in the spectrum is quite rare in practice and Mössbauer spectroscopy is often utilized for determination of phases present in a sample on the basis of their specific lines in the spectra. When measuring a set of particles with nanometer size, there are additional effects that influence the shape of spectra. One of them is the size distribution of nanoparticles in the sample studied. If nanoparticles possess spontaneous magnetic moments, the spectra can exhibit a hyperfine field distribution corresponding to the particle size distribution. When the nanoparticles are small enough to be superparamagnetic at given measurement conditions the resulting spectra can be more complex. This topic is quite well described in literature, namely Blume and Tjon elaborated a method for calculating the spectra in such fluctuating environment (Blume and Tjon, 1968). It was based on the previous work of Anderson, Weiss and Kubo concerning similar problem in nuclear magnetic resonance. This stochastic method introduces a fluctuating magnetic field by replacing the expression for magnetic field energy in the Hamiltonian of the system with a random function that assumes one of two states -1 or +1. In order to give this random function some physical meaning it is specified with matrix of probabilities of transitions between states in a time period which corresponds to a fluctuation frequency f and asymmetry of residing time ρ in each state. Those two factors determine the shape of the spectra.

There are four scenarios worth mentioning. When the frequency of fluctuations is much lower than the reciprocal of the characteristic time of the Mössbauer transition (~ 7 MHz for ^{57}Fe) then the spectra should remain unaffected, no matter what the

asymmetry is. On the opposite side is the case when the fluctuation frequency is high and there is no asymmetry, then the sextet in the spectrum would collapse into a single line, as the hyperfine field seen by the nucleus would average to zero over the time of the Mössbauer transition. In-between of those two extremes there is the case when both frequency and asymmetry are moderate, then the shape of the spectra would be a distorted sextet with broadened most outer pair of lines and whole spectrum shrunk, as the hyperfine field averaged over the transition time diminishes. The last case is when the frequency is high and the asymmetry is also substantial, then there is no significant distortion in the spectrum but the average (effective) hyperfine field B_{eff} is smaller than hyperfine field in one of the states, B_0 . The effective field can then be calculated as:

$$B_{eff} = B_0 \frac{\rho}{f} = B_0 \sigma \quad \text{Eq. VII-V}$$

It is convenient to introduce the asymmetry normalized to the fluctuation frequency $\sigma = \rho/f$ as then $\sigma=0$ would correspond to a fully symmetrical and $\sigma=1$ – to a static, fully asymmetric case. In Graph VII-II examples of line shapes are presented, corresponding with different frequencies f and residing times ρ calculated using the previously described method.



Graph VII-II Simulated line shapes for $B=540$ kOe, $IS = 0.24$ mm/s and $QS = 0$.

When the fluctuation frequency is only slightly higher than the measurement frequency the most apparent effect in the spectra is broadening of the peaks and distortion of their intensity ratio. With increasing frequency the effects of relaxational character are more pronounced. When the asymmetry factor ρ is close to unity, the only effect is a change in the hyperfine field, especially strong at high frequencies. For ρ close to zero the spectra collapse into a single peak. In the intermediate states the spectra have their line shapes diverging from the Lorentzian shape and the outer lines are the most strongly broadened towards the center of the spectrum.

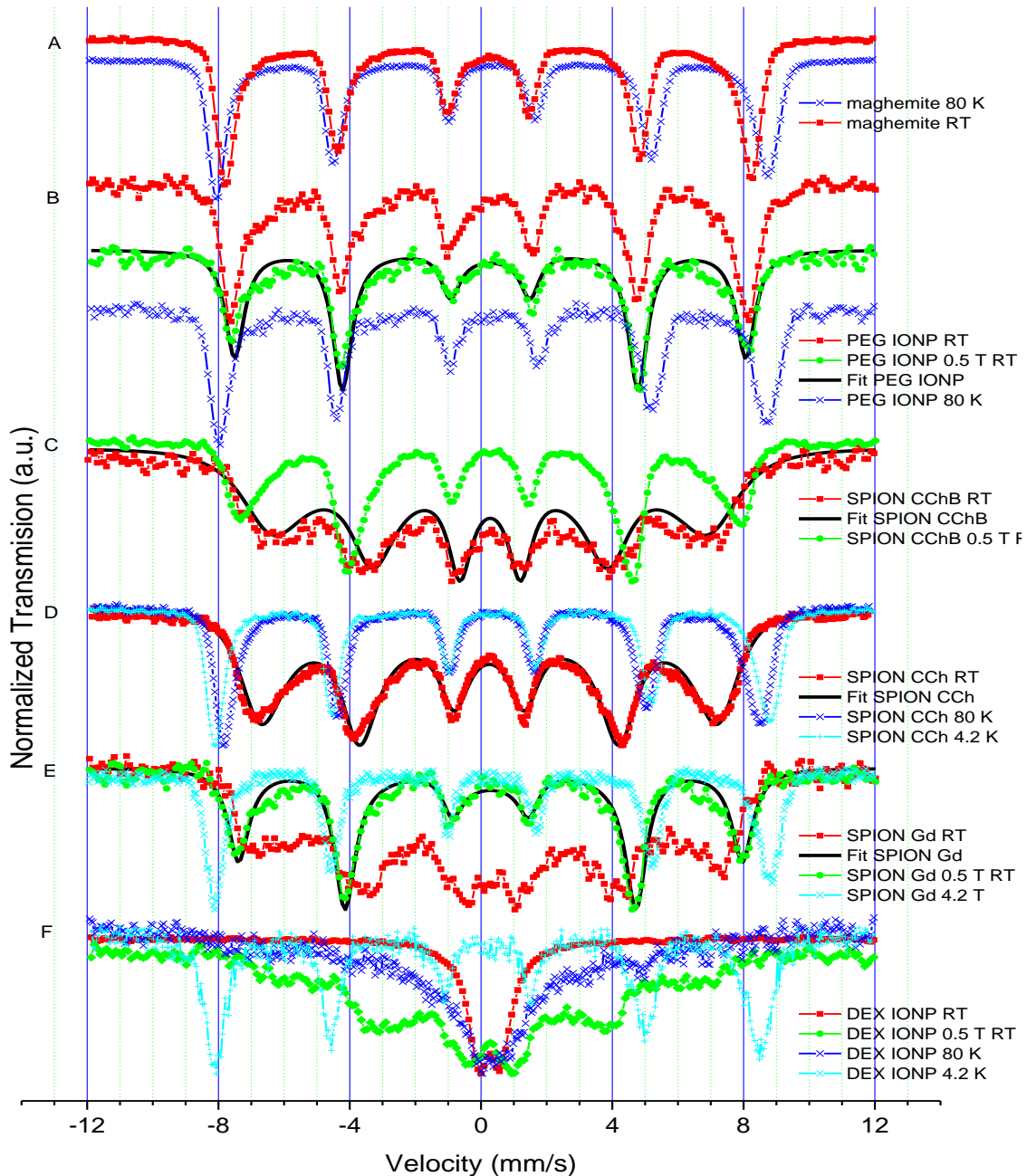
1. Experimental

Mössbauer effect has rather low sensitivity, thus it requires high concentration of Mössbauer active element in the sample studied. Because of this, samples of nanoparticles couldn't be used in their original, water suspension, state but had to be dried. The same samples that were used for XRD were measured at room temperature and at applied external magnetic field. For measurements at low temperatures samples were dried on a high purity aluminum foil and pressed against another foil to form a thin capsule. External magnetic field was produced with a set of permanent neodymium magnets. Magnetic field in the sample region was measured with a magnetic field meter based on Hall effect. Mössbauer measurements have been carried out in the transmission mode at a constant acceleration spectrometer. A source of 50 mCi ^{57}Co in rhodium matrix has been used. For low temperature measurements a bath cryostat filled with liquid nitrogen or helium or continuous flow cryostat were used. For temperature stabilization an automated temperature controller was used.

The spectra obtained were fitted using a Gauss-Newton's iterative method of minimizing χ^2 , with a Lorentz function shape of the spectral lines for the low temperature static spectra. For room temperature results the fitting proposed by Blume and Tjon was applied to obtain relaxation parameters f (fluctuation frequency) and ρ/f (asymmetry as defined by D. G. Rancour) (Blume and Tjon, 1968; Rancourt, 1996).

2. Results and discussion

The spectra obtained for the samples studied are presented in Graph VII-III. As their individual magnitudes (the effect) significantly differ due to different Fe content related to varying nanoparticle shell thickness, the spectra are shown with their intensity normalized to unity.



Graph VII-III Cumulative graph of normalized Mössbauer spectra for all the investigated materials at different temperatures, with and without external magnetic field. For selected spectra curves fitted according to the presented model are also shown. The velocity is relative to Co(Rh) for all spectra.

A simple explanation presented in theory section states that Mössbauer spectra should consist of Lorentzian peaks and this is correct in the case of simple systems. The spectra of PEG-IONP (Graph VII-III B) almost agree with this picture with six absorption peaks visible and their areas corresponding to the case of isotropic distribution of magnetic moments in the sample. When external magnetic field of 0.5 T was applied (Graph VII-III green spectra) the middle pair of peaks gained on intensity relatively to other peaks, which reflects an anisotropic distribution of magnetic moments in the sample as they align with external magnetic field.

Mössbauer spectra of all SPION samples measured at room temperature (Graph VII-III) look quite similar. There is strong deviation of line shape from Lorentzian distribution visible, which is due to relaxation of magnetic moments of nanoparticles, as described in the literature. The outer lines are flattened and whole spectrum is smeared towards its center. With the applied magnetic field the SPION Gd spectrum is brought to the state in which it resembles PEG IONP measured with external field, although with broader lines. The spectra of the DEX IONP sample are the most different compared to other samples (Graph VII-III F). At room temperature there is only central doublet visible and the whole spectrum is compressed towards its center. In addition, splitting between those two peaks is clearly much smaller compared to the central pair of lines in other samples. That suggests very high fluctuations frequency which is consistent with its low blocking temperature. Even applying external magnetic field of 0.5 T (5 kOe), which, according to VSM measurement, is almost saturation field, isn't able to bring this sample to the static state. In all the low temperature spectra there is a noticeable asymmetry between the outer peaks. The left side peak is narrower and of larger amplitude and the right side one is broader and of smaller amplitude. This is caused by the difference in isomer shifts and hyperfine fields of iron at the tetrahedral and octahedral sites, which for maghemite amount to 0.40 mm/s, 50,6 T and 0.46 mm/s, 52.5 T, respectively, as it is derived from fits of the spectra in the subsequent paragraph.

In the case of SPION CCh at low temperatures the spectra (Graph VII-III D) show that the line broadening toward the center diminishes much. Also the splitting

considerably grows with decreasing temperature, indicating an increase of the hyperfine field, as expected. The spectrum of the SPION Gd sample measured at 4.2 K is similar to SPION CCh. All the three SPION samples show a similar, heavily broadened pattern of room temperature spectra, with the smallest broadening occurring for the SPION CCh material, which indicates its lowest superparamagnetic fluctuations frequency.

To use Mössbauer data to full of its capacity it is needed to use more advanced analysis. With the use of software, based on theory described earlier in this work, sextets were fitted to the experimental data. In the case of room temperature measurements relaxational model was used and for low temperature data standard sextets were fitted with two data sets representing tetrahedral and octahedral sites in maghemite or magnetite.

Table VII-I. Hyperfine parameters for nanoparticle materials studied and microcrystalline maghemite obtained from the fit to the low temperature (4.2 K and 80 K) of Mössbauer spectra.

	Relative Intensity [%]	IS [mm/s]	B [T]	QS [mm/s]
SPION CCh 4,2 K	61(1)	0,48(1)	52,3(3)	0,02(1)
	39(1)	0,41(1)	50,3(4)	-0,01(1)
SPION CCh 80 K	68(1)	0,45(1)	50.9(2)	-0,02(1)
	32(1)	0,39(1)	48,4(5)	-0,02(1)
SPION Gd 4,2 K	64(2)	0,45(1)	52,3(4)	0,01(1)
	36(2)	0,40(1)	50,3(7)	-0,01(1)
PEG IONP 80 K	58(3)	0,52(1)	52.3(7)	-0,02(1)
	42(3)	0,46(1)	50.2(9)	-0,02(1)
DEX IONP 4,3 K	46(4)	0.34(1)	52.2(1)	-0.01(1)
	53(4)	0.29(1)	50.3(3)	-0.01(1)
Maghemite 80 K	61(1)	0.46(1)	52.5(3)	-0.01(1)
	39(1)	0.40(1)	50.6(5)	-0.02(7)

The values of hyperfine parameters obtained by fitting of the spectra measured at 80 K and at 4.2 K with two sextets are presented in Table VII-I. Data obtained for samples measured at 4.2 K are close to these determined for the reference maghemite

structure. Values of the relative intensity of the tetra- and octahedral components, IS, B_{hf} and QS mostly match to those of maghemite within the uncertainty margin for SPION and PEG IONP samples. The DEX IONP sample shows considerable deviation from the maghemite spectrum, with smaller isomer shift and the proportion between two components leading to conclusion that more of octahedral sites are occupied. This can possibly be the explanation of their much different relaxational behavior, as the difference in size between DEX IONP and SPION samples isn't that large according to the XRD or TEM data, The much different site occupation may affect the magnetocrystalline anisotropy, which also has an exponential impact on the superparamagnetic fluctuations frequency (Eq. V-XI).

Table VII-II Hyperfine parameters obtained from the fits of Mössbauer spectra of nanoparticle materials measured at room temperature.

	IS *[mm/s]	B [T]	FWHM [mm/s]	f [MHz]	ρ/f	χ^2
PEG IONP RT	0,38(2)	48,3(1)	0,35	1,2(7)	0,44(4)	0,65
PEG IONP RT 0,5T	0,39(1)	48,3	0,35	1,2(4)	0,98(8)	1,17
DEX IONP RT	0,38	51,6	0,25	10 ⁶	0,07(2)	5,26
DEX IONP RT 0,5T	0,42(2)	50,2	0,30	56(3)	0,44(1)	1,33
SPION CCh RT	0,36(1)	46,2(2)	0,54(1)	106(3)	0,91(2)	2,19
SPION Gd RT	0,39(2)	44,5(4)	0,78(4)	43(4)	0,88(5)	0,62
SPION Gd RT 0,5T	0,4	47,7	0,32	3,8(5)	0,82(4)	1,19
SPION CChB RT	0,39(1)	46(6)	0,35	72(6)	0,78(1)	1,33
SPION CChB RT 0,5 T	0,39(1)	46,5(7)	0,35	4,5(4)	0,8	6,72

* relative to α -Fe

Hyperfine parameters obtained by fitting the spectra measured at room temperature to a single (average) relaxational sextet are presented in Table VII-II. Fitting with two sextets did not provide reliable results and, thus, it was abandoned. The values of the isomer shift (IS) obtained are similar for all the samples (0.38 to 0.39 mm/s). Assuming small or vanishing quadruple splitting (QS), such average IS value could be attributed to Fe³⁺ in maghemite at both the octahedral and the tetrahedral sites. Taking into account large half width of the fitted spectra (0.35 mm/s and higher) one cannot exclude that some part of Fe atoms are of Fe^{2.5+} valence (Dyar et al., 2006), like at the octahedral site in magnetite, where fast electron hopping between

adjacent sites averages Fe^{2+} and Fe^{3+} states to an intermediate one within the time window of the Mössbauer transition.

The superparamagnetic fluctuation frequency obtained varies between samples and for PEG IONP it equals 1.2 MHz, and is smaller than the Mössbauer probing frequency ($1/140 \text{ ns} \approx 7 \text{ MHz}$). This result is consistent with the highest blocking temperature (above 320 K) obtained for these nanoparticles from ACMS measurements discussed in the previous chapter. Application of the magnetic field increases the asymmetry parameter, ρ/f , almost to the static case, $\rho/f=0.98$. In fact, the fitted nonzero frequency value of 1.2 MHz bears a large error margin and can originate from line broadening due to defects rather, than from superparamagnetic fluctuations.

For SPION samples f values are much higher and consistent with their $T_b \sim 280$ K. The unmodified SPION CCh shows the highest f (106 MHz) and modification with gadolinium (SPION Gd) or increased shell thickness (SPION CChB) slow the fluctuations down to 43 MHz and 72 MHz, respectively. Application of the external magnetic field slows down the fluctuations even more (to about 4 MHz for both modified samples) as it was expected, because 0.5 T magnetic field induction is far above the saturation value for this material. This explains a high effectiveness of SPION Gd as low field MRI T_1 contrast agent (Szpak 2014), since there its fluctuation frequency should match the operation (Larmor) frequency. DEX IONP at room sample shows very high f of order of THz as expected. When subjected to the external field, the fluctuation rate diminishes to 57 MHz and the asymmetry factor increases to 0.44.

A high value of the line width observed for SPION samples at room temperature can be attributed to the effect of size distribution of nanoparticle cores. The change of resulting linewidth FWHM upon application of the magnetic field is caused by additional energy introduced to the system. For smaller nanoparticles it can dominate over the magnetocrystalline anisotropy energy, which decreases with decreasing nanoparticle size (Figueroa et al., 2015; Komorida et al., 2009), thus making frequency distribution more uniform. The measured hyperfine field induction was in the range from 44 T to 48 T, being slightly smaller than the average value reported for maghemite (50 T) (Murad and Johnston, J.H., 1989). That can be

explained considering that fluctuations decrease the hyperfine field measured and their frequency spread is actually observed, as can be anticipated from the core size distribution, Graph IV-VII. The observed asymmetry of the magnetic moment distribution in SPION samples could be explained by the existence of larger nanoparticles that are still at the blocked state. This also implies that there can occur some interactions between them.

3. Summary of Mössbauer study

The Mössbauer spectroscopy results confirm that for all SPION samples and PEG IONP sample their cores are composed mostly of maghemite, as the fitted hyperfine parameters are in good agreement with the reference maghemite sample. The DEX IONP sample differs from maghemite in the isomer shift and the component ratio, suggesting that most of the iron atoms are located at octahedral sites, likely due to the highest surface to volume ratio as this sample has the smallest particles. Except for the PEG IONP sample, all the others exhibit distinct signatures of magnetic fluctuations. The fluctuation frequency determined at room temperature was the greatest for DEX IONP as expected, locating at terahertz range

The room temperature fluctuations of the SPION samples were significantly slower, in megahertz range, and there was a considerable asymmetry of the residence time, in contrast to DEX IONP, where the asymmetry was the lowest. This might be possibly caused by a higher magnetocrystalline anisotropy of SPION nanoparticles which can be deduced from their much higher blocking temperatures despite similar sizes to that of DEX IONP. The MHz range of the fluctuation frequencies determined for SPION samples corresponds well to the values obtained from extrapolated ACMS measurements results. However, there are discrepancies ranging up to one order of magnitude (and even more for SPION Gd), which could be related to a lack of the Brown relaxation in dried samples used for Mössbauer spectroscopy measurements. Addition of gadolinium complex to the shell of nanoparticle doesn't appear to have a significant impact on the hyperfine parameters in the static state but apparently slows down the fluctuations. Similar, but smaller slowing effect was observed for nanoparticles with thicker shell.

VIII. Conclusions

The study conducted allows to formulate the following conclusions:

- Nanoparticles studied are mostly composed of maghemite as determined by XRD and Mössbauer study. However, the magnetic behavior of the PEG-IONP sample indicates that there may be another phase, producing exchange bias effect, present in this material.
- Relaxation frequencies determined from Mössbauer spectroscopy are comparable with those obtained from the ACMS, with exception of Spion Gd, indicating that, although Brown relaxation influences the value of the magnetic susceptibility it doesn't have a major impact on the blocking temperature.
- Addition of gadolinium complex to the shell of nanoparticle slows down the superparamagnetic fluctuations rate and adds paramagnetic component to the magnetization curve at low temperatures.
- Different coatings result in a major difference in the Brown relaxation. It was found that the thin coating (PEG) results in a prevailing Brown-like contribution, whereas for the thicker chitosan coated materials both parts are comparable.
- The thickness of the shell does not influence the ratio between Brown and Néel relaxation at low frequencies but nanoparticles with thick shell reach equilibrium at higher frequencies, whereas for other samples this ratio is still changing at 10 kHz.
- The shell thickness does influence the blocking temperature and the behavior in liquid (viscous) environment.
- The environment strongly influences the properties of the nanoparticles so for any practical application the study of such materials should be conducted in the environment they are intended to be used.

- The characteristic frequencies of superparamagnetic fluctuations observed show that the maximum absorption of the electromagnetic radiation corresponds to the range from hundreds of kilohertz to hundreds of megahertz, i.e. they can be regarded as suitable for self-regulating magnetic hyperthermia. In particular, the chitosan coated SPIONs can be considered as good candidates for hyperthermia of immobilized nanoparticles, whereas for the PEG-IONP that effect is obtained mainly due to freely rotating nanoparticles.
- The SPION materials can also be effective as contrast agents for MRI, in particular, for T_1 weighted scans at low field scanners, as their characteristic fluctuation frequencies correspond to operation (Larmor) frequencies there.

IX. References

- Alwi, R., Telenkov, S., Mandelis, A., Leshuk, T., Gu, F., Oladepo, S., Michaelian, K., 2012. Silica-coated super paramagnetic iron oxide nanoparticles (SPION) as biocompatible contrast agent in biomedical photoacoustics. *Biomed. Opt. Express* 3, 2500. <https://doi.org/10.1364/BOE.3.002500>
- Ansari, M.O., Parveen, N., Ahmad, M.F., Wani, A.L., Afrin, S., Rahman, Y., Jameel, S., Khan, Y.A., Siddique, H.R., Tabish, M., Shadab, G.G.H.A., 2019. Evaluation of DNA interaction, genotoxicity and oxidative stress induced by iron oxide nanoparticles both in vitro and in vivo: attenuation by thymoquinone. *Sci Rep* 9, 6912. <https://doi.org/10.1038/s41598-019-43188-5>
- Anthony, J.W., Bladh, K.W., Bideaux, R.A., 1990. Magnetite. *Handbook of Mineralogy*. Chantilly, VA: Mineralogical Society of America 333.
- Aragón, R., Buttrey, D.J., Shepherd, J.P., Honig, J.M., 1985. Influence of nonstoichiometry on the Verwey transition. *Phys. Rev. B* 31, 430–436. <https://doi.org/10.1103/PhysRevB.31.430>
- Arruebo, M., Fernández-Pacheco, R., Ibarra, M.R., Santamaría, J., 2007. Magnetic nanoparticles for drug delivery. *Nano Today* 2, 22–32. [https://doi.org/10.1016/S1748-0132\(07\)70084-1](https://doi.org/10.1016/S1748-0132(07)70084-1)
- Baker, I., Zeng, Q., Li, W., Sullivan, C.R., 2006. Heat deposition in iron oxide and iron nanoparticles for localized hyperthermia. *Journal of Applied Physics* 99, 08H106. <https://doi.org/10.1063/1.2171960>
- Bałańda, M., 2013. AC Susceptibility Studies of Phase Transitions and Magnetic Relaxation: Conventional, Molecular and Low-Dimensional Magnets. *Acta Phys. Pol. A* 124, 964–976. <https://doi.org/10.12693/APhysPolA.124.964>
- Banin, A., Ben-Shlomo, T., Margulies, L., Blake, D.F., Mancinelli, R.L., Gehring, A.U., 1993. The nanophase iron mineral(s) in Mars soil. *J. Geophys. Res.* 98, 20831. <https://doi.org/10.1029/93JE02500>
- Baruah, S., Najam Khan, M., Dutta, J., 2016. Perspectives and applications of nanotechnology in water treatment. *Environ Chem Lett* 14, 1–14. <https://doi.org/10.1007/s10311-015-0542-2>
- Beyene, H.D., Werkneh, A.A., Bezabh, H.K., Ambaye, T.G., 2017. Synthesis paradigm and applications of silver nanoparticles (AgNPs), a review. *Sustainable Materials and Technologies* 13, 18–23. <https://doi.org/10.1016/j.susmat.2017.08.001>
- Bloemen, M., Brullot, W., Luong, T.T., Geukens, N., Gils, A., Verbiest, T., 2012. Improved functionalization of oleic acid-coated iron oxide nanoparticles for biomedical applications. *J Nanopart Res* 14, 1100. <https://doi.org/10.1007/s11051-012-1100-5>
- Blume, M., Tjon, J.A., 1968. Mössbauer Spectra in a Fluctuating Environment. *Phys. Rev.* 165, 446–456. <https://doi.org/10.1103/PhysRev.165.446>
- Brown, R., 1828. XXVII. *A brief account of microscopical observations made in the months of June, July and August 1827, on the particles contained in the pollen of plants; and on the general existence of active molecules in organic and*

- inorganic bodies*. The Philosophical Magazine 4, 161–173. <https://doi.org/10.1080/14786442808674769>
- Brown, W.F., 1963. Thermal Fluctuations of a Single-Domain Particle. Phys. Rev. 130, 1677–1686. <https://doi.org/10.1103/PhysRev.130.1677>
- Bulwan, M., Zapotoczny, S., Nowakowska, M., 2009. Robust “one-component” chitosan-based ultrathin films fabricated using layer-by-layer technique. Soft Matter 5, 4726. <https://doi.org/10.1039/b909355a>
- Buzea, C., Pacheco, I.I., Robbie, K., 2007. Nanomaterials and nanoparticles: Sources and toxicity. Biointerphases 2, MR17–MR71. <https://doi.org/10.1116/1.2815690>
- Bystrzejewska-Piotrowska, G., Golimowski, J., Urban, P.L., 2009. Nanoparticles: Their potential toxicity, waste and environmental management. Waste Management 29, 2587–2595. <https://doi.org/10.1016/j.wasman.2009.04.001>
- Caricato, A.P., Luches, A., Martino, M., 2016. Laser Fabrication of Nanoparticles, in: Aliofkhaezai, M. (Ed.), Handbook of Nanoparticles. Springer International Publishing, Cham, pp. 407–428. https://doi.org/10.1007/978-3-319-15338-4_21
- Chaudhuri, A., Mandal, K., 2012. Enhancement of ferromagnetic and dielectric properties of lanthanum doped bismuth ferrite nanostructures. Materials Research Bulletin 47, 1057–1061. <https://doi.org/10.1016/j.materresbull.2011.12.034>
- Chen, A., Holt-Hindle, P., 2010. Platinum-Based Nanostructured Materials: Synthesis, Properties, and Applications. Chem. Rev. 110, 3767–3804. <https://doi.org/10.1021/cr9003902>
- Chinnathambi, S., Shirahata, N., 2019. Recent advances on fluorescent biomarkers of near-infrared quantum dots for *in vitro* and *in vivo* imaging. Science and Technology of Advanced Materials 20, 337–355. <https://doi.org/10.1080/14686996.2019.1590731>
- Chiolerio, A., Garofalo, E., Mattiussi, F., Crepaldi, M., Fortunato, G., Iovieno, M., 2020. Waste heat to power conversion by means of thermomagnetic hydrodynamic energy harvester. Applied Energy 277, 115591. <https://doi.org/10.1016/j.apenergy.2020.115591>
- Coduri, M., Masala, P., Del Bianco, L., Spizzo, F., Ceresoli, D., Castellano, C., Cappelli, S., Oliva, C., Checchia, S., Allietta, M., Szabo, D.-V., Schlabach, S., Hagelstein, M., Ferrero, C., Scavini, M., 2020. Local Structure and Magnetism of Fe₂O₃ Maghemite Nanocrystals: The Role of Crystal Dimension. Nanomaterials 10, 867. <https://doi.org/10.3390/nano10050867>
- Cole, A.J., David, A.E., Wang, J., Galbán, C.J., Hill, H.L., Yang, V.C., 2011. Polyethylene glycol modified, cross-linked starch-coated iron oxide nanoparticles for enhanced magnetic tumor targeting. Biomaterials 32, 2183–2193. <https://doi.org/10.1016/j.biomaterials.2010.11.040>
- Cousins, D., Dharmawardena, K., 1969. Use of Mössbauer spectroscopy in the study of ancient pottery. Nature 223, 732–733. <https://doi.org/10.1038/223732a0>
- Cullity, B.D., Graham, C.D., 2011. Introduction to magnetic materials. John Wiley & Sons.
- Dhand, C., Dwivedi, N., Loh, X.J., Jie Ying, A.N., Verma, N.K., Beuerman, R.W., Lakshminarayanan, R., Ramakrishna, S., 2015. Methods and strategies for the

- synthesis of diverse nanoparticles and their applications: a comprehensive overview. *RSC Adv.* 5, 105003–105037. <https://doi.org/10.1039/C5RA19388E>
- Dyar, M.D., Agresti, D.G., Schaefer, M.W., Grant, C.A., Sklute, E.C., 2006. MÖSSBAUER SPECTROSCOPY OF EARTH AND PLANETARY MATERIALS. *Annu. Rev. Earth Planet. Sci.* 34, 83–125. <https://doi.org/10.1146/annurev.earth.34.031405.125049>
- Ebrahiminezhad, A., Ghasemi, Y., Rasoul-Amini, S., Barar, J., Davaran, S., 2012. Impact of Amino-Acid Coating on the Synthesis and Characteristics of Iron-Oxide Nanoparticles (IONS). *Bulletin of the Korean Chemical Society* 33, 3957–3962. <https://doi.org/10.5012/BKCS.2012.33.12.3957>
- Fannin, P.C., Charles, S.W., 1989. The study of a ferrofluid exhibiting both Brownian and Neel relaxation. *J. Phys. D: Appl. Phys.* 22, 187–191. <https://doi.org/10.1088/0022-3727/22/1/027>
- Faraday, M., 1857. X. The Bakerian Lecture. —Experimental relations of gold (and other metals) to light. *Phil. Trans. R. Soc.* 147, 145–181. <https://doi.org/10.1098/rstl.1857.0011>
- Feynman, R., 1960. There's Plenty of Room at the Bottom. *Engineering and Science* 22–36.
- Figueroa, A.I., Bartolomé, J., García, L.M., Bartolomé, F., Arauzo, A., Millán, A., Palacio, F., 2015. Magnetic Anisotropy of Maghemite Nanoparticles Probed by RF Transverse Susceptibility. *Physics Procedia* 75, 1050–1057. <https://doi.org/10.1016/j.phpro.2015.12.174>
- Gaharwar, U.S., Meena, R., Rajamani, P., 2017. Iron oxide nanoparticles induced cytotoxicity, oxidative stress and DNA damage in lymphocytes: Iron oxide nanoparticles toxicity in lymphocytes. *J. Appl. Toxicol.* 37, 1232–1244. <https://doi.org/10.1002/jat.3485>
- Gaihre, B., Khil, M., Lee, D., Kim, H., 2009. Gelatin-coated magnetic iron oxide nanoparticles as carrier system: Drug loading and in vitro drug release study. *International Journal of Pharmaceutics* 365, 180–189. <https://doi.org/10.1016/j.ijpharm.2008.08.020>
- García-Jimeno, S., Estelrich, J., 2013. Ferrofluid based on polyethylene glycol-coated iron oxide nanoparticles: Characterization and properties. *Colloids and Surfaces A: Physicochemical and Engineering Aspects* 420, 74–81. <https://doi.org/10.1016/j.colsurfa.2012.12.022>
- Gaur, U., Sahoo, S.K., De, T.K., Ghosh, P.C., Maitra, A., Ghosh, P.K., 2000. Biodistribution of fluoresceinated dextran using novel nanoparticles evading reticuloendothelial system. *International Journal of Pharmaceutics* 202, 1–10. [https://doi.org/10.1016/S0378-5173\(99\)00447-0](https://doi.org/10.1016/S0378-5173(99)00447-0)
- Gonzalez-Fernandez, M.A., Torres, T.E., Andrés-Vergés, M., Costo, R., de la Presa, P., Serna, C.J., Morales, M.P., Marquina, C., Ibarra, M.R., Goya, G.F., 2009. Magnetic nanoparticles for power absorption: Optimizing size, shape and magnetic properties. *Journal of Solid State Chemistry* 182, 2779–2784. <https://doi.org/10.1016/j.jssc.2009.07.047>
- Grubbs, R.B., 2007. Roles of Polymer Ligands in Nanoparticle Stabilization. *Polymer Reviews* 47, 197–215. <https://doi.org/10.1080/15583720701271245>

- Gumieniczek-Chlopek, E., Odrobińska, J., Strączek, T., Radziszewska, A., Zapotoczny, S., Kapusta, C., 2020. Hydrophobically Coated Superparamagnetic Iron Oxides Nanoparticles Incorporated into Polymer-Based Nanocapsules Dispersed in Water. *Materials* 13, 1219. <https://doi.org/10.3390/ma13051219>**
- Gutfleisch, O., Martinez, N., Verdier, M., Harris, I.R., 1994. Development of microstructure of the disproportionated material during HDDR processes in a Nd₁₆Fe₇₆B₈ alloy. *Journal of Alloys and Compounds* 204, L21–L23. [https://doi.org/10.1016/0925-8388\(94\)90060-4](https://doi.org/10.1016/0925-8388(94)90060-4)
- Hansen, M.F., Mørup, S., 1999. Estimation of blocking temperatures from ZFC/FC curves. *Journal of Magnetism and Magnetic Materials* 203, 214–216. [https://doi.org/10.1016/S0304-8853\(99\)00238-3](https://doi.org/10.1016/S0304-8853(99)00238-3)
- Haracz, S., Hilgendorff, M., Rybka, J.D., Giersig, M., 2015. Effect of surfactant for magnetic properties of iron oxide nanoparticles. *Nuclear Instruments and Methods in Physics Research Section B: Beam Interactions with Materials and Atoms* 364, 120–126. <https://doi.org/10.1016/j.nimb.2015.08.035>
- Helgesen, G., Pieranski, P., Skjeltorp, A.T., 1990. Nonlinear phenomena in systems of magnetic holes. *Phys. Rev. Lett.* 64, 1425–1428. <https://doi.org/10.1103/PhysRevLett.64.1425>
- Hergt, R., Hiergeist, R., Hilger, I., Kaiser, W.A., Lapatnikov, Y., Margel, S., Richter, U., 2004. Maghemite nanoparticles with very high AC-losses for application in RF-magnetic hyperthermia. *Journal of Magnetism and Magnetic Materials* 270, 345–357. <https://doi.org/10.1016/j.jmmm.2003.09.001>
- Huang, J., Bu, L., Xie, J., Chen, K., Cheng, Z., Li, X., Chen, X., 2010. Effects of Nanoparticle Size on Cellular Uptake and Liver MRI with Polyvinylpyrrolidone-Coated Iron Oxide Nanoparticles. *ACS Nano* 4, 7151–7160. <https://doi.org/10.1021/nn101643u>
- ISO, 2015. ISO/TS 80004-2:2015.
- Jiang, S., Chen, Y., Duan, G., Mei, C., Greiner, A., Agarwal, S., 2018. Electrospun nanofiber reinforced composites: a review. *Polym. Chem.* 9, 2685–2720. <https://doi.org/10.1039/C8PY00378E>
- Jonsson, T., Mattsson, J., Nordblad, P., Svedlindh, P., 1997. Energy barrier distribution of a noninteracting nano-sized magnetic particle system. *Journal of Magnetism and Magnetic Materials* 168, 269–277. [https://doi.org/10.1016/S0304-8853\(96\)00710-X](https://doi.org/10.1016/S0304-8853(96)00710-X)
- Karak, N., 2009. *Fundamentals of polymers: raw materials to finish products*. PHI Learning Private Ltd., New Delhi.
- Karnas, K., Karewicz, A., Dulińska-Litewka, J., Strączek, T., Kapusta, C., Lekka, M., 2021. Interactions of the new SPION-based system bearing anti-N-cadherin antibodies with prostate cancer cells. Submitted to: “International Journal of Nanomedicine.”**
- Kim, D.K., Zhang, Y., Voit, W., Rao, K.V., Muhammed, M., 2001. Synthesis and characterization of surfactant-coated superparamagnetic monodispersed iron oxide nanoparticles. *Journal of Magnetism and Magnetic Materials* 225, 30–36. [https://doi.org/10.1016/S0304-8853\(00\)01224-5](https://doi.org/10.1016/S0304-8853(00)01224-5)

- Kittelson, D.B., 1998. Engines and nanoparticles. *Journal of Aerosol Science* 29, 575–588. [https://doi.org/10.1016/S0021-8502\(97\)10037-4](https://doi.org/10.1016/S0021-8502(97)10037-4)
- Komorida, Y., Mito, M., Deguchi, H., Takagi, S., Millán, A., Silva, N.J.O., Palacio, F., 2009. Surface and core magnetic anisotropy in maghemite nanoparticles determined by pressure experiments. *Appl. Phys. Lett.* 94, 202503. <https://doi.org/10.1063/1.3131782>
- KRAKsat, 2019. Ferrofluidowe koło zamachowe [WWW Document]. URL <https://www.kraksat.pl/space/ferrofluidowe-kolo-zamachowe/>
- Kronmüller, H., Fähnle, M., 2003. *Micromagnetism and the microstructure of ferromagnetic solids*, Cambridge studies in magnetism. Cambridge Univ. Press, Cambridge.
- Kundu, S., 2013. A new route for the formation of Au nanowires and application of shape-selective Au nanoparticles in SERS studies. *J. Mater. Chem. C* 1, 831–842. <https://doi.org/10.1039/C2TC00315E>
- Lacroix, L.-M., Malaki, R.B., Carrey, J., Lachaize, S., Respaud, M., Goya, G.F., Chaudret, B., 2009. Magnetic hyperthermia in single-domain monodisperse FeCo nanoparticles: Evidences for Stoner–Wohlfarth behavior and large losses. *Journal of Applied Physics* 105, 023911. <https://doi.org/10.1063/1.3068195>
- Lempart, M., Derkowski, A., Strączek, T., Kapusta, C., 2020. Systematics of H₂ and H₂O evolved from chlorites during oxidative dehydrogenation. *American Mineralogist* 105, 932–944. <https://doi.org/10.2138/am-2020-7326>**
- Lewandowska-Łańcucka, J., Staszewska, M., Szuwarzyński, M., Kępczyński, M., Romek, M., Tokarz, W., Szpak, A., Kania, G., Nowakowska, M., 2014. Synthesis and characterization of the superparamagnetic iron oxide nanoparticles modified with cationic chitosan and coated with silica shell. *Journal of Alloys and Compounds* 586, 45–51. <https://doi.org/10.1016/j.jallcom.2013.10.039>
- Li, J., Liu, X., Lin, Y., Qiu, X., Ma, X., Huang, Y., 2004. Field-induced transmission of light in ionic ferrofluids of tunable viscosity. *J. Phys. D: Appl. Phys.* 37, 3357–3360. <https://doi.org/10.1088/0022-3727/37/24/001>
- Lin, Y., Böker, A., He, J., Sill, K., Xiang, H., Abetz, C., Li, X., Wang, J., Emrick, T., Long, S., Wang, Q., Balazs, A., Russell, T.P., 2005. Self-directed self-assembly of nanoparticle/copolymer mixtures. *Nature* 434, 55–59. <https://doi.org/10.1038/nature03310>
- Ma, H., Qi, X., Maitani, Y., Nagai, T., 2007. Preparation and characterization of superparamagnetic iron oxide nanoparticles stabilized by alginate. *International Journal of Pharmaceutics* 333, 177–186. <https://doi.org/10.1016/j.ijpharm.2006.10.006>
- Mahmoudi, M., Serpooshan, V., 2012. Silver-Coated Engineered Magnetic Nanoparticles Are Promising for the Success in the Fight against Antibacterial Resistance Threat. *ACS Nano* 6, 2656–2664. <https://doi.org/10.1021/nn300042m>
- Martinez-Boubeta, C., Simeonidis, K., Makridis, A., Angelakeris, M., Iglesias, O., Guardia, P., Cabot, A., Yedra, L., Estradé, S., Peiró, F., Saggi, Z., Midgley, P.A., Conde-Leborán, I., Serantes, D., Baldomir, D., 2013. Learning from Nature to Improve the Heat Generation of Iron-Oxide Nanoparticles for

- Magnetic Hyperthermia Applications. *Sci Rep* 3, 1652. <https://doi.org/10.1038/srep01652>
- Maziarz, P., Matusik, J., Leiviskä, T., Strączek, T., Kapusta, C., Marek Woch, W., Tokarz, W., Górniak, K., 2019a. Toward highly effective and easily separable halloysite-containing adsorbents: The effect of iron oxide particles impregnation and new insight into As(V) removal mechanisms. *Separation and Purification Technology* 210, 390–401. <https://doi.org/10.1016/j.seppur.2018.08.012>**
- Maziarz, P., Matusik, J., Strączek, T., Kapusta, C., Woch, W.M., Tokarz, W., Radziszewska, A., Leiviskä, T., 2019b. Highly effective magnet-responsive LDH-Fe oxide composite adsorbents for As(V) removal. *Chemical Engineering Journal* 362, 207–216. <https://doi.org/10.1016/j.cej.2019.01.017>**
- Mirguet, C., Fredrickx, P., Sciau, P., Colombari, P., 2008. Origin of the self-organisation of Cu⁰/Ag⁰ nanoparticles in ancient lustre pottery. A TEM study. *Phase Transitions* 81, 253–266. <https://doi.org/10.1080/01411590701514433>
- Mössbauer, R.L., 1958. Kernresonanzabsorption von Gammastrahlung in Ir¹⁹¹. *Naturwissenschaften* 45, 538–539. <https://doi.org/10.1007/BF00632050>
- Müller, R., Hergt, R., Zeisberger, M., Gawalek, W., 2005. Preparation of magnetic nanoparticles with large specific loss power for heating applications. *Journal of Magnetism and Magnetic Materials* 289, 13–16. <https://doi.org/10.1016/j.jmmm.2004.11.005>
- Murad, E., Johnston, J.H., 1989. Iron Oxides and Oxyhydroxides, in: Long, G.J., Grandjean, F. (Eds.), *Mössbauer Spectroscopy Applied to Inorganic Chemistry*. Springer US, Boston, MA. <https://doi.org/10.1007/978-1-4899-2289-2>
- Néel, L., 1949. Influence des fluctuations thermiques sur l'aimantation de grains ferromagnétiques très fins. *Comptes Rendus Hebdomadaires Des Seances De L Academie Des Sciences* 228, 664–666.
- Okunev, V.D., Szymczak, H., Szymczak, R., Gierłowski, P., Glot, A.B., Bondarchuk, A.N., Burkhovetski, V.V., 2016. Effect of oxygen clusters on optics, magnetism, and conductivity of (In₂O₃)_{0.9}(SrO)_{0.1}. *Solid State Communications* 231–232, 31–35. <https://doi.org/10.1016/j.ssc.2016.01.022>
- Ono, M., Igarashi, T., Ohno, E., Sasaki, M., 1995. Unusual thermal defence by a honeybee against mass attack by hornets. *Nature* 377, 334–336. <https://doi.org/10.1038/377334a0>
- Ott, L.S., Finke, R.G., 2006. Nanocluster Formation and Stabilization Fundamental Studies: † Investigating “Solvent-Only” Stabilization En Route to Discovering Stabilization by the Traditionally Weakly Coordinating Anion BF₄⁻ Plus High Dielectric Constant Solvents. *Inorg. Chem.* 45, 8382–8393. <https://doi.org/10.1021/ic060876s>
- Padovani, S., Sada, C., Mazzoldi, P., Brunetti, B., Borgia, I., Sgamellotti, A., Giulivi, A., D'Acapito, F., Battaglin, G., 2003. Copper in glazes of Renaissance lustre pottery: Nanoparticles, ions, and local environment. *Journal of Applied Physics* 93, 10058–10063. <https://doi.org/10.1063/1.1571965>
- Patterson, A.L., 1939. The Scherrer Formula for X-Ray Particle Size Determination. *Phys. Rev.* 56, 978–982. <https://doi.org/10.1103/PhysRev.56.978>

- Pollert, E., Knížek, K., Maryško, M., Kašpar, P., Vasseur, S., Duguet, E., 2007. New - tuned magnetic nanoparticles for self-controlled hyperthermia. *Journal of Magnetism and Magnetic Materials* 316, 122–125. <https://doi.org/10.1016/j.jmmm.2007.02.031>
- Rancourt, D.G., 1996. Analytical Methods for Mössbauer Spectral Analysis of Complex Materials, in: Long, G.J., Grandjean, F. (Eds.), *Mössbauer Spectroscopy Applied to Magnetism and Materials Science*. Springer US, Boston, MA, pp. 105–124. https://doi.org/10.1007/978-1-4899-1763-8_5
- Rancourt, D.G., McDonald, A.M., Lalonde, A.E., Ping, J.Y., 1993. Mössbauer absorber thicknesses for accurate site populations in Fe-bearing minerals. *American Mineralogist* 78, 1–7.
- Roduner, E., 2006. Size matters: why nanomaterials are different. *Chem. Soc. Rev.* 35, 583–592. <https://doi.org/10.1039/B502142C>
- Romodina, M.N., Lyubin, E.V., Fedyanin, A.A., 2016. Detection of Brownian Torque in a Magnetically-Driven Rotating Microsystem. *Sci Rep* 6, 21212. <https://doi.org/10.1038/srep21212>
- Rose, H., 1994. Correction of aberrations, a promising means for improving the spatial and energy resolution of energy-filtering electron microscopes. *Ultramicroscopy* 56, 11–25. [https://doi.org/10.1016/0304-3991\(94\)90142-2](https://doi.org/10.1016/0304-3991(94)90142-2)
- Scherrer, P., 1912. Bestimmung der inneren Struktur und der Größe von Kolloidteilchen mittels Röntgenstrahlen, in: *Kolloidchemie Ein Lehrbuch*. Springer Berlin Heidelberg, Berlin, Heidelberg, pp. 387–409. https://doi.org/10.1007/978-3-662-33915-2_7
- Schleich, N., Sibret, P., Danhier, P., Ucar, B., Laurent, S., Muller, R.N., Jérôme, C., Gallez, B., Prétat, V., Danhier, F., 2013. Dual anticancer drug/superparamagnetic iron oxide-loaded PLGA-based nanoparticles for cancer therapy and magnetic resonance imaging. *International Journal of Pharmaceutics* 447, 94–101. <https://doi.org/10.1016/j.ijpharm.2013.02.042>
- Segal, V., Hjortsberg, A., Rabinovich, A., Nattrass, D., Raj, K., 1998. AC (60 Hz) and impulse breakdown strength of a colloidal fluid based on transformer oil and magnetite nanoparticles, in: *Conference Record of the 1998 IEEE International Symposium on Electrical Insulation (Cat. No.98CH36239)*. Presented at the Conference Record of the 1998 IEEE International Symposium on Electrical Insulation, IEEE, Arlington, VA, USA, pp. 619–622. <https://doi.org/10.1109/ELINSL.1998.694869>
- Shima, P.D., Philip, J., Raj, B., 2009. Role of microconvection induced by Brownian motion of nanoparticles in the enhanced thermal conductivity of stable nanofluids. *Appl. Phys. Lett.* 94, 223101. <https://doi.org/10.1063/1.3147855>
- Shliomis, M., Raikher, Yu., 1980. Experimental investigations of magnetic fluids. *IEEE Trans. Magn.* 16, 237–250. <https://doi.org/10.1109/TMAG.1980.1060590>
- Singh, V., Banerjee, V., Sharma, M., 2009. Dynamics of magnetic nanoparticle suspensions. *J. Phys. D: Appl. Phys.* 42, 245006. <https://doi.org/10.1088/0022-3727/42/24/245006>
- Slomkowski, S., Alemán, J.V., Gilbert, R.G., Hess, M., Horie, K., Jones, R.G., Kubisa, P., Meisel, I., Mormann, W., Penczek, S., Stepto, R.F.T., 2011. Terminology of polymers and polymerization processes in dispersed systems (IUPAC

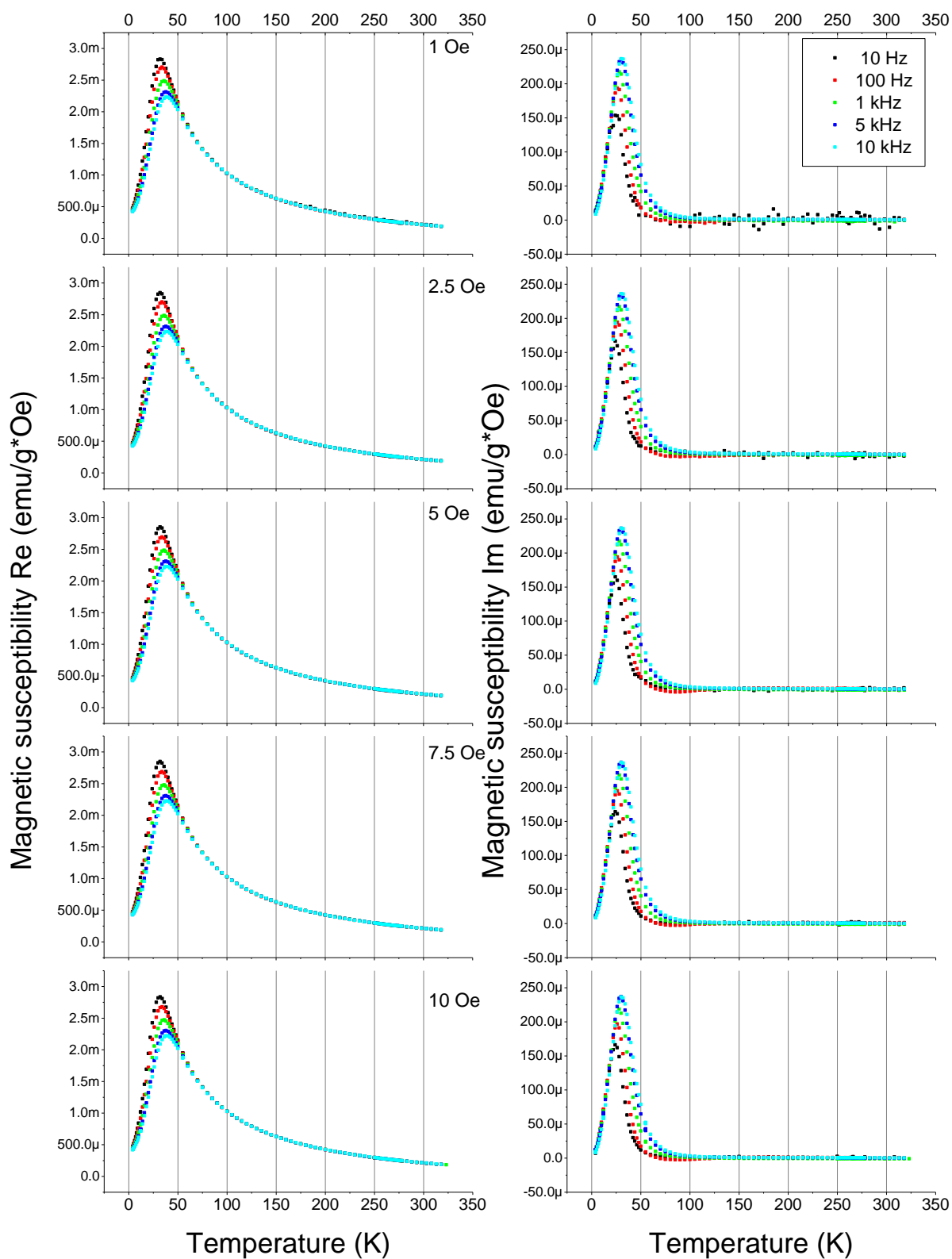
- Recommendations 2011). *Pure and Applied Chemistry* 83, 2229–2259. <https://doi.org/10.1351/PAC-REC-10-06-03>
- Stoner, E.C., Wohlfarth, E.P., 1948. A mechanism of magnetic hysteresis in heterogeneous alloys. *Phil. Trans. R. Soc. Lond. A* 240, 599–642. <https://doi.org/10.1098/rsta.1948.0007>
- Sun, C., Lee, J.S.H., Zhang, M., 2008. Magnetic nanoparticles in MR imaging and drug delivery. *Advanced Drug Delivery Reviews* 60, 1252–1265. <https://doi.org/10.1016/j.addr.2008.03.018>
- Szpak, A., Fiejdasz, S., Prendota, W., Strączek, T., Kapusta, C., Szmyd, J., Nowakowska, M., Zapotoczny, S., 2014. T1–T2 Dual-modal MRI contrast agents based on superparamagnetic iron oxide nanoparticles with surface attached gadolinium complexes. *J Nanopart Res* 16, 2678. <https://doi.org/10.1007/s11051-014-2678-6>**
- Szpak, A., Kania, G., Skórka, T., Tokarz, W., Zapotoczny, S., Nowakowska, M., 2013. Stable aqueous dispersion of superparamagnetic iron oxide nanoparticles protected by charged chitosan derivatives. *J Nanopart Res* 15, 1372. <https://doi.org/10.1007/s11051-012-1372-9>
- Tadros, T. (Ed.), 2013. *Encyclopedia of Colloid and Interface Science*. Springer Berlin Heidelberg, Berlin, Heidelberg. <https://doi.org/10.1007/978-3-642-20665-8>
- Tassa, C., Shaw, S.Y., Weissleder, R., 2011. Dextran-Coated Iron Oxide Nanoparticles: A Versatile Platform for Targeted Molecular Imaging, Molecular Diagnostics, and Therapy. *Acc. Chem. Res.* 44, 842–852. <https://doi.org/10.1021/ar200084x>
- Tolea, F., Sofronie, M., Birsan, A., Schinteie, G., Kuncser, V., Valeanu, M., 2010. Magnetic Nanocomposites for Permanent Magnets, in: Bârsan, V., Aldea, A. (Eds.), *Trends in Nanophysics, Engineering Materials*. Springer Berlin Heidelberg, Berlin, Heidelberg, pp. 287–296. https://doi.org/10.1007/978-3-642-12070-1_12
- Tsai, T.-H., Kuo, L.-S., Chen, P.-H., Lee, D., Yang, C.-T., 2010. Applications of Ferro-Nanofluid on a Micro-Transformer. *Sensors* 10, 8161–8172. <https://doi.org/10.3390/s100908161>
- Unsoy, G., Yalcin, S., Khodadust, R., Gunduz, G., Gunduz, U., 2012. Synthesis optimization and characterization of chitosan-coated iron oxide nanoparticles produced for biomedical applications. *J Nanopart Res* 14, 964. <https://doi.org/10.1007/s11051-012-0964-8>
- Veiseh, O., Gunn, J.W., Zhang, M., 2010. Design and fabrication of magnetic nanoparticles for targeted drug delivery and imaging. *Advanced Drug Delivery Reviews* 62, 284–304. <https://doi.org/10.1016/j.addr.2009.11.002>
- Verwey, E.J.W., Haayman, P.W., 1941. Electronic conductivity and transition point of magnetite (“Fe₃O₄”). *Physica* 8, 979–987. [https://doi.org/10.1016/S0031-8914\(41\)80005-6](https://doi.org/10.1016/S0031-8914(41)80005-6)
- Wang, B., Zhang, Y., Zhang, L., 2018. Recent progress on micro- and nano-robots: towards in vivo tracking and localization. *Quant. Imaging Med. Surg.* 8, 461–479. <https://doi.org/10.21037/qims.2018.06.07>
- Weissleder, R., Elizondo, G., Wittenberg, J., Rabito, C.A., Bengel, H.H., Josephson, L., 1990. Ultrasmall superparamagnetic iron oxide: characterization of a new

- class of contrast agents for MR imaging. *Radiology* 175, 489–493. <https://doi.org/10.1148/radiology.175.2.2326474>
- Widder, D., Greif, W., Widder, K., Edelman, R., Brady, T., 1987. Magnetite albumin microspheres: a new MR contrast material. *American Journal of Roentgenology* 148, 399–404. <https://doi.org/10.2214/ajr.148.2.399>
- Williamson, G.K., Hall, W.H., 1953. X-ray line broadening from fcc aluminium and wolfram. *Acta Metallurgica* 1, 22–31. [https://doi.org/10.1016/0001-6160\(53\)90006-6](https://doi.org/10.1016/0001-6160(53)90006-6)
- Wu, R., Ding, S., Lai, Y., Tian, G., Yang, J., 2018. Enhancement of exchange bias in ferromagnetic/antiferromagnetic core-shell nanoparticles through ferromagnetic domain wall formation. *Phys. Rev. B* 97, 024428. <https://doi.org/10.1103/PhysRevB.97.024428>
- Yang, L., Cui, F., Cun, D., Tao, A., Shi, K., Lin, W., 2007. Preparation, characterization and biodistribution of the lactone form of 10-hydroxycamptothecin (HCPT)-loaded bovine serum albumin (BSA) nanoparticles. *International Journal of Pharmaceutics* 340, 163–172. <https://doi.org/10.1016/j.ijpharm.2007.03.028>
- Yang, X., Yang, M., Pang, B., Vara, M., Xia, Y., 2015. Gold Nanomaterials at Work in Biomedicine. *Chem. Rev.* 115, 10410–10488. <https://doi.org/10.1021/acs.chemrev.5b00193>
- Yoo, D., Lee, J.-H., Shin, T.-H., Cheon, J., 2011. Theranostic Magnetic Nanoparticles. *Acc. Chem. Res.* 44, 863–874. <https://doi.org/10.1021/ar200085c>
- Zhang, W., 2003. Nanoscale Iron Particles for Environmental Remediation: An Overview. *Journal of Nanoparticle Research* 5, 323–332. <https://doi.org/10.1023/A:1025520116015>
- Zhao, Y., Li, C., Liu, X., Gu, F., Jiang, H., Shao, W., Zhang, L., He, Y., 2007. Synthesis and optical properties of TiO₂ nanoparticles. *Materials Letters* 61, 79–83. <https://doi.org/10.1016/j.matlet.2006.04.010>
- Zhen, G., Muir, B.W., Moffat, B.A., Harbour, P., Murray, K.S., Moubaraki, B., Suzuki, K., Madsen, I., Agron-Olshina, N., Waddington, L., Mulvaney, P., Hartley, P.G., 2011. Comparative Study of the Magnetic Behavior of Spherical and Cubic Superparamagnetic Iron Oxide Nanoparticles. *J. Phys. Chem. C* 115, 327–334. <https://doi.org/10.1021/jp104953z>
- Zheng, X., Deng, J., Wang, N., Deng, D., Zhang, W.-H., Bao, X., Li, C., 2014. Podlike N-Doped Carbon Nanotubes Encapsulating FeNi Alloy Nanoparticles: High-Performance Counter Electrode Materials for Dye-Sensitized Solar Cells. *Angew. Chem. Int. Ed.* 53, 7023–7027. <https://doi.org/10.1002/anie.201400388>
- Zhu, Q., Tao, F., Pan, Q., 2010. Fast and Selective Removal of Oils from Water Surface via Highly Hydrophobic Core–Shell Fe₂O₃@C Nanoparticles under Magnetic Field. *ACS Appl. Mater. Interfaces* 2, 3141–3146. <https://doi.org/10.1021/am1006194>

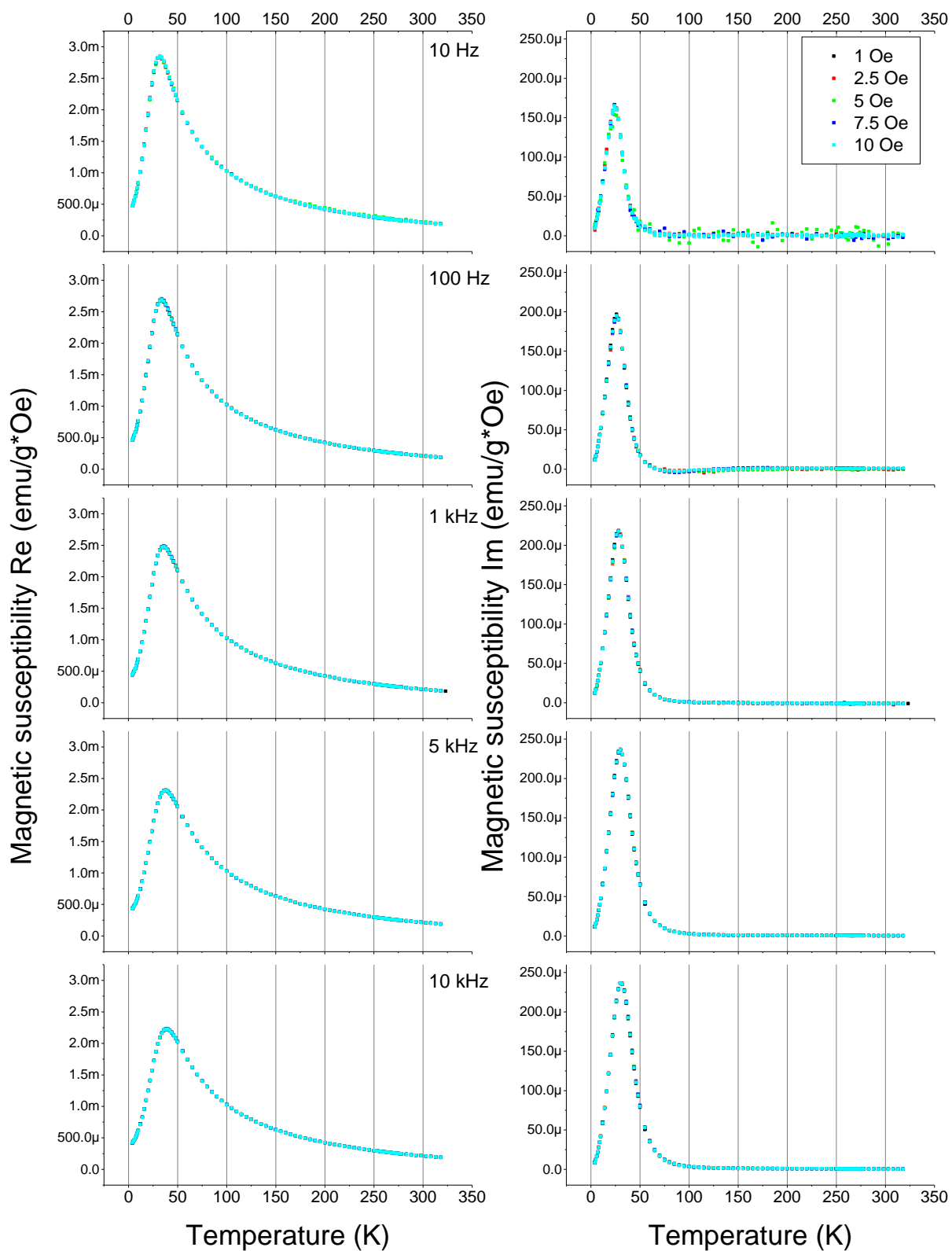
A. Appendix

1. Additional ACMS data

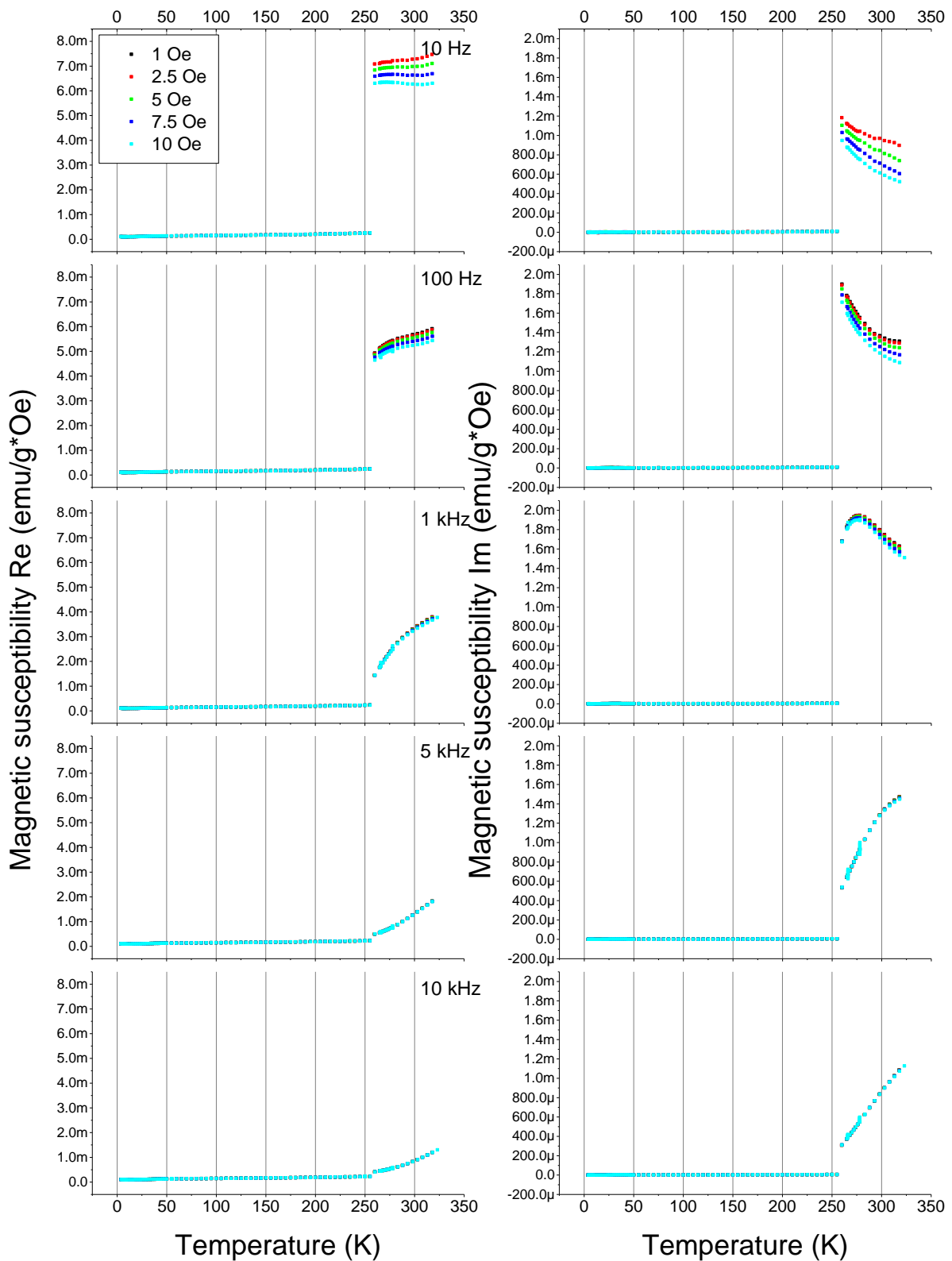
As mentioned in the main body of the thesis the ACMS data were collected for five different amplitudes and five different frequencies for each sample. Only the results for 10 Oe were presented. At the following pages the data for remaining amplitudes are presented for every sample. The data are shown on two pages: on the first one they are grouped in by frequency and on the other by magnetic field amplitude. This confirms that at low magnetic field amplitudes the magnetic susceptibility exhibits paramagnetic behavior (it is independent of the field amplitude) but for DEX IONP and SPION Gd samples the absorption part contribution raises with increasing AC field amplitude.



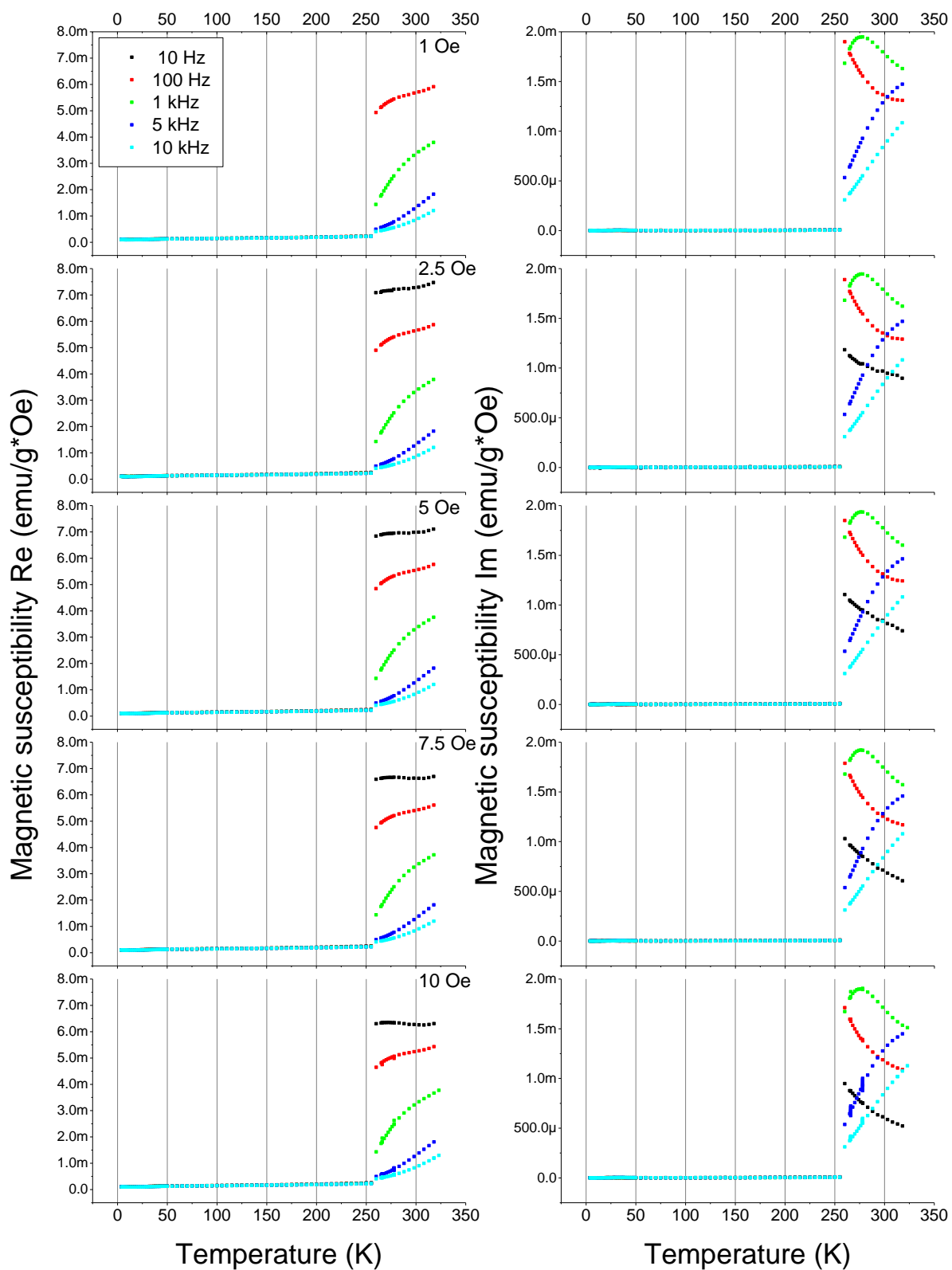
Graph A-I Temperature dependence of magnetic susceptibility of the DEX IONP sample without constant external field and with AC field grouped by the frequency. The dispersion part is presented in the left panel and the absorption part is shown in the right panel.



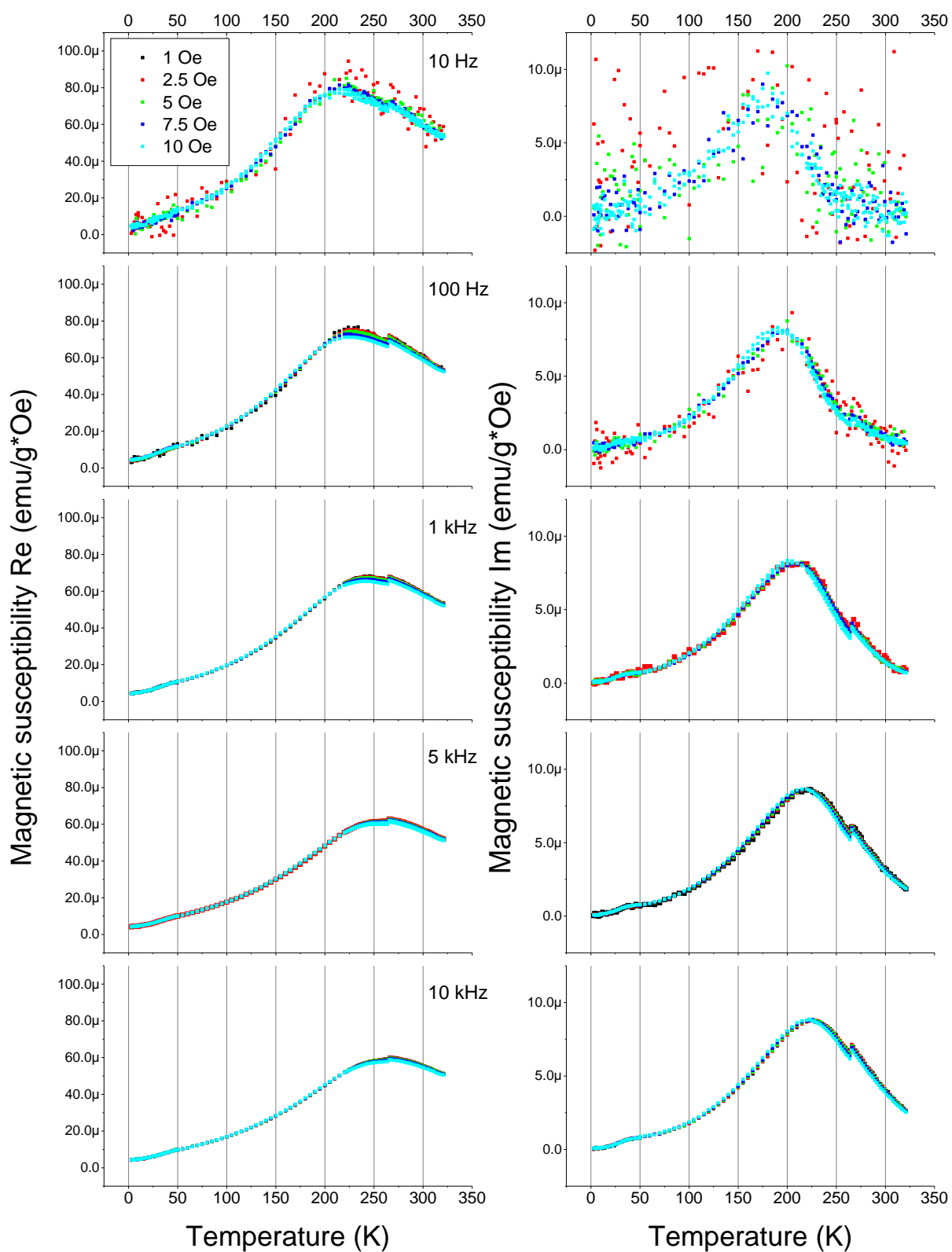
Graph A-II Temperature dependence of magnetic susceptibility of the DEX IONP sample without constant external field and with AC field grouped by the amplitude. The dispersion part is presented in the left panel and the absorption part is shown in the right panel.



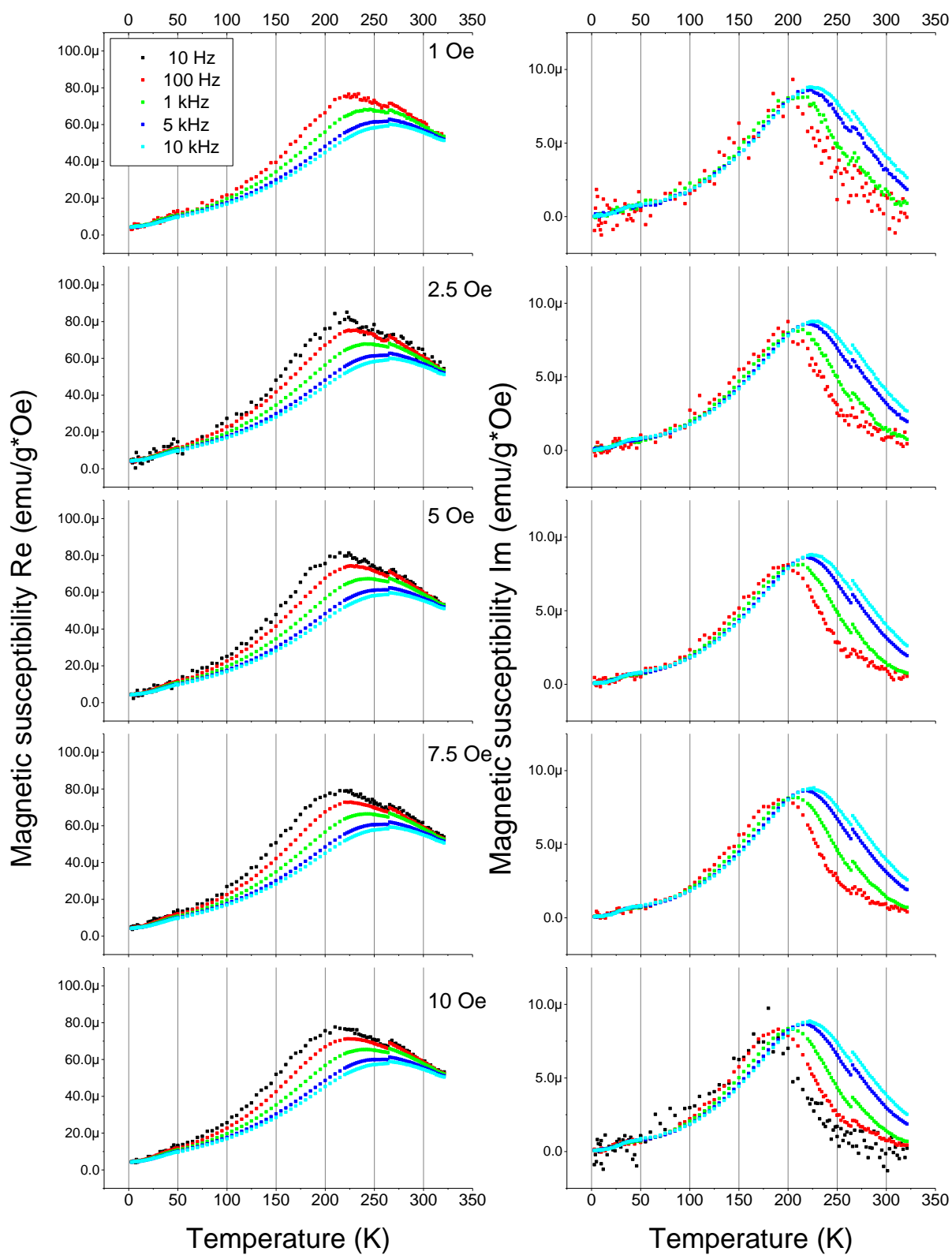
Graph A-III Temperature dependence of magnetic susceptibility of the PEG IONP sample without constant external field and with AC field grouped by the frequency. The dispersion part is presented in the left panel and the absorption part is shown in the right panel.



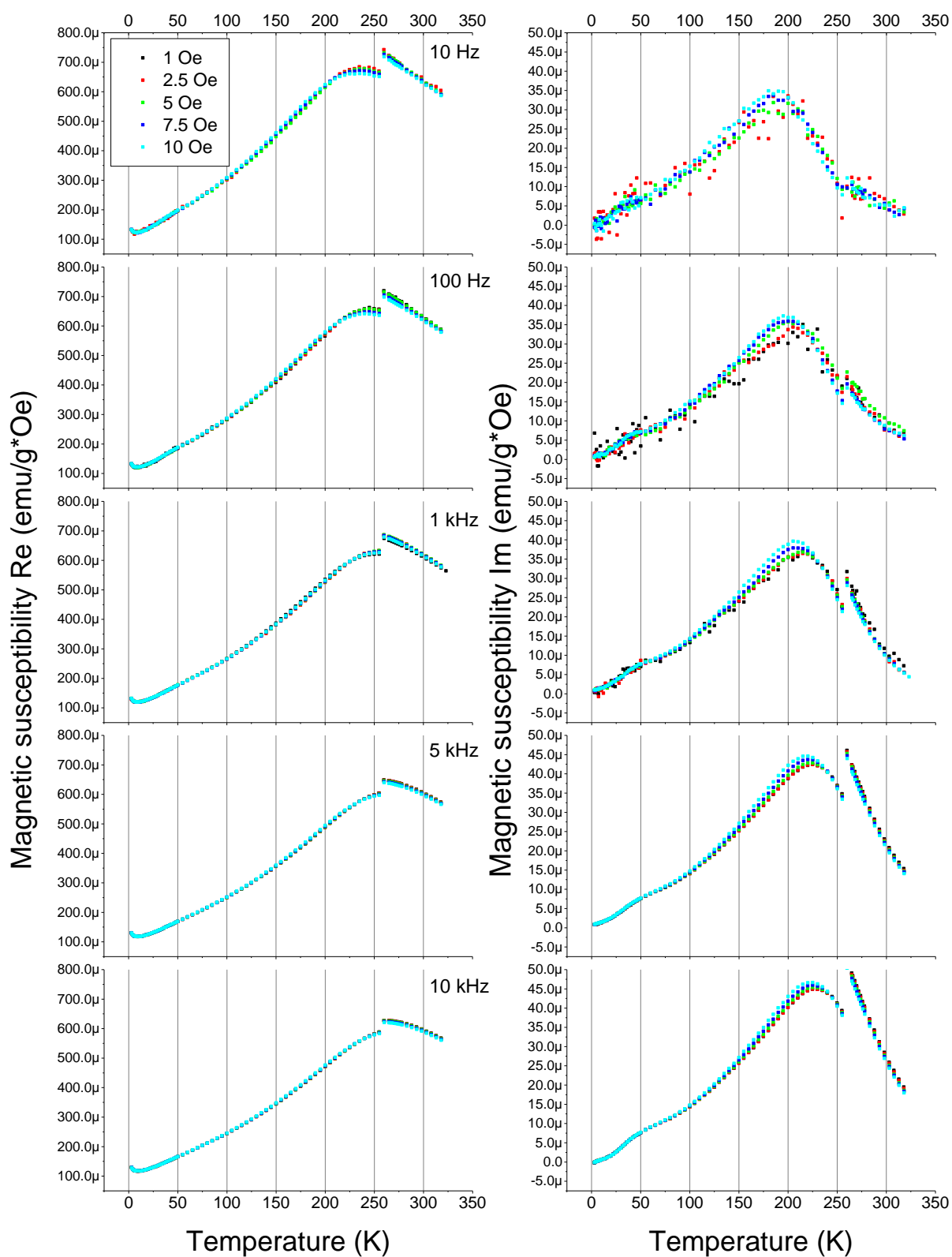
Graph A-IV Temperature dependence of magnetic susceptibility of the DEX IONP sample without constant external field and with AC field grouped by the amplitude. The dispersion part is presented in the left panel and the absorption part is shown in the right panel.



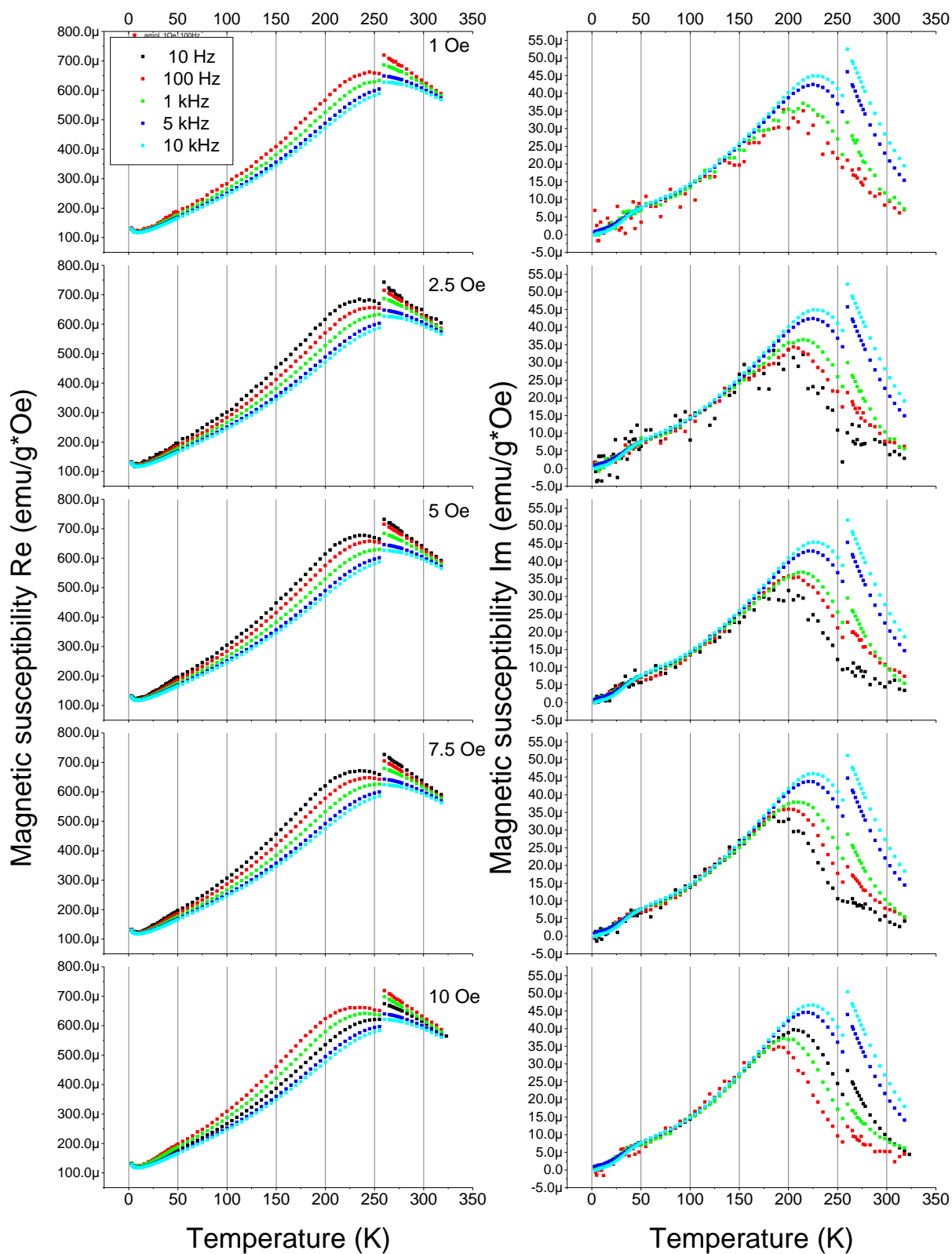
Graph A-V Temperature dependence of magnetic susceptibility of the SPION CCh sample without constant external field and with AC field grouped by the frequency. The dispersion part is presented in the left panel and the absorption part is shown in the right panel.



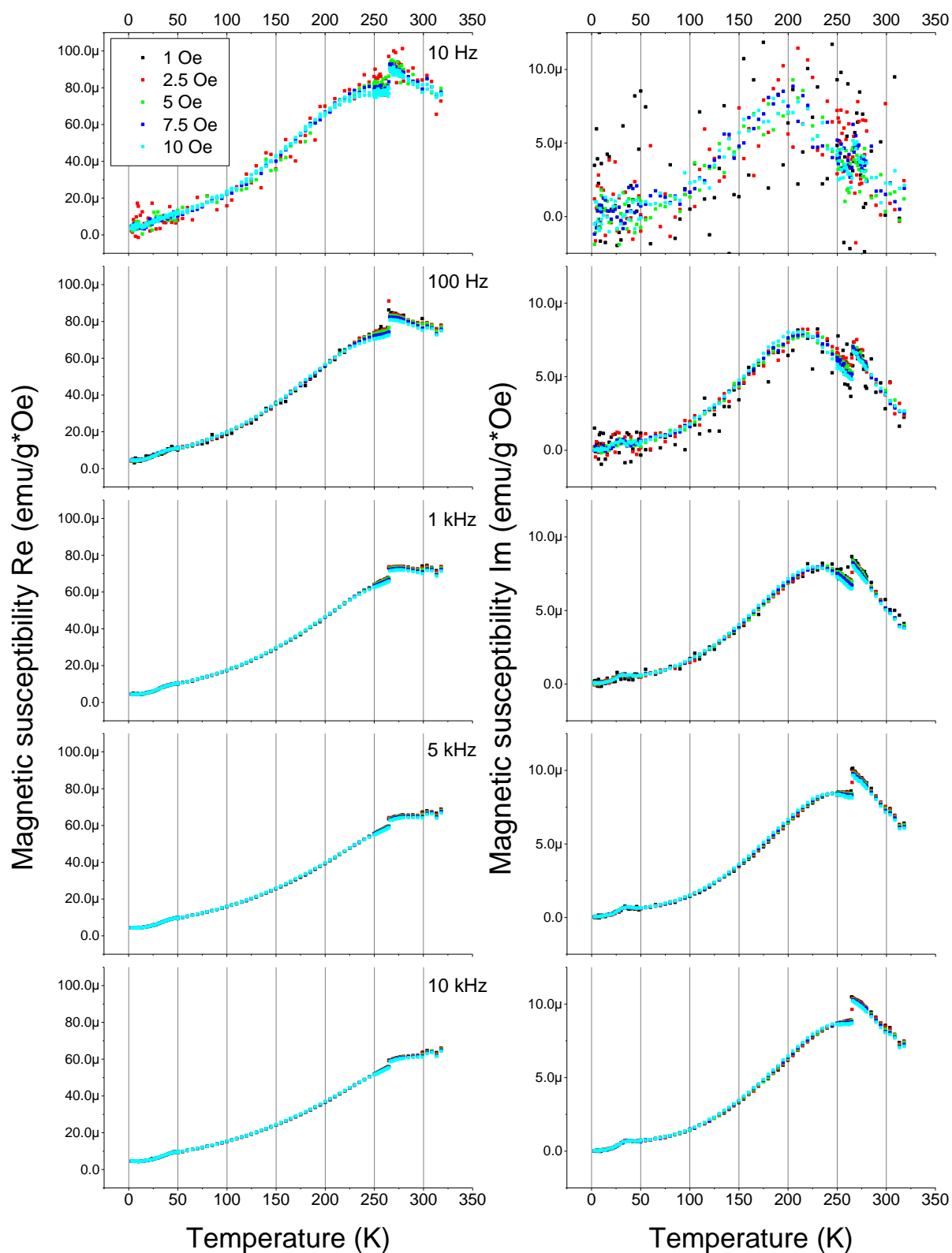
Graph A-VI Temperature dependence of magnetic susceptibility of the SPION CCh sample without constant external field and with AC field grouped by the amplitude. The dispersion part is presented in the left panel and the absorption part is shown in the right panel.



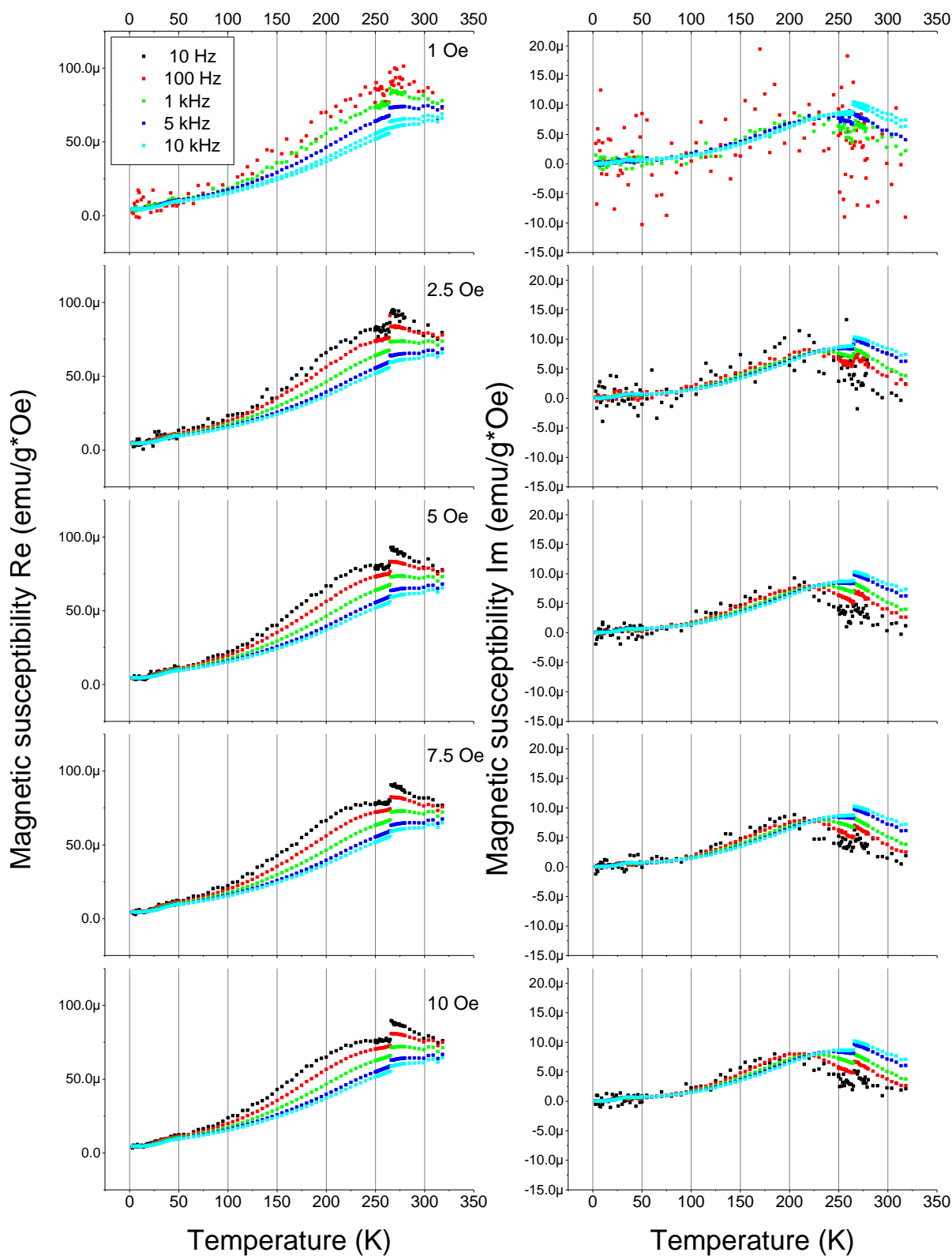
Graph A-VII Temperature dependence of magnetic susceptibility of the SPION CChB sample without constant external field and with AC field grouped by the frequency. The dispersion part is presented in the left panel and the absorption part is shown in the right panel.



Graph A-VIII Temperature dependence of magnetic susceptibility of the SPION CChB sample without constant external field and with AC field grouped by the amplitude. The dispersion part is presented in the left panel and the absorption part is shown in the right panel.



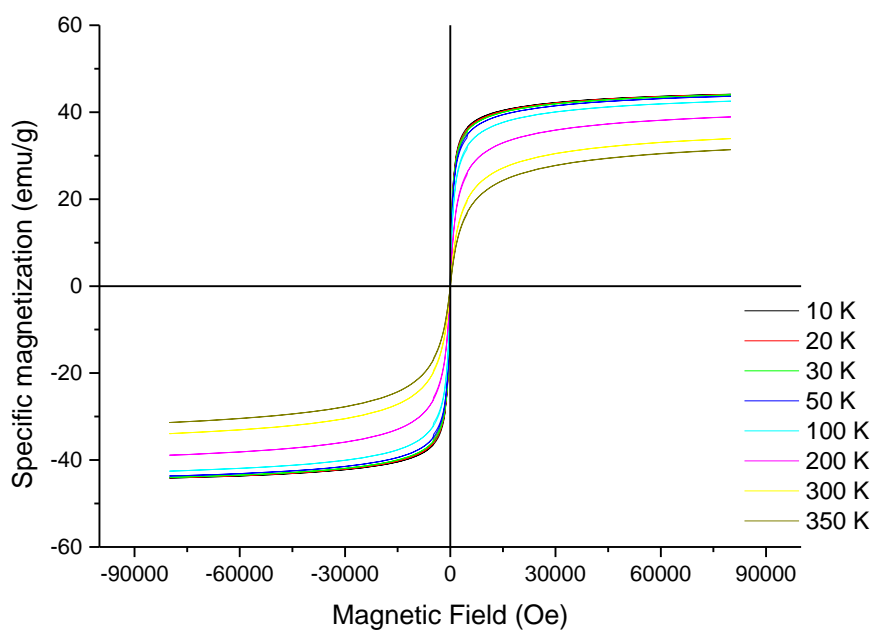
Graph A-IX Temperature dependence of magnetic susceptibility of the SPION Gd sample without constant external field and with AC field grouped by the frequency. The dispersion part is presented in the left panel and the absorption part is shown in the right panel.



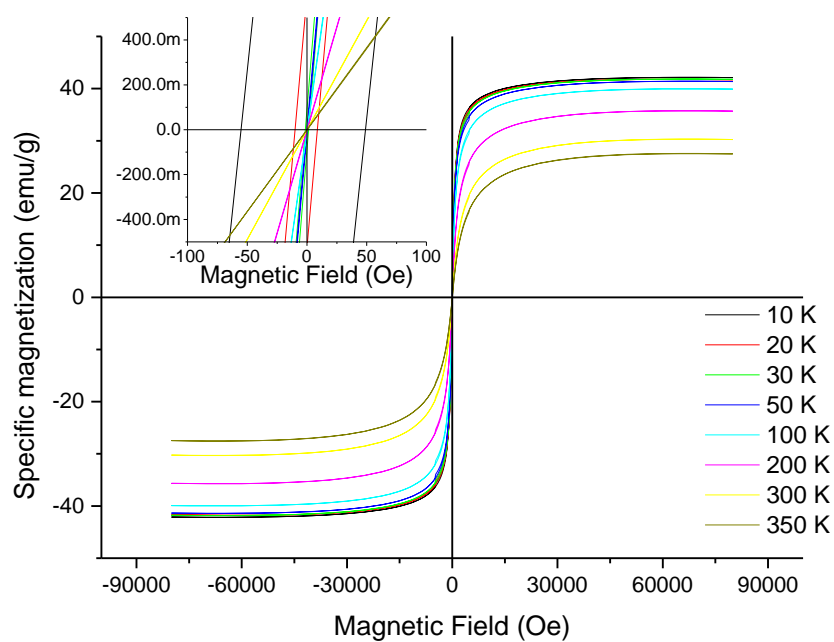
Graph A-X Temperature dependence of magnetic susceptibility of the SPION Gd sample without constant external field and with AC field grouped by the amplitude. The dispersion part is presented in the left panel and the absorption part is shown in the right panel.

2. Raw VSM data

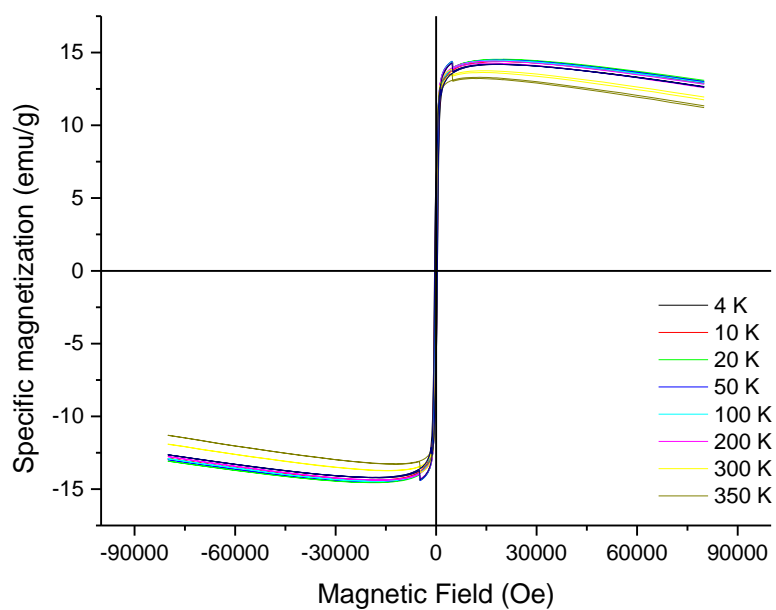
The thesis contains results of magnetic hysteresis loops from the VSM contained in the Graph V-V and one set of loops only for SPION Gd sample. The magnetic hysteresis loops for all other samples are presented on next few pages. For every sample there are two graphs, one presents raw data and the second one data with subtracted diamagnetic part.



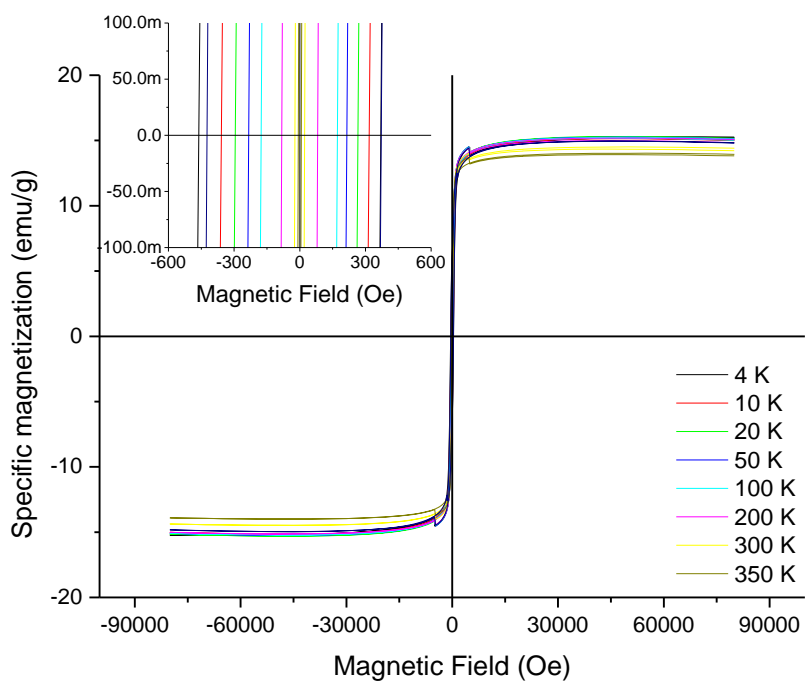
Graph A-XI Magnetic hysteresis loops of the DEX IONP sample carried out at different temperatures.



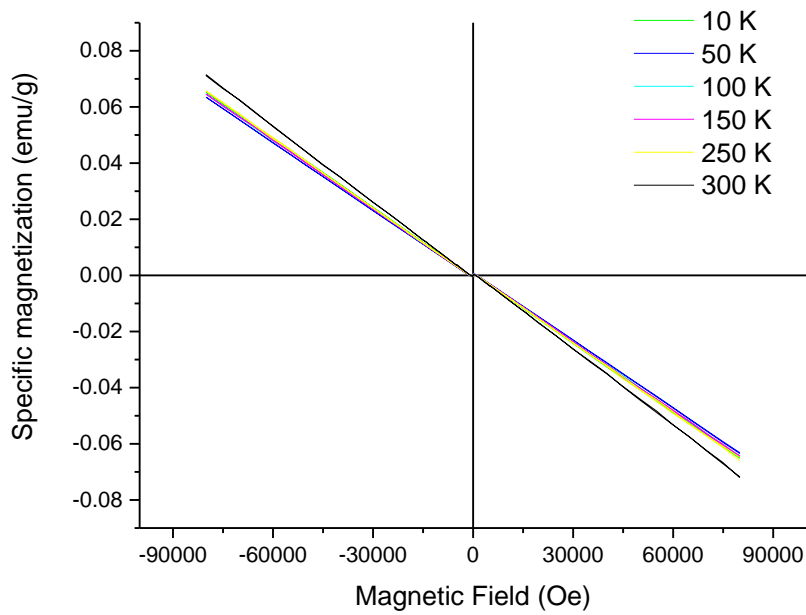
Graph A-XII Magnetic hysteresis loops of the DEX IONP sample after subtraction of the diamagnetic contribution from the loops. Inset shows enlarged area around the zero external magnetic field.



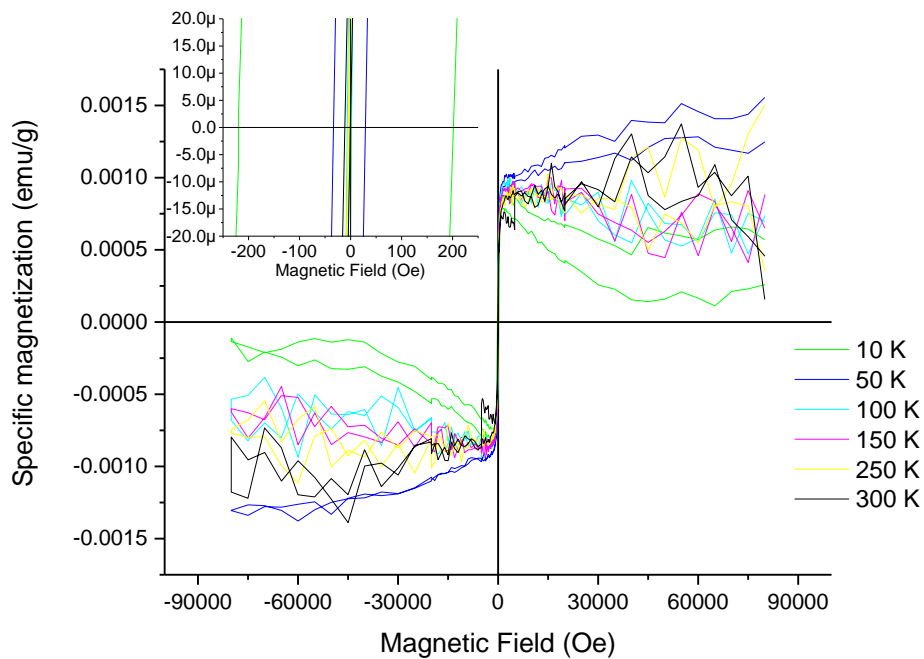
Graph A-XIII Magnetic hysteresis loops of the PEG IONP sample carried out at different temperatures.



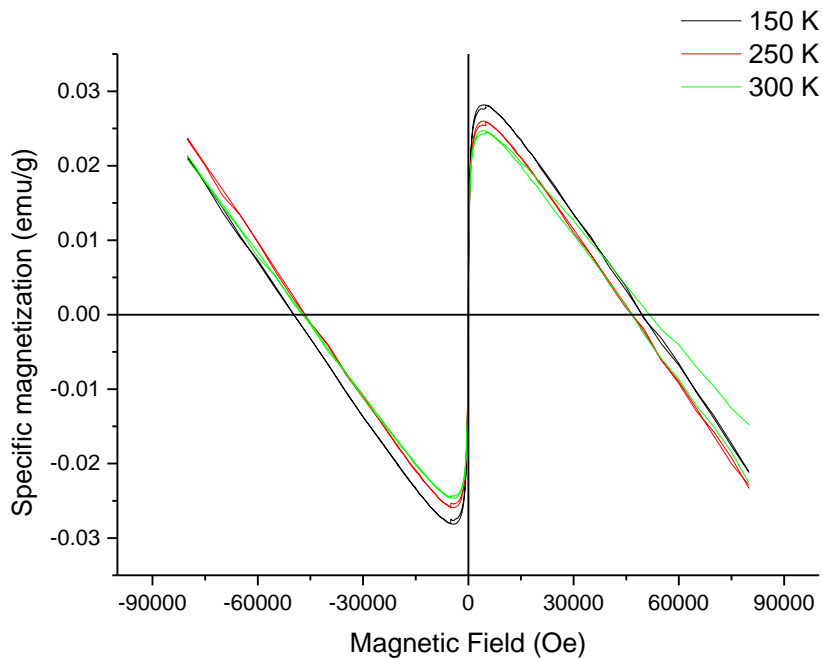
Graph A-XIV Magnetic hysteresis loops of the PEG IONP sample after subtraction of the diamagnetic contribution from the loops. Inset shows enlarged area around the zero external magnetic field.



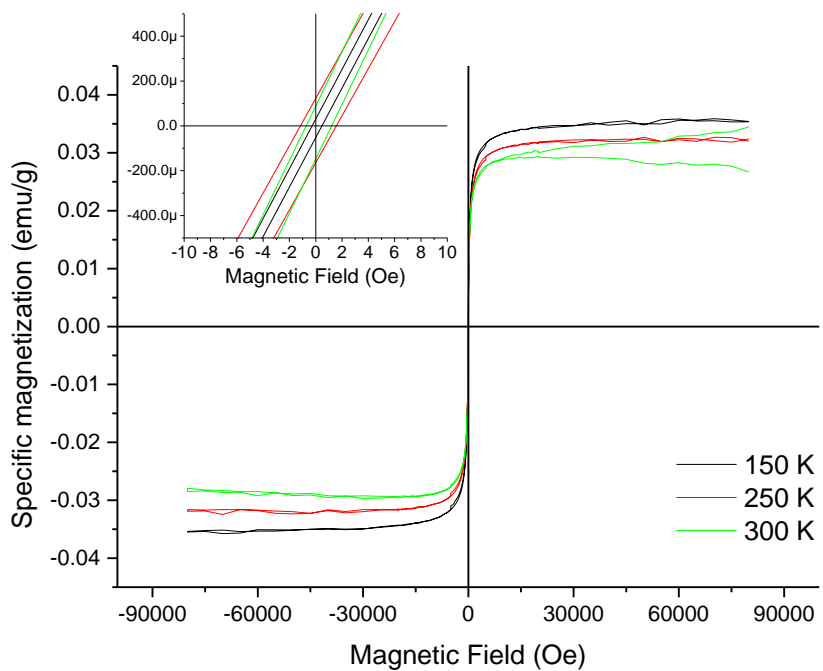
Graph A-XV Magnetic hysteresis loops of the SPION CCh sample in water suspension carried out at different temperatures.



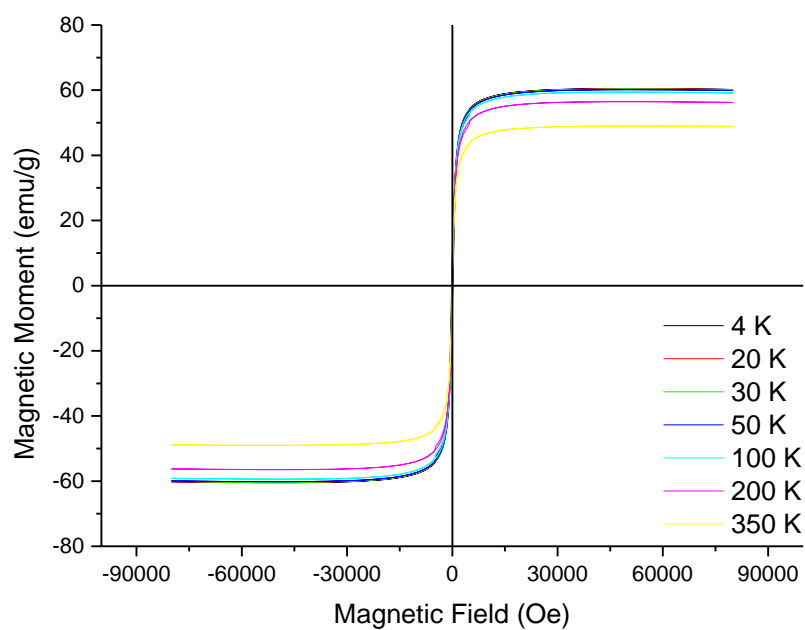
Graph A-XVI Magnetic hysteresis loops of the SPION CCh sample in water suspension after subtraction of the diamagnetic contribution from the loops. Inset shows enlarged area around the zero external magnetic field.



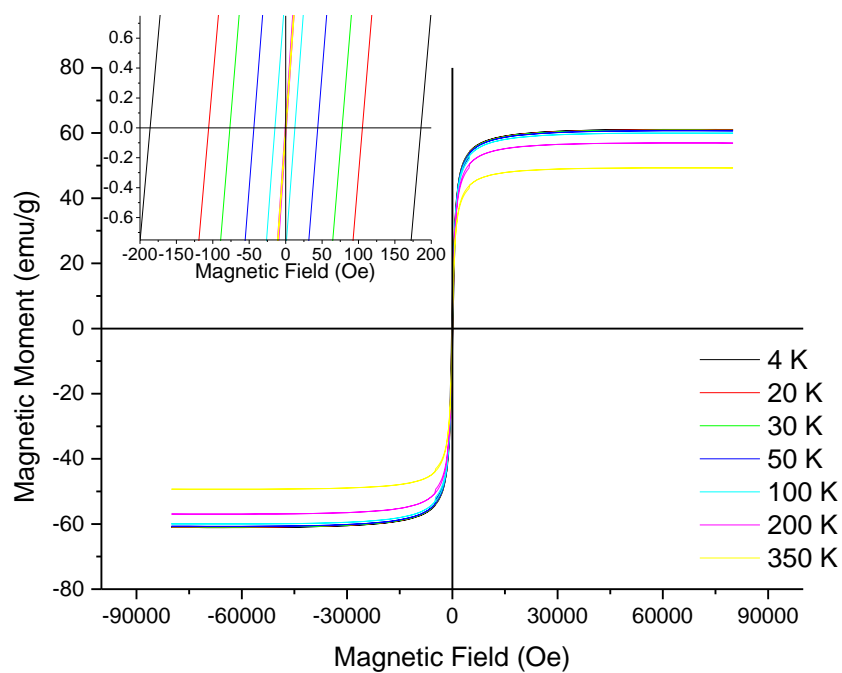
Graph A-XVII Magnetic hysteresis loops of the SIPON CChB sample in water suspension carried out at different temperatures.



Graph A-XVIII Magnetic hysteresis loops of the SPION CCh sample in water suspension after subtraction of the diamagnetic contribution from the loops. Inset shows enlarged area around the zero external magnetic field.

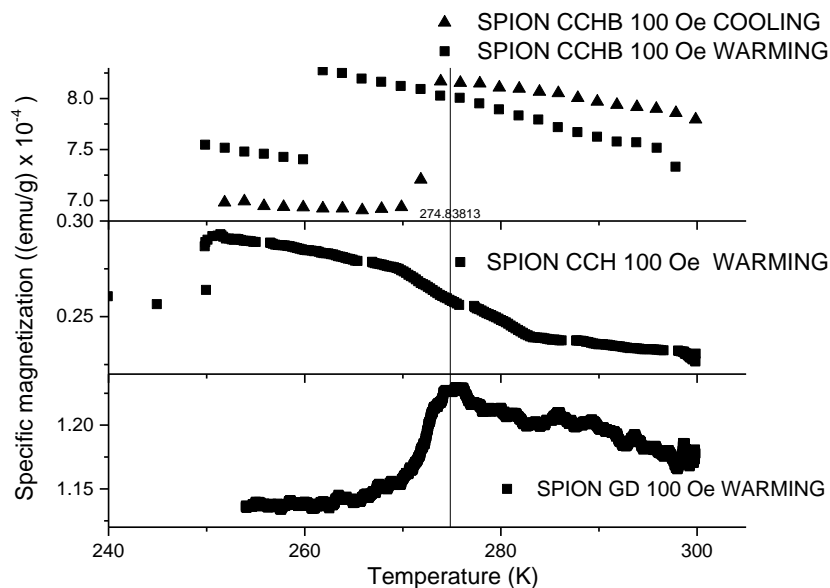


Graph A-XIX Magnetic hysteresis loops of the SIPON CChB sample carried out at different temperatures.



Graph A-XX Magnetic hysteresis loops of the SPION CCh sample after subtraction of the diamagnetic contribution from the loops. Inset shows enlarged area around the zero external magnetic field.

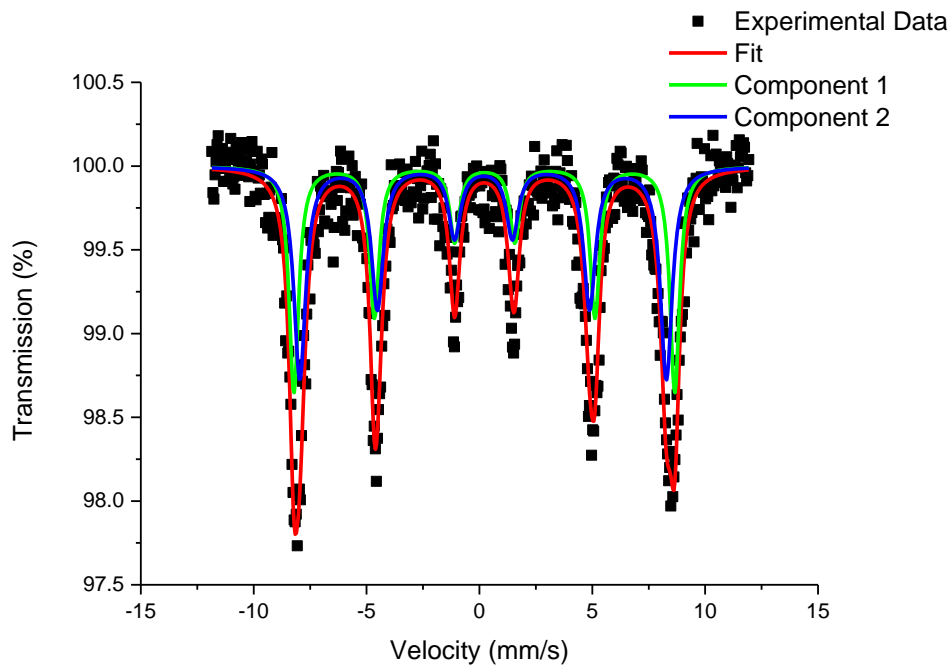
Because of a possible leakage risk, the liquid samples were measured in a two stage process. At temperatures higher than 250 K measurements were conducted in a helium atmosphere with a small overpressure condition. Below 250 K, where it was assumed that the sample is frozen, the measurement was continued in vacuum (~20 Torr). Measurements taken above 250 K are shown in Graph A-XXI and show an interesting behavior. Close to the freezing temperature magnetic susceptibility suddenly decreases when the sample is cooled down or increases when it is heated up. The explanation of the rise above the freezing temperature might be that previously randomly oriented particles align themselves to the field and thus the magnetization occurs always along easy axis which exhibits itself as a rise in magnetic susceptibility. On the other hand if that was the case, when the temperature falls beyond freezing the particles should remain organized so there wouldn't be any change in susceptibility, but experiment shows it isn't the case. Another explanation might be that the changes of susceptibility are the consequence of enabling or disabling rotational diffusion of the Brownian relaxation. The apparent hysteresis visible on the SPION CChB data is a result of continues, not stabilized, measurement which always results in some gap between heating and cooling curves due to the thermal mass.



Graph A-XXI Parts of FC-ZFC curves in temperature region between 250 k and 300 K.

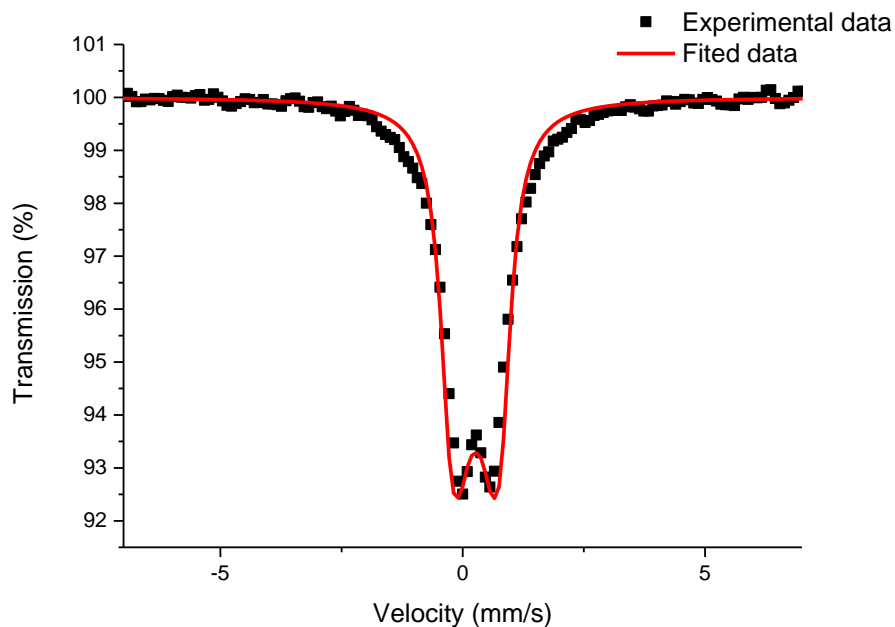
3. Fits performed for Mössbauer spectroscopy

Similarly to ACMS and VSM results, the main part of the thesis shows only couple of fits for the Mössbauer spectroscopy, all of them are presented below. The graphs and tables present spectra and isomer shifts relative to Co(Rh).



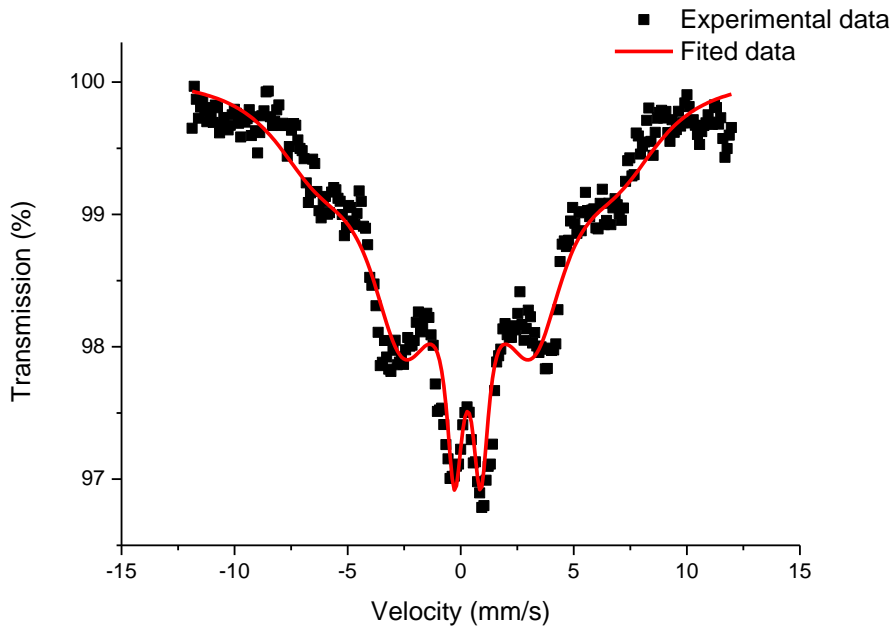
Graph A-XXII Mössbauer spectrum for DEX IONP, without external magnetic field at 4.3 K.

	RELATIVE INTENSITY [%]	FWHM mm/s	IS [mm/s]	B [T]	QS [mm/s]	χ^2
DEX IONP 4,3 K	46(4)	0,25	0.23(1)	52.2(1)	-0.01(1)	0,84
	53(4)	0,32	0.18(1)	50.3(3)	-0.01(1)	



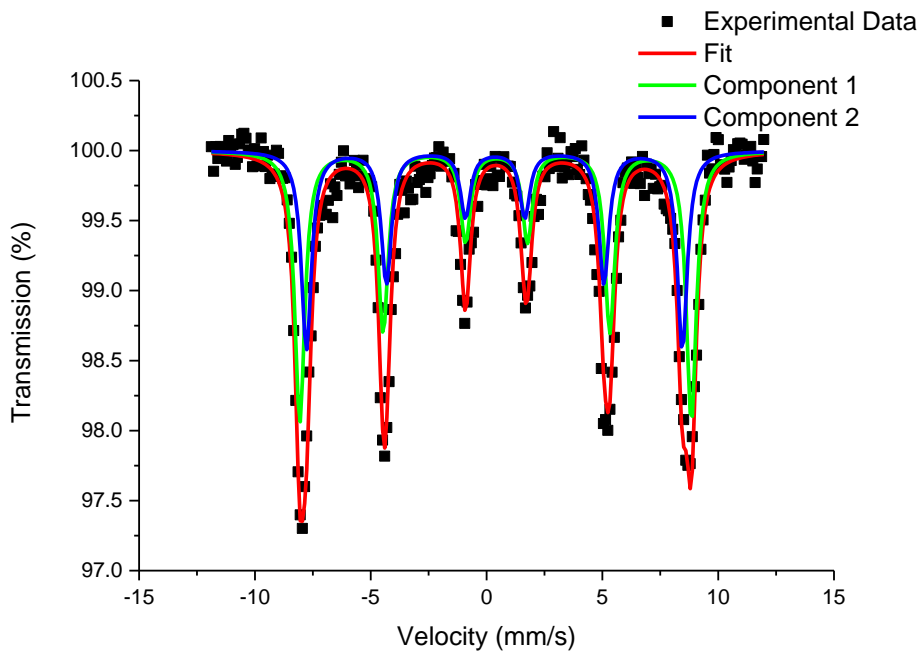
Graph A-XXIII Mössbauer spectrum for DEX IONP, without external magnetic field at RT.

	IS [mm/s]	B [T]	FWHM [mm/s]	f [MHz]	ρ/f	χ^2
DEX IONP RT	0,38	51.6	0,25	10^6	0.07(2)	5,26



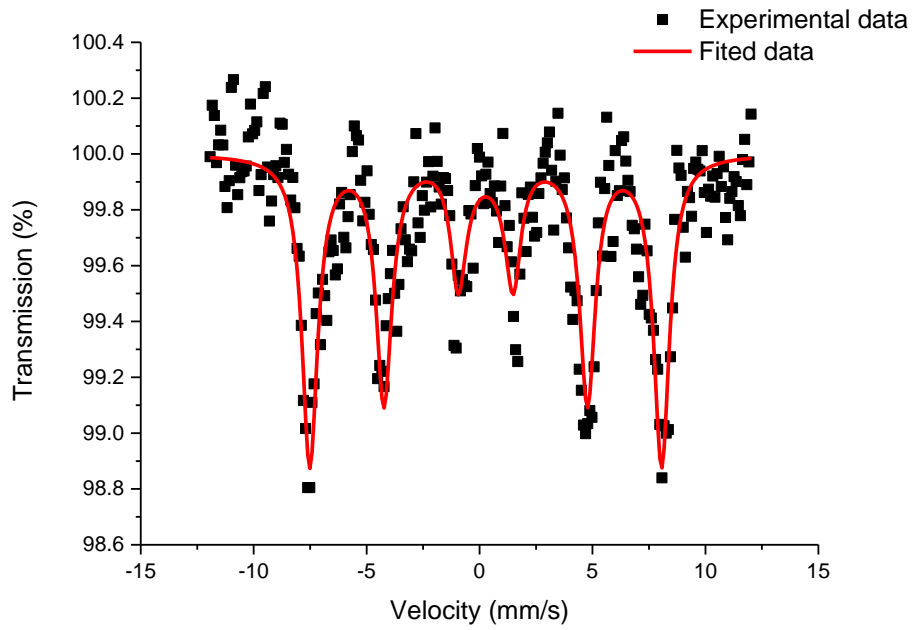
Graph A-XXIV Mössbauer spectrum for DEX IONP, with 0,5 T external magnetic field at RT.

	IS [mm/s]	B [T]	FWHM [mm/s]	f [MHz]	ρ/f	χ^2
DEX IONP RT 0,5T	0.42(2)	50,2	0,30	56(3)	0,44(1)	1,33



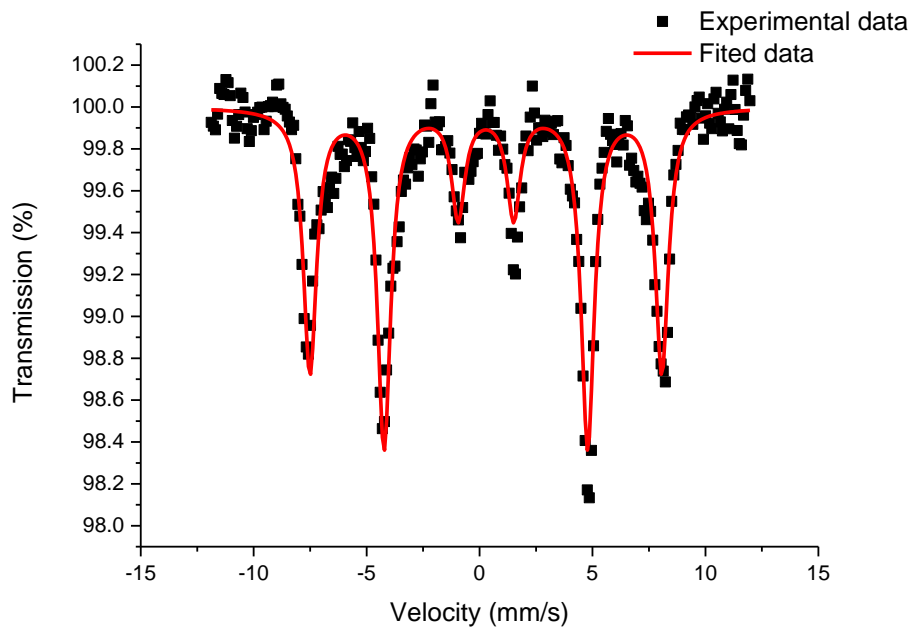
Graph A-XXV Mössbauer spectrum for PEG IONP, without external magnetic field at 80 K.

	RELATIVE INTENSITY [%]	FWHM [mm/s]	IS [mm/s]	B [T]	QS [mm/s]	χ^2
PEG IONP 80 K	58(3)	0,26	0,41(1)	52.3(7)	-0,02(1)	1,32
	42(3)	0,26	0,35(1)	50.2(9)	-0,02(1)	



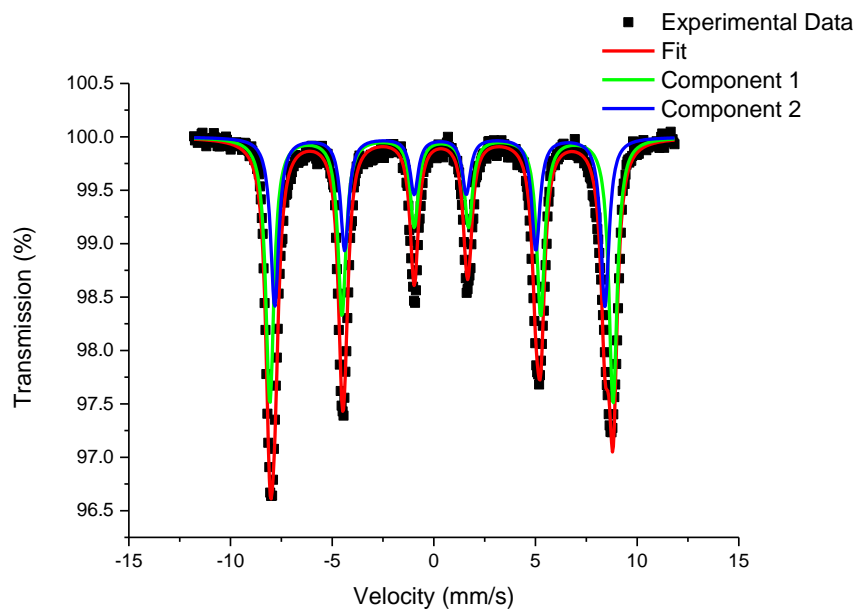
Graph A-XXVI Mössbauer spectrum for PEG IONP, without external magnetic field at RT.

	IS [mm/s]	B [T]	FWHM [mm/s]	f [MHz]	ρ/f	χ^2
PEG IONP RT	0,38(2)	48,3(1)	0,35	1,2(7)	0,44(4)	0,65



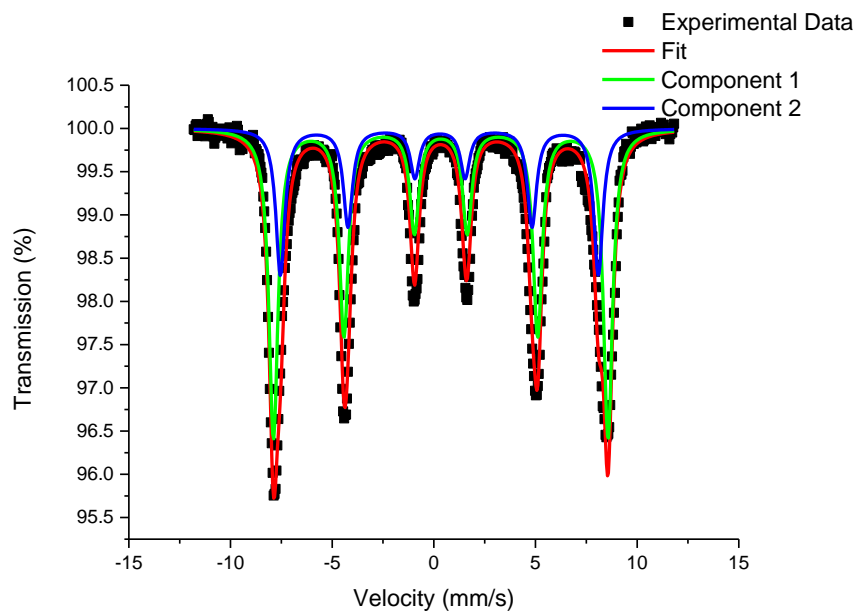
Graph A-XXVII Mössbauer spectrum for PEG IONP, with 0,5 T external magnetic field at RT.

	IS [mm/s]	B [T]	FWHM [mm/s]	f [MHz]	ρ/f	χ^2
PEG IONP RT 0,5T	0,39(1)	48,3	0,35	1,2(4)	0,98(8)	1,17



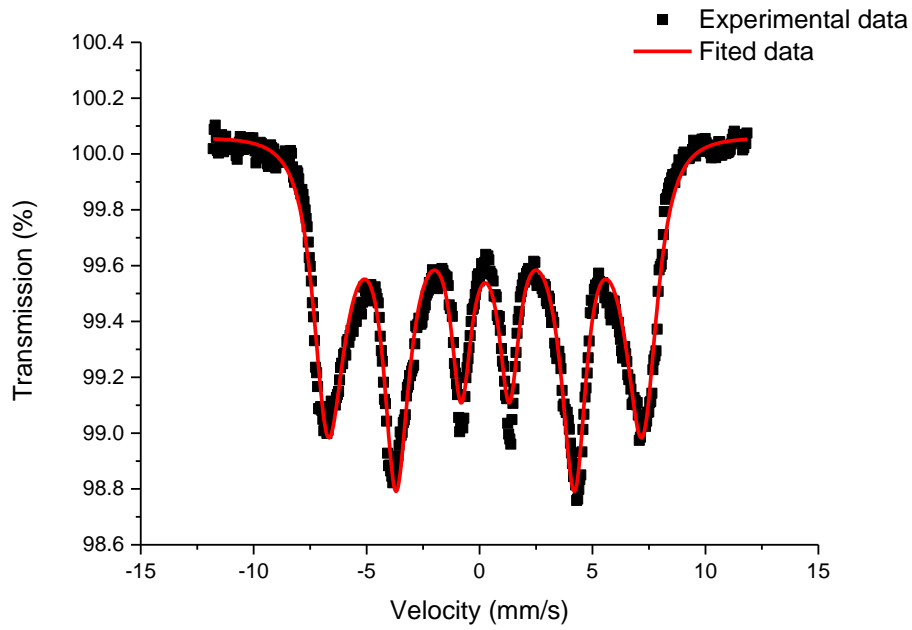
Graph A-XXVIII Mössbauer spectrum for SPION CCh, without external magnetic field at 4.2 K.

	Relative intensity [%]	FWHM [mm/s]	IS [mm/s]	B [T]	QS [mm/s]	χ^2
SPION CCH 4,2 K	61(1)	0,25	0,37(1)	52,3(3)	0,02(1)	0,25
	39(1)	0,26	0,30(1)	50,3(4)	-0,01(1)	



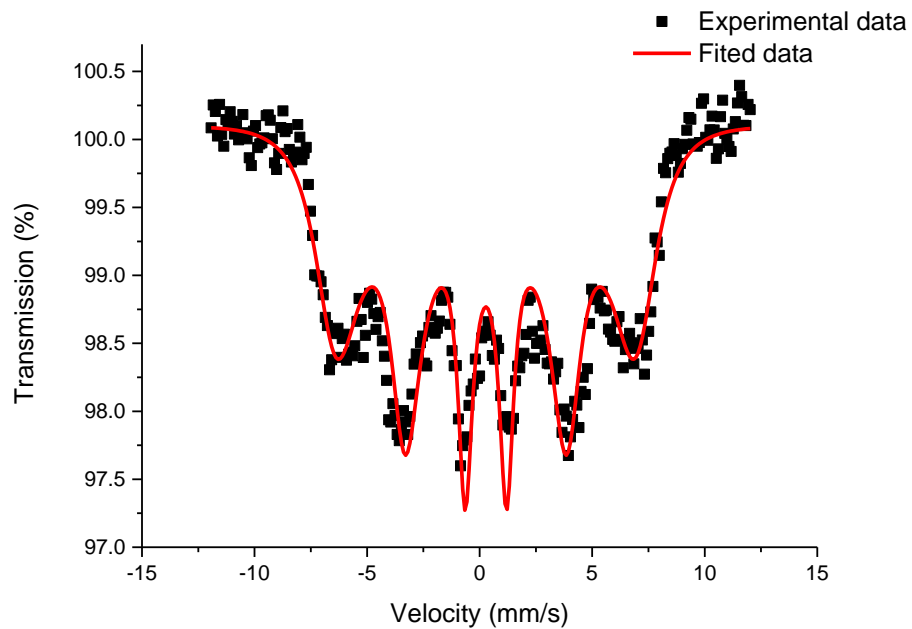
Graph A-XXIX Mössbauer spectrum for SPION CCh, without external magnetic field at 80 K.

	Relative intensity [%]	FWHM mm/s	IS [mm/s]	B [T]	QS [mm/s]	χ^2
SPION CCH 80 K	68(1)	0,25	0,34(1)	50.9(2)	-0,02(1)	2,54
	32(1)	0,32	0,28(1)	48,4(5)	-0,02(1)	



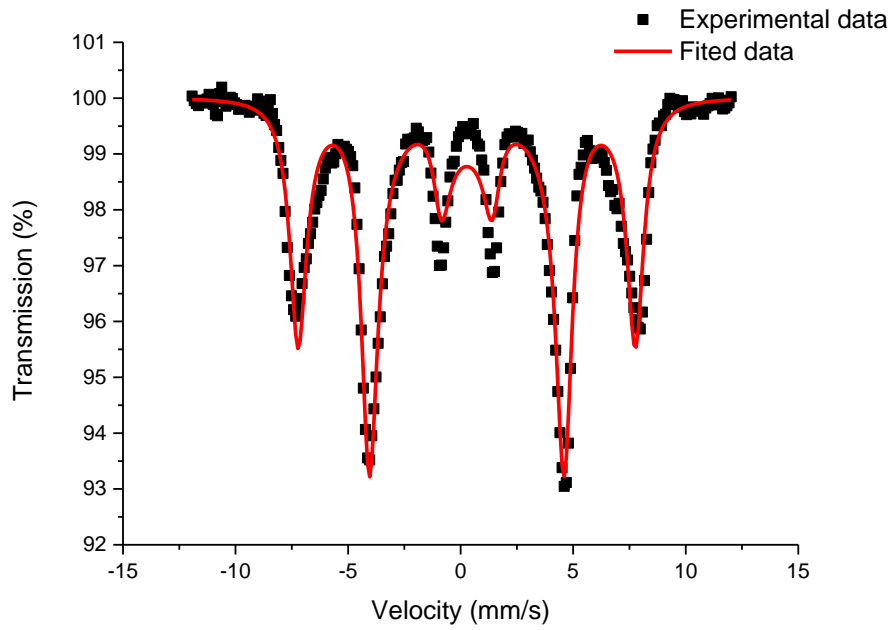
Graph A-XXX Mössbauer spectrum for SPION CCh, without external magnetic field at RT.

	IS [mm/s]	B [T]	FWHM [mm/s]	f [MHz]	ρ/f	χ^2
SPION CCh RT	0,25(1)	46,2(2)	0,54(1)	106(3)	0,91(2)	2,19



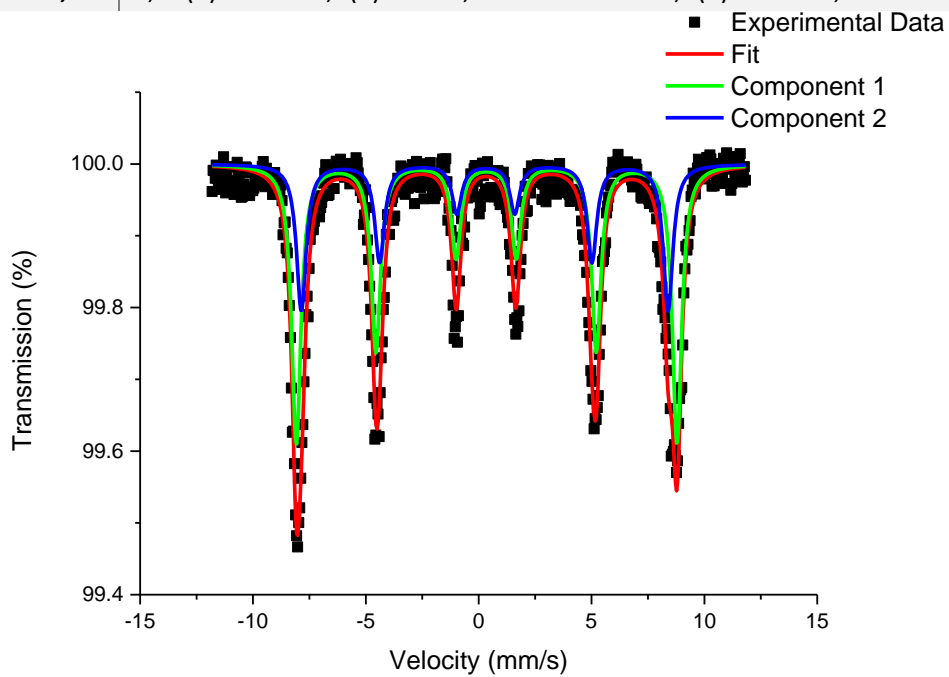
Graph A-XXXI Mössbauer spectrum for SPION CChB, without external magnetic field at RT.

	IS [mm/s]	B [T]	FWHM [mm/s]	f [MHz]	ρ/f	χ^2
SPION CChB RT	0,39(1)	46(6)	0,35	72(6)	0,78(1)	1,33



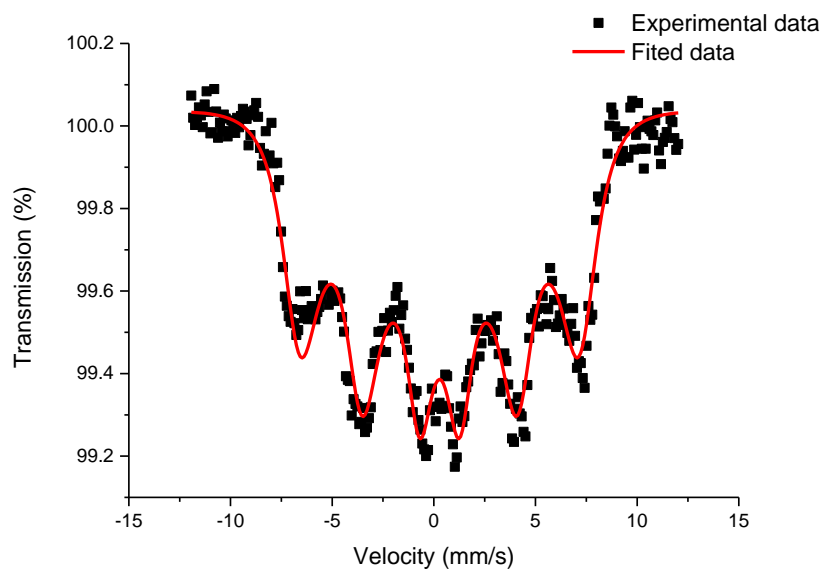
Graph A-XXXII Mössbauer spectrum for SPION CChB, with 0,5 T external magnetic field at RT.

	IS [mm/s]	B [T]	FWHM [mm/s]	f [MHz]	ρ/f	χ^2
SPION CChB RT 0,5 T	0,28(1)	46,5(7)	0,35	4,5(4)	0,8	6,72



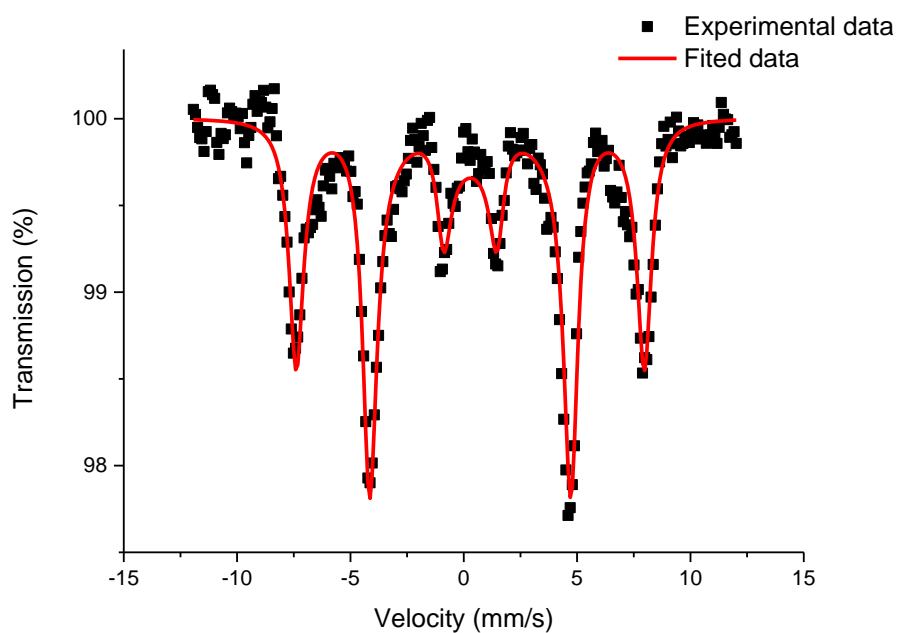
Graph A-XXXIII Mössbauer spectrum for SPION Gd, without external magnetic field at 80 K.

	Relative intensity [%]	FWHM mm/s	IS [mm/s]	B [T]	QS [mm/s]	χ^2
SPION Gd 80 K	64(2)	0,25	0,34(1)	52,3(4)	0,01(1)	0,25
	36(2)	0,26	0,29(1)	50,3(7)	-0,01(1)	



Graph A-XXXIV Mössbauer spectrum for SPION Gd, without external magnetic field at RT.

	IS [mm/s]	B [T]	FWHM [mm/s]	f [MHz]	ρ/f	χ^2
SPION Gd RT	0,39(2)	44,5(4)	0,78(4)	43(4)	0,88(5)	0,62



Graph A-XXXV Mössbauer spectrum for SPION Gd, with 0,5 T external magnetic field at RT.

	IS [mm/s]	B [T]	FWHM [mm/s]	f [MHz]	ρ/f	χ^2
SPION Gd RT 0,5T	0,4	47,7	0,32	3,8(5)	0,82(4)	1,19

List of graphs

Graph IV-I Crystal structure of magnetite with marked tetrahedral and octahedral positions.	28
Graph IV-II Schematic representation of Bragg law.....	29
Graph IV-III Crystallographic directions representation	29
Graph IV-IV Schematic representation of the principle of operation of dynamic light scattering, which is recorded as a function of time.	32
Graph IV-V XRD results for studied SPION and IONP samples with microcrystalline magnetite diffraction pattern for comparison.....	34
Graph IV-VI STEM/TEM images of studied materials	37
Graph IV-VII Particle radii distribution with fitted normal distribution function.	38
Graph IV-VIII Hydrodynamic radius distribution for investigated samples as measured with DLS.	39
Graph V-I A schematic dependence of the coercive field H_C on the particle size, with D_C being critical diameter.....	48
Graph V-II A schematic of the vibrating sample magnetometer.	53
Graph V-III Magnetic hysteresis loops of the SPION-Gd water suspension sample carried out at different temperatures.	56
Graph V-IV Magnetic hysteresis loops of the SPION-Gd sample after subtraction of the diamagnetic contribution from loops presented in Graph V-III.....	57
Graph V-V Cumulative graph of temperature dependences of saturation magnetizations, coercive field asymmetry and coercive fields.....	58
Graph V-VI FC-ZFC magnetization curves of the samples studied normalized to the maximum of the ZFC curve.	60
Graph VI-I Principle of the phase sensitive ACMS measurement.....	64
Graph VI-II Temperature dependence of the magnetic susceptibility of the SPION Gd sample without constant external field at the AC field frequency of 10 kHz and various amplitude.	68
Graph VI-III Temperature dependence of magnetic susceptibility of the DEX-IONP sample without constant external field and with AC field amplitude of 10 Oe and various frequency.	68
Graph VI-IV Temperature dependence of magnetic susceptibility of the DEX-IONP sample at constant external field $H=100$ Oe and with AC field amplitude A of 10 Oe at various frequencies..	69
Graph VI-V Temperature dependence of magnetic susceptibility of the SPION Gd sample without constant external field and with AC field amplitude of 10 Oe at various frequencies.....	69
Graph VI-VI Temperature dependence of magnetic susceptibility of the SPION CChB sample without constant external field and with AC field amplitude of 10 Oe at various frequencies.....	70
Graph VI-VII Temperature dependence of magnetic susceptibility of the SPION CCh sample without constant external field and with AC field amplitude of 10 Oe at various frequencies.....	71
Graph VI-VIII Temperature dependence of magnetic susceptibility of the PEG IONP sample without constant external field and with AC field amplitude of 10 Oe at various frequencies.....	72

Graph VI-IX Temperature dependence of magnetic susceptibility of the DRY PEG IONP sample without constant external field and with AC field amplitude of 10 Oe at various frequencies.....	72
Graph VI-X Temperature dependence of magnetic susceptibility normalized to its maximum of all of the samples studied without constant external field, with AC field amplitude of 10 Oe and a frequency of 10 kHz.	73
Graph VI-XI Blocking temperature of investigated samples as a function of the AC field frequency together with fits to the experimental data.	76
Graph VI-XII Graphical explanation of the procedure of determination of the Brownian contribution at the freezing temperature.	77
Graph VI-XIII The partial Néel (top) and Brown (bottom) relaxation contributions to the magnetic susceptibility at the freezing temperature.	78
Graph VII-I Schematic representations of: isomer shift, and quadruple splitting and the magnetic Zeeman splitting.	83
Graph VII-II Simulated line shapes for $B=540$ kOe, $IS= 0.24$ mm/s and $QS= 0$	88
Graph VII-III Cumulative graph of normalized Mössbauer spectra for all the investigated materials at different temperatures.	90
Graph A-I Temperature dependence of magnetic susceptibility of the DEX IONP sample without constant external field and with AC field grouped by the frequency. ...	108
Graph A-II Temperature dependence of magnetic susceptibility of the DEX IONP sample without constant external field and with AC field grouped by the amplitude. ...	109
Graph A-III Temperature dependence of magnetic susceptibility of the PEG IONP sample without constant external field and with AC field grouped by the frequency. ...	110
Graph A-IV Temperature dependence of magnetic susceptibility of the DEX IONP sample without constant external field and with AC field grouped by the amplitude.....	111
Graph A-V Temperature dependence of magnetic susceptibility of the SPION CCh sample without constant external field and with AC field grouped by the frequency. ...	112
Graph A-VI Temperature dependence of magnetic susceptibility of the SPION CCh sample without constant external field and with AC field grouped by the amplitude. ...	113
Graph A-VII Temperature dependence of magnetic susceptibility of the SPION CChB sample without constant external field and with AC field grouped by the frequency. ...	114
Graph A-VIII Temperature dependence of magnetic susceptibility of the SPION CChB sample without constant external field and with AC field grouped by the amplitude. ...	115
Graph A-IX Temperature dependence of magnetic susceptibility of the SPION Gd sample without constant external field and with AC field grouped by the frequency. ...	116
Graph A-X Temperature dependence of magnetic susceptibility of the SPION Gd sample without constant external field and with AC field grouped by the amplitude. ...	117
Graph A-XI Magnetic hysteresis loops of the DEX IONP sample carried out at different temperatures.	119
Graph A-XII Magnetic hysteresis loops of the DEX IONP sample after subtraction of the diamagnetic contribution from the loops.	119
Graph A-XIII Magnetic hysteresis loops of the PEG IONP sample carried out at different temperatures.	120
Graph A-XIV Magnetic hysteresis loops of the PEG IONP sample after subtraction of the diamagnetic contribution from the loops.	120
Graph A-XV Magnetic hysteresis loops of the SPION CCh sample in water suspension carried out at different temperatures.	121
Graph A-XVI Magnetic hysteresis loops of the SPION CCh sample in water suspension after subtraction of the diamagnetic contribution from the loops.	121

Graph A-XVII Magnetic hysteresis loops of the SIPON CChB sample in water suspension carried out at different temperatures.....	122
Graph A-XVIII Magnetic hysteresis loops of the SPION CCh sample in water suspension after subtraction of the diamagnetic contribution from the loops.	122
Graph A-XIX Magnetic hysteresis loops of the SIPON CChB sample carried out at different temperatures.	123
Graph A-XX Magnetic hysteresis loops of the SPION CCh sample after subtraction of the diamagnetic contribution from the loops.	123
Graph A-XXI Parts of FC-ZFC curves in temperature region between 250 K and 300K.....	124
Graph A-XXII Mössbauer spectrum for DEX IONP, without external magnetic field at 4.3K.....	126
Graph A-XXIII Mössbauer spectrum for DEX IONP, without external magnetic field at RT.....	126
Graph A-XXIV Mössbauer spectrum for DEX IONP, with 0,5 T external magnetic field at RT.....	127
Graph A-XXV Mössbauer spectrum for PEG IONP,without external magnetic field at 80 K.....	127
Graph A-XXVI Mössbauer spectrum for PEG IONP, without external magnetic field at RT.....	128
Graph A-XXVII Mössbauer spectrum for PEG IONP,with 0,5 T external magnetic field at RT.....	128
Graph A-XXVIII Mössbauer spectrum for SPION CCh, without external magnetic field at 4.2 K.....	129
Graph A-XXIX Mössbauer spectrum for SPION CCh, without external magnetic field at 80K.....	129
Graph A-XXX Mössbauer spectrum for SPION CCh, without external magnetic field at RT.....	130
Graph A-XXXI Mössbauer spectrum for SPION CChB, without external magnetic field at RT.....	130
Graph A-XXXII Mössbauer spectrum for SPION CChB, with 0,5 T external magnetic field at RT.....	131
Graph A-XXXIII Mössbauer spectrum for SPION Gd, without external magnetic field at 80K.....	131
Graph A-XXXIV Mössbauer spectrum for SPION Gd, without external magnetic field at RT.....	132
Graph A-XXXV Mössbauer spectrum for SPION Gd, with 0,5 T external magnetic field at RT.....	132

List of tables

Table IV-1 The particle size for investigated samples,	35
Table IV-II Mean radii of three nanoparticle samples as obtained from the fit to the experimental data (see Graph IV-VII).	38
Table IV-III Results of Dynamic Light Scattering measurements.	39
Table V-1 Conversion table of CGS and EMU units to the SI system.....	42
Table V-2 Results of analyses of FC-ZFC curves.	61
Table VI-1 Results of calculations based on the Néel-Arrhenius formula.	74
Table VI-II Estimated frequency at which T_B would be equal to a human body temperature.	76
Table VII-I. Hyperfine parameters for nanoparticle materials studied and microcrystalline maghemite obtained from the fit to the low temperature (4.2 K and 80 K) of Mössbauer spectra.	92
Table VII-II Hyperfine parameters obtained from the fits of Mössbauer spectra of nanoparticle materials measured at room temperature.....	93

List of author's publications

1. Goc, K., Prendota, W., Chlubny, L., Strączek, T., Tokarz, W., (Chachlowska), P. B., (Chabior), K. W., Bućko, M. M., Przewoźnik, J., & Lis, J. (2018). Structure, morphology and electrical transport properties of the Ti_3AlC_2 materials. *Ceramics International*, 44(15), 18322–18328. <https://doi.org/10.1016/j.ceramint.2018.07.045>
2. Goc, K., Przewoźnik, J., Witulska, K., Chlubny, L., Tokarz, W., Strączek, T., Michalik, J. M., Jurczyk, J., Utke, I., Lis, J., & Kapusta, C. (2021). Structure, Morphology, Heat Capacity, and Electrical Transport Properties of $Ti_3(Al,Si)C_2$ Materials. *Materials*, 14(12). <https://doi.org/10.3390/ma14123222>
3. Gumieniczek-Chłopek, E., Odrobińska, J., Strączek, T., Radziszewska, A., Zapotoczny, S., & Kapusta, C. (2020). Hydrophobically Coated Superparamagnetic Iron Oxides Nanoparticles Incorporated into Polymer-Based Nanocapsules Dispersed in Water. *Materials*, 13(5), 1219. <https://doi.org/10.3390/ma13051219>
4. Karnas, K., Karewicz, A., Dulińska-Litewka, J., Strączek, T., Kapusta, C., & Lekka, M. (2021). Interactions of the new SPION-based system bearing anti-N-cadherin antibodies with prostate cancer cells. *Submitted to: „International Journal of Nanomedicine”*.
5. Krawczyk, P. A., Jurczyszyn, M., Pawlak, J., Salamon, W., Baran, P., Kmita, A., Gondek, Ł., Sikora, M., Kapusta, C., Strączek, T., Wyrwa, J., & Żywczak, A. (2020). High-Entropy Perovskites as Multifunctional Metal Oxide Semiconductors: Synthesis and Characterization of $(Gd_{0.2}Nd_{0.2}La_{0.2}Sm_{0.2}Y_{0.2})CoO_3$. *ACS Applied Electronic Materials*, 2(10), 3211–3220. <https://doi.org/10.1021/acsaelm.0c00559>
6. Lempart, M., Derkowski, A., Strączek, T., & Kapusta, C. (2020). Systematics of H_2 and H_2O evolved from chlorites during oxidative dehydrogenation. *American Mineralogist*, 105(6), 932–944. <https://doi.org/10.2138/am-2020-7326>
7. Malinowska, E., Klimaszewska, M., Strączek, T., Schneider, K., Kapusta, C., Podsadni, P., Łapienis, G., Dawidowski, M., Kleps, J., Górski, S., Pisklak, D. M., & Turło, J. (2018). Selenized polysaccharides – Biosynthesis and structural analysis. *Carbohydrate Polymers*, 198, 407–417. <https://doi.org/10.1016/j.carbpol.2018.06.057>
8. Maziarz, P., Matusik, J., Leiviskä, T., Strączek, T., Kapusta, C., Woch, W.M., Tokarz, W., & Górniak, K. (2019). Toward highly effective and easily separable halloysite-containing adsorbents: The effect of iron oxide particles impregnation and new insight into As(V) removal mechanisms. *Separation and Purification Technology*, 210, 390–401. <https://doi.org/10.1016/j.seppur.2018.08.012>
9. Maziarz, P., Matusik, J., Strączek, T., Kapusta, C., Woch, W. M., Tokarz, W., Radziszewska, A., & Leiviskä, T. (2019). Highly effective magnet-responsive LDH-Fe oxide composite adsorbents for As(V) removal. *Chemical Engineering Journal*, 362, 207–216. <https://doi.org/10.1016/j.cej.2019.01.017>

10. Odrobińska, J., Gumieniczek-Chłopek, E., Szuwarzyński, M., Radziszewska, A., Fiejdasz, S., Strączek, T., Kapusta, C., & Zapotoczny, S. (2019). Magnetically Navigated Core–Shell Polymer Capsules as Nanoreactors Loadable at the Oil/Water Interface. *ACS Applied Materials & Interfaces*, *11*(11), 10905–10913. <https://doi.org/10.1021/acsami.8b22690>
11. Prendota, W., Goc, K., Strączek, T., Yamada, E., Takasaki, A., Przewoźnik, J., Radziszewska, A., Uematsu, S., & Kapusta, C. (2019). Properties of NiTi Shape Memory Alloy Micro-Foils Obtained by Pulsed-Current Sintering of Ni/Ti Foils. *Metals*, *9*(3), 323. <https://doi.org/10.3390/met9030323>
12. Rybicki, D., Sikora, M., Stępień, J., Gondek, Ł., Goc, K., Strączek, T., Jurczyszyn, M., Kapusta, C., Bukowski, Z., Babij, M., Matusiak, M., & Zając, M. (2020). Direct evidence of uneven $d_x z$ and $d_y z$ orbital occupation in the superconducting state of iron pnictide. *Physical Review B*, *102*(19), 195126. <https://doi.org/10.1103/PhysRevB.102.195126>
13. Strączek, T., Fiejdasz, S., Rybicki, D., Goc, K., Przewoźnik, J., Mazur, W., Nowakowska, M., Zapotoczny, S., Rumian, S., & Kapusta, C. (2019). Dynamics of Superparamagnetic Iron Oxide Nanoparticles with Various Polymeric Coatings. *Materials*, *12*(11), 1793. <https://doi.org/10.3390/ma12111793>
14. Szpak, A., Fiejdasz, S., Prendota, W., Strączek, T., Kapusta, C., Szmyd, J., Nowakowska, M., & Zapotoczny, S. (2014). T1–T2 Dual-modal MRI contrast agents based on superparamagnetic iron oxide nanoparticles with surface attached gadolinium complexes. *Journal of Nanoparticle Research*, *16*(11), 2678. <https://doi.org/10.1007/s11051-014-2678-6>